Probing Atomic-Scale Properties of Magnetic and Optoelectronic Nanostructures

by

Xiaowei Zhang

A dissertation submitted in partial satisfaction of the

requirements for the degree of

Doctor of Philosophy

in

Physics

in the

Graduate Division

of the

University of California, Berkeley

Committee in charge:

Professor Michael F. Crommie, Chair
Professor Steven G. Louie
Professor Rachel A. Segalman

Fall 2012

Probing Atomic-Scale Properties of Magnetic and Optoelectronic Nanostructures

by

Xiaowei Zhang

Abstract

Probing Atomic-Scale Properties of Magnetic and Optoelectronic Nanostructures

by

Xiaowei Zhang

Doctor of Philosophy in Physics

University of California, Berkeley

Professor Michael F. Crommie, Chair

This dissertation presents scanning tunneling microscopy and spectroscopy studies of individual molecules and graphene nanoribbons (GNRs) bound to a substrate. Understanding the local electronic properties of these systems is importance from a fundamental physics viewpoint and for advancing potential technological applications in nanoelectronics. Two molecular systems, tetracyanoethylene (TCNE), and bithiophene naphthalene diimide (BND), were investigated. The basic questions addressed are (1) how do molecules respond to a condensed matter environment (i.e. a metal or semiconducting surface), (2) how do spins behave in molecule-scale structures, and (3) how do the intrinsic electronic properties of molecules affect their self-assembly behavior. We find that TCNE molecules display variable surface coupling and enable tunable magnetic exchange coupling between covalently bonded spin centers in $V_x(TCNE)_y$ complexes. We also were able to determine the TCNE adsorption site within a molecular monolayer on Ag(100) through a combination of inelastic electron tunneling spectroscopy and density functional theory calculations. We find that BND molecules exhibit type-II heterojunction energy level alignment. The interplay between the bipolar electronic nature of the molecule and the substrate results in different self-assembly patterns on a Au(111) surface. In GNRs we have demonstrated the presence of magnetic edge states for chiral nanoribbons with atomically smooth edges. We have further controlled GNR edges via hydrogen plasma etching, and have determined their exact edge termination.

Contents

List of Figures **iv**

List of Abbreviations **vi**

Acknowledgments **vii**

I Introduction 1

1 Why Nanoelectronics? 2
- 1.1 Molecular Devices . . . 2
  - 1.1.1 Magnetic Molecules for Spintronics Applications . . . 3
  - 1.1.2 Bipolar Molecules for Photovoltaic Applications . . . 4
- 1.2 Graphene Nanoribbon Devices . . . 4
- 1.3 Outline of Dissertation . . . 5

2 Scanning Tunneling Microscopy Principles 6
- 2.1 Theory of Operation . . . 6
- 2.2 STM Topography . . . 7
- 2.3 Elastic Spectroscopy . . . 9
- 2.4 dI/dV Maps . . . 9
- 2.5 Inelastic Electron Tunneling Spectroscopy . . . 10
- 2.6 STM Manipulation . . . 12

3 Instrumentation 13
- 3.1 The Scanning Tunneling Microscope Instrument . . . 13
  - 3.1.1 UHV Chambers and Pumping Systems . . . 13

3.1.2 Cryogenic System . . . 15
3.1.3 Vibration Isolation . . . 15
3.1.4 STM Scanner . . . 15
3.1.5 STM Electronics and Software . . . 16
3.1.6 Coarse Approach and Fine Motion . . . 17
3.2 Sample Preparation . . . 18
3.2.1 Sputtering and Annealing . . . 18
3.2.2 Thin Insulating Layers . . . 18
3.3 Deposition Techniques . . . 19
3.3.1 Knudsen Cell Evaporator . . . 19
3.3.2 Electron Beam Evaporator . . . 21
3.3.3 K Getter Evaporator . . . 21
3.3.4 Leak Valve Evaporator . . . 21
3.3.5 Spin Coating . . . 25

II Magnetic Nanostructures 26

4 Spin Coupling Mediated by TCNE 27
4.1 TCNE on Ag(100) . . . 28
4.2 $V_x(TCNE)_y$ Complexes . . . 29
4.3 V(TCNE) on NaCl . . . 36
4.4 Conclusions . . . 36

5 TCNE Monolayer Adsorption Site Determination 39
5.1 TCNE Monolayer on Ag(100) . . . 40
5.2 STS and IETS of TCNE Monolayer . . . 41
5.3 DFT Calculations on TCNE Monolayer Vibrational Modes . . . 43
5.4 Conclusions . . . 45

III Photovoltaic Molecules 47

6 Energy Level Alignment in a Bipolar Molecule 48
6.1 Introduction to Organic Solar Cells . . . 48
6.1.1 Photovoltaic Principles of Organic Solar Cells . . . 48
6.1.2 Organic Photovoltaic Materials . . . 49
6.1.3 Device Architectures . . . 50
6.2 Bipolar Molecules . . . 51
6.3 BND Molecules on NaCl/Ag(100) . . . 52
6.4 DFT Calculations on BND Molecule . . . 56
6.5 Conclusions . . . 58

7 Self-Assembly of Bipolar Molecules on Au(111) 59
7.1 Molecules on Au(111) Terraces 60
7.2 Molecules near Step-edges 61
7.3 Conclusions 61

IV Graphene Nanoribbons 63

8 Edge States of Chiral Graphene Nanoribbons 64
8.1 Graphene Nanoribbons on Au(111) 64
8.2 Edge State of GNRs 68
8.3 Theoretical Calculations on GNRs 71
8.4 Conclusions 75

9 Controlling the Edge Termination of GNRs 76
9.1 Hydrogen Plasma Treated GNRs on Au(111) 76
9.2 Thermodynamic Calculations of Edge Terminations 78
9.3 Conclusions 84

Bibliography 85

List of Figures

1.1 Screening around a local spin on the surface 4

2.1 Tunneling diagram 7
2.2 STM schematic diagram 8
2.3 Atomic resolution of Ag(100) surface 9
2.4 Simulated $I - V$ and dI/dV curves 10
2.5 Inelastic electron tunneling diagram 11
2.6 STM manipulation diagram 12

3.1 Overview of the home-built UHV LT STM 14
3.2 STM stage and scanner 16
3.3 NaCl islands on Ag(100) 19
3.4 CuN islands on Cu(100) 20
3.5 Knudsen cell evaporator 20
3.6 Electron beam evaporator 22
3.7 Room temperature leak valve evaporator setup 23
3.8 Low temperature leak valve evaporator setup 24

4.1 TCNE molecular structure 27
4.2 TCNE on Ag(100) 29
4.3 DFT calculations of TCNE HOMO 30
4.4 Construction of $V_x(TCNE)_y$ on Ag(100) 30
4.5 Various $V_x(TCNE)_y$ structures 31
4.6 $V_x(TCNE)_y$ structure models 32
4.7 $V_x(TCNE)_y$ high bias spectra 33
4.8 $V_x(TCNE)_y$ low bias spectra 34
4.9 $V_2(TCNE)$ spectra 35

4.10 V(TCNE) and V_2(TCNE) SP-DFT calculations 35
4.11 TCNE on NaCl topographs 37

5.1 Topograph of TCNE monolayer on Ag(100) 41
5.2 STS and IETS of TCNE molecules within a monolayer 42
5.3 DFT calculations of TCNE monolayer 44

6.1 Photovoltaic principles of organic solar cells 49
6.2 Organic semiconductor examples 50
6.3 Organic solar cell arichitectures 51
6.4 Bithiophene naphthalene diimide molecule structure 52
6.5 Topograph of BND molecules on NaCl islands 53
6.6 dI/dV spectroscopy of a BND molecule on NaCl 54
6.7 Other dI/dV spectroscopic behavior of BND molecules 55
6.8 dI/dV maps of a BND molecule on NaCl 55
6.9 Calculations of quasi-particle LDOS of BND molecule 57

7.1 Directly bonded BND molecule structure 59
7.2 Self-assembly of direct BND molecules on terraces 60
7.3 Self-assembly of direct BND molecules near step-edges 61
7.4 Schematic and STM images of parallel molecular chains 62

8.1 Graphene nanoribbons on Au(111) 65
8.2 Partially unzipped carbon nanotubes on Au(111) 66
8.3 Folded GNRs on Au(111) 67
8.4 Determination of chirality of GNRs 69
8.5 Edge states of GNRs 70
8.6 Position- and width-dependent edge-state properties 72
8.7 Theoretical band structure and DOS of a 20-nm-wide $(8, 1)$ GNR 74

9.1 Hydrogen plasma treated GNRs on Au(111) 77
9.2 Experiment and simulated images of GNR edges 79
9.3 H-terminated GNR edges thermodynamic stability calculation 80
9.4 Simulated STM images for (2, 1) chiral edge 82
9.5 Comparison of line profiles of experimental and simulation images 83

List of Abbreviations

DFT	Density Functional Theory
dI/dV	Differential Conductance
DOS	Electronic Density of States
e_c	Absolute value of the Electron Charge
E_F	Fermi energy
FE	Field Emission
FWHM	Full Width at Half Maximum
HOMO	Highest Occupied Molecular Orbital
IETS	Inelastic Tunneling Spectroscopy
LDOS	Local Density of States
LT	Low Temperature (around 77 K or lower)
LUMO	Lowest Unoccupied Molecular Orbital
ML	Monolayer
rms	Root Mean Square
RT	Room Temperature
STM	Scanning Tunneling Microscopy *or* Scanning Tunneling Microscope
STS	Scanning Tunneling Spectroscopy
UHV	Ultra High Vacuum

Acknowledgments

There are many people to thank for their support throughout the time this work was done. First and foremost, I would like to express my sincere thanks to my advisor, Professor Michael Crommie, for his guidance and support during the past five years. His insight into physics provides novel research ideas and his enthusiasm has always been an inspiration. He cares about his students and always makes time for them to discuss any questions. I feel very grateful to have him as my advisor.

I would also like to express my special thanks to graduate student Ryan Yamachika and postdoctoral fellow Daniel Wegner. They were my first co-workers in the group and I learned a lot from them. Ryan patiently showed me every detail of the STM, taught me how to fix equipment, introduced me to STM theory and molecular physics. His broad knowledge, diligence and persistence have greatly impressed me. Daniel also taught me a lot of STM principles and good experimental techniques. He guided me how to analyze data, showed me how to effectively present results. His cheerful and optimistic nature made the lab a pleasant place. I feel very fortunate to have gotten to work with them.

In addition to my earliest co-workers, there are many other people who I directly worked with contributed to this work. We spent a lot of time doing the experiments, analyzing data, fixing the STM, and writing papers. I learned a lot from them, and they made the lab work more enjoyable. I would like to thank postdoctoral fellows Yayu Wang, Chenggang Tao, and Dimas de Oteyza, graduate students Yen-Chia Chen, visiting graduate student Juanjuan Feng, undergraduate students Melissa Panlasigui, Yasaman Bahri, and Zahra Pedramrazi.

There are also other people in the group to thank whom I sometimes worked with, discussed with, and learned from: postdocs Luis Berbil-Bautista, Yuanbo Zhang, Sarah Burke, Regis Decker, Alexander Riss, Miguel Ugeda, and Peigen Cao, graduate students Jongweon Cho, Victor Brar, Niv Levy, Kacey Meaker, Sebastian Wickenburg, Chuck Sleasman, Aaron Bradley, Giang Nguyen, Ivan Pechenezhskiy, Yang Wang, and Dillon Wong, undergraduate students Kunal Sahasrabuddhe, Travis Zack, Hsin-zon Tsai, Brandon Giles, Steven Munn,

Chad Germany, Drew Edelberg, and Zaw Htet, visiting student Qiong Wu.

There are many theory collaborators to thank for their computational and theoretical assistance. Mark Pederson and Tunna Baruah have helped us with magnetism related DFT calculations. Professor Steven Louie and his group members Georgy Samsonidze and Oleg Yazyev have helped us understand the energy level alignment in bipolar molecules and magnetic edge states in graphene nanoribbons. Their theoretical calculations provided great insights into our experimental measurements.

There are many collaborators who provided us with the materials that we studied. Without their high quality samples, many of our experiments would not be possible. Professor Jeffrey Long and his group member Bart Bartlett synthesized the magnetic molecules that we studied. Professor Rachel Segalman and her group member Jibin Sun synthesized the novel bipolar molecules that exhibit the desired type-II heterojunction behavior. Professor Hongjie Dai and his group members Liying Jiao, Liming Xie have synthesized very clean graphene nanoribbon samples that we were not able to obtain elsewhere.

I would like to thank many stuff members in the physics department for their support. Anne Takizawa and Donna Sakima in the graduate student service office are always very supportive and helpful. They kindly helped me with all the paperwork and bureaucratic details. Marco Ambrosini in the main machine shop have been very helpful in designing and machining part. Joseph Kant in the student machine shop have always been nice answering questions and guiding me use the machines.

Finally, I would like to thank my family: my dad Longbao Zhang, my mom Lin Xu, and my husband Fuzhuo Huang, for their endless love, understanding and support throughout all these years.

Part I

Introduction

1 Why Nanoelectronics?

Constant technological and scientific advances have continually improved the size and performance of silicon microelectronics devices. Following Moore's law [127], which predicted that the number of transistors on a chip would double every two years and consequently exponentially increase computational ability, semiconductor devices have reduced in size on a yearly basis. This trend has continued for five decades and will eventually lead us to nanometer-sized circuit components. However, at this length scale traditional semiconductor technology will encounter tremendous difficulties due to current leakage and high power consumption [138].

Different approaches and new designs of electronic devices have been proposed to overcome these difficulties. One promising potential solution is to utilize new nanoscale building blocks, such as molecules and graphene, to construct electrical circuits. Resulting molecular and graphene devices have opened new opportunities for both science and technology, and it is important now to understand their properties in order to successfully implement new device architecture. This is a motivating factor for my study of single molecules and graphene nanoribbons in this thesis.

This chapter gives an overview of molecular and graphene devices and introduces the materials that I have studied. This chapter also presents additional motivation for these studies and gives an outline of the whole dissertation.

1.1 Molecular Devices

Molecular devices are potentially extraordinarily efficient for performing certain functions. With advances in physics, chemistry, engineering and other related fields, many nanometer-size devices can now be realized [5], such as C_{60} molecular transistors [142], nanotube radios [89], logic gates via molecular motion [69], and rotational actuators [45]. To further develop new and more useful molecular devices, a thorough understanding of single molecule properties in condensed matter environments is becoming increasingly important.

The physics of single molecule structure is fundamentally different from that of macroscopic objects. The performance of molecular devices is determined by factors that depend on the intrinsic properties of the molecule, the influence of the local environment, and our ability to control and actuate molecular structures. Intrinsic molecular properties, such as electronic, magnetic, and optical response, will determine the function of any molecular device. In such devices, molecules will be inevitably in contact with other substances, for example, electrodes. The influence of the local environment, such as charge transfer, broadening of molecular states, thus needs to be well understood in order to design devices. Future applications of molecular devices will depend on how these properties can be controlled. Molecular nanoscience addresses these fundamental molecular physics questions, and helps point the way towards future device applications, thus creating exciting opportunities in both science and technology.

1.1.1 Magnetic Molecules for Spintronics Applications

Molecule-based spintronics raises new possibilities for electronic and magnetic devices [20, 82]. However, for this concept to become reality, a more fundamental understanding of the interaction between the molecule adsorbates and the substrate as well as the interaction between different spin centers, is necessary, due to the fact that spin coupling and magnetic anisotropy can change as the local environment is varied [165, 8]. To understand these types of effects for a model system, I studied the magnetic molecule platform tetracyanoethylene (TCNE) in this dissertation.

TCNE is a strong π-electron acceptor with a large electron affinity [32] that easily forms charge-transfer complexes by pulling electrons from neighboring metal atoms or molecules [47, 120]. Bulk V(TCNE)$_x$ with $x \sim 2$ is the first known room temperature organic magnet, and have a Curie temperature of $\sim 400\,\mathrm{K}$ [119, 155, 175, 99]. This motivated us to design spin networks using TCNE as a molecular linker and vanadium atoms as spin centers, since we expected good spin coupling through the TCNE molecules. Despite much research done on the bulk and thin films of V(TCNE) in past years, the origin of TCNE-based ferromagnetism is still not well understood [155, 67, 175], thus making TCNE an interesting candidate to explore molecule-based magnetism at microscopic length scales.

Magnetic adsorbates can interact with surfaces in various ways, such as through the RKKY interaction. With spin sensitive local probes, such as spin polarized STM, one can obtain local magnetic and spin properties of a system. However, even without a spin sensitive probe, one may still access certain magnetic properties. One way is through inelastic spin excitation signals [70]. When a tunneling electron's energy exceeds the spin excitation energy, the electron may induce a spin transition. Another way of detecting spins is through a phenomenon known as the *Kondo effect* [98]. When a magnetic impurity is placed in contact with a bulk metal, and the temperature is lowered below a characteristic temperature scale (the Kondo temperature), then electrical resistance of the sample begins to increase rather than decrease as is normally expected. In this situation, the interaction between electrons in the bulk state and the local spin results in a spin singlet state, and a screening

cloud is formed in the vicinity of the molecule, as schematically shown in figure 1.1. Often

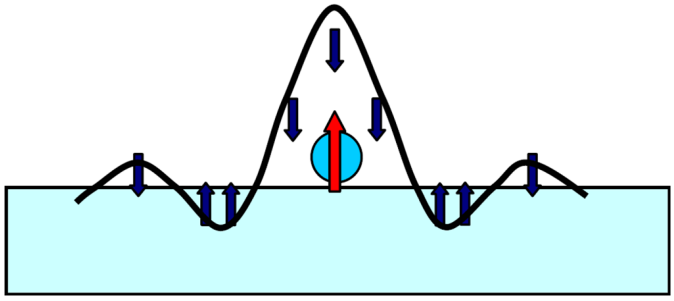

Figure 1.1: Kondo screening cloud around a local spin on the surface.

in STM, the Kondo effect is characterized as a sharp resonance in dI/dV spectra near the Fermi energy.

1.1.2 Bipolar Molecules for Photovoltaic Applications

Bipolar molecules that incorporate donor and acceptor components within a single covalently bonded scaffold are the subject of much interest for applications in diodes, LEDs, and photovoltaic (PV) devices [39, 164]. The suitability of such molecules for future applications depends on many factors, including the energy and geometry of molecular orbitals and intramolecular interfaces, the influence of environment, and properties such as electrical contacts and optical excitation response [132, 122]. For PV applications it is particularly important for bipolar molecular orbitals to have staggered energy levels with strong orbital localization between the two halves of the molecule [172, 197, 46]. In macroscopic devices this situation is referred to as a "type II heterojunction" [93].

The bipolar molecules used in our work incorporate bithiophene as the electron donor, and naphthalene diimide as the electron acceptor. Since molecular electronic properties are very inhomogeneous at sub-nanometer length scales, a local probe such as an STM is needed to resolve spatial variation in electronic structure. The potential for making a nanometer scale photovoltaic cell makes this molecule an interesting system to study.

For device applications, it is important to understand how these molecules respond to different environment and how these molecules interact with each other. Many interesting properties may arise due to collective behavior of these molecules on a metallic surface.

1.2 Graphene Nanoribbon Devices

Since the successful isolation of graphene in 2004 [134], graphene has become the subject of intense experimental and theoretical scrutiny. Graphene possesses many intriguing electronic properties. The charge carriers in graphene behave like "massless Dirac fermions" with remarkably high mobility [53]. They also display an anomalous quantum Hall effect

[133, 199] and show Klein tunneling phenomena [196]. Furthermore, graphene has proven itself to be a versatile and chemically stable material that can be patterned with conventional lithography techniques [65, 53]. Thus, there is great interest in using graphene as a building block for new electronic technologies.

The fact that intrinsic graphene is a zero bandgap semiconductor is a major problem for mainstream logic applications. Introducing lateral confinement into graphene, i.e., making graphene nanoribbons (GNRs), is one solution to open up a bandgap in this 2D material. Such GNRs have been predicted to exhibit a wide range of behaviour, including tunable energy gaps [169, 43], and the presence of one-dimensional (1D) edge states [129, 1, 186] with unusual magnetic structure [51, 170]. These properties make GNRs a very interesting new system to study.

1.3 Outline of Dissertation

This dissertation is divided into four parts. The first part introduces the main instrument used in our studies: a home-built low-temperature ultra high vacuum scanning tunneling microscope (STM). Chapter 2 reviews the fundamental tunneling theory and STM operational modes. Chapter 3 describes the detailed STM instrumentation and related experimental techniques that are used in our work.

The second part of the dissertation presents experimental studies on magnetic nanostructures, more specifically, TCNE molecules and $V_x(TCNE)_y$ complexes. Chapter 4 describes the interaction between TCNE and Ag(100) substrates, and how we are able to build $V_x(TCNE)_y$ complexes via STM manipulation. Depending on the particular structure of $V_x(TCNE)_y$ complexes and their orientation relative to the Ag(100) substrate, the strength of the TCNE-mediated spin coupling between V atoms can be tuned. Chapter 5 presents an in-depth study focused on determining TCNE adsorption sites within a molecular monolayer on Ag(100). Combining inelastic electron tunneling spectroscopy (IETS) and density functional theory (DFT) calculations, we are able to obtain this precise structural information.

The third part of the dissertation focuses on bipolar molecules that have potential photovoltaic applications. Chapter 6 introduces the bithiophene naphthalene diimide (BND) molecule, and shows how we measure type-II heterojunction energy level alignment within a single molecule. Chapter 7 describes the self-assembly properties of BND molecules. Depending on the environment, they form either anti-parallel or parallel aligned chains.

The fourth part of the dissertation describes our studies of graphene nanoribbons (GNRs). Chapter 8 demonstrates our measurement of the presence of magnetic edge states in chiral GNRs with atomically smooth edges. Chapter 9 describes our ability to control and determine the edge termination of hydrogen-plasma-treated GNRs.

2

Scanning Tunneling Microscopy Principles

Since the invention of the scanning tunneling microscopy (STM) by Binnig and Rohrer in 1982 [13, 14], it has served as one of the premier surface characterization tools. The main strengths of the STM include its imaging [15, 36], manipulation [38, 9], and spectroscopic characterization [34, 35, 171, 70] capabilities on nanostructures with sub-angstrom precision. These properties make the STM an ideal choice for studying atomic and electronic properties of adsorbates on conducting substrates, as well as for modifying and controlling chemical properties at the atomic scale [184].

In an STM a sharp metal tip (usually made of W or Pt-Ir) is placed very close ($\sim 6\,\text{Å}$) to a conducting surface. By applying a bias voltage between the tip and the sample, a tunneling current is generated. Qualitatively, the tunneling current exponentially decays with the increase of the tip-sample distance, which gives the STM its high spatial resolution. Quantitatively, the basic formalism used to explain electron tunneling between two electrodes was first given by Bardeen in 1961 [7], and later developed by Tersoff and Hamann [176] for the specific STM configuration. A detailed derivation of the tunneling current will be given in this chapter.

2.1 Theory of Operation

The details of the electron tunneling process in an STM have been discussed in several classic references [7, 176, 27]. Under the condition of elastic tunneling events, the tunneling current between the STM tip and the sample can be expressed as [27],

$$I(V) \propto \int_{-\infty}^{\infty} [f(E - e_c V) - f(E)]\, \rho_s(E) \rho_t(E - e_c V) |M_{t-s}(E, V, z_0)|^2 dE \qquad (2.1)$$

where $f(E)$ is the Fermi-Dirac function, $\rho_s(E)$ and $\rho_t(E)$ are the sample and tip local density of states, respectively, $|M_{t-s}(E, V, z_0)|$ is the tunneling matrix element. The bias

voltage V is defined as the voltage of the sample relative to the tip following the usual STM convention. z_0 is the tunnel barrier width (i.e., tip-sample distance). A schematic drawing of the tip and sample density of states under the tunneling condition is shown in figure 2.1.

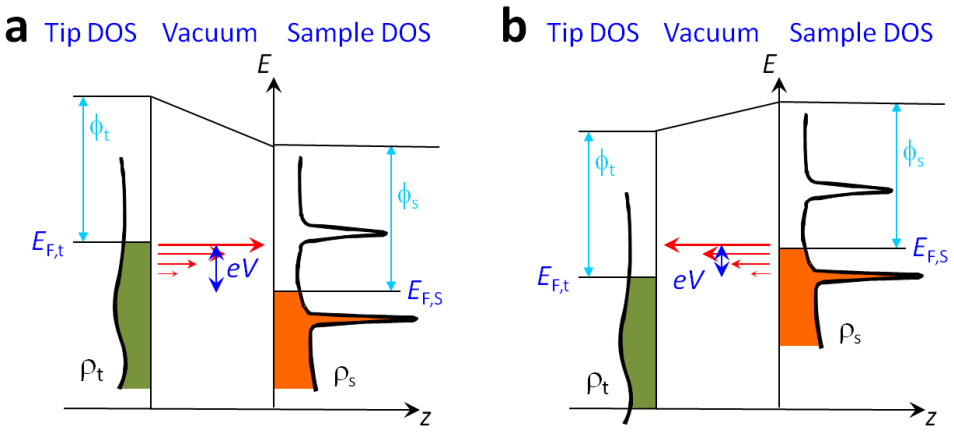

Figure 2.1: Schematic tunneling diagram in STM.

Typical approximations used to simplify equation (2.1) are the following:

1. $T = 0K$.
2. The tip DOS ρ_t is a constant with respect to energy.
3. $|M_{t-s}(E, V, z_0)|^2 \sim \exp(-\kappa z_0 \sqrt{\phi_0})$, where ϕ_0 is the substrate work function, and $\kappa = 2\sqrt{2m_e/\hbar^2} = 1.02\,\text{Å}^{-1}V^{-1/2}$.

Under these approximations, equation 2.1 simplifies to

$$I(V) \propto \exp(-\kappa z_0 \sqrt{\phi_0}) \int_0^{e_c V} \rho(E_F + E)dE \tag{2.2}$$

2.2 STM Topography

For simplicity we first define the plane of a sample's surface to be the xy-plane, and the direction perpendicular to the surface as the z direction (figure 2.2). In typical STM topography mode, a constant voltage is applied to the tip or sample (figure 2.2 shows it applied to the tip, which is equivalent to applying $V = -V_{tip}$ to the sample), and feedback circuits are used to keep the tunneling current $I(V)$ constant (figure 2.2). The position of the tip in the xy-plane is controlled by piezoelectric crystals. When scanning the tip in the xy-plane, the plot of the change in the z position of the tip as a function of x and y is referred to as the constant-current topograph.

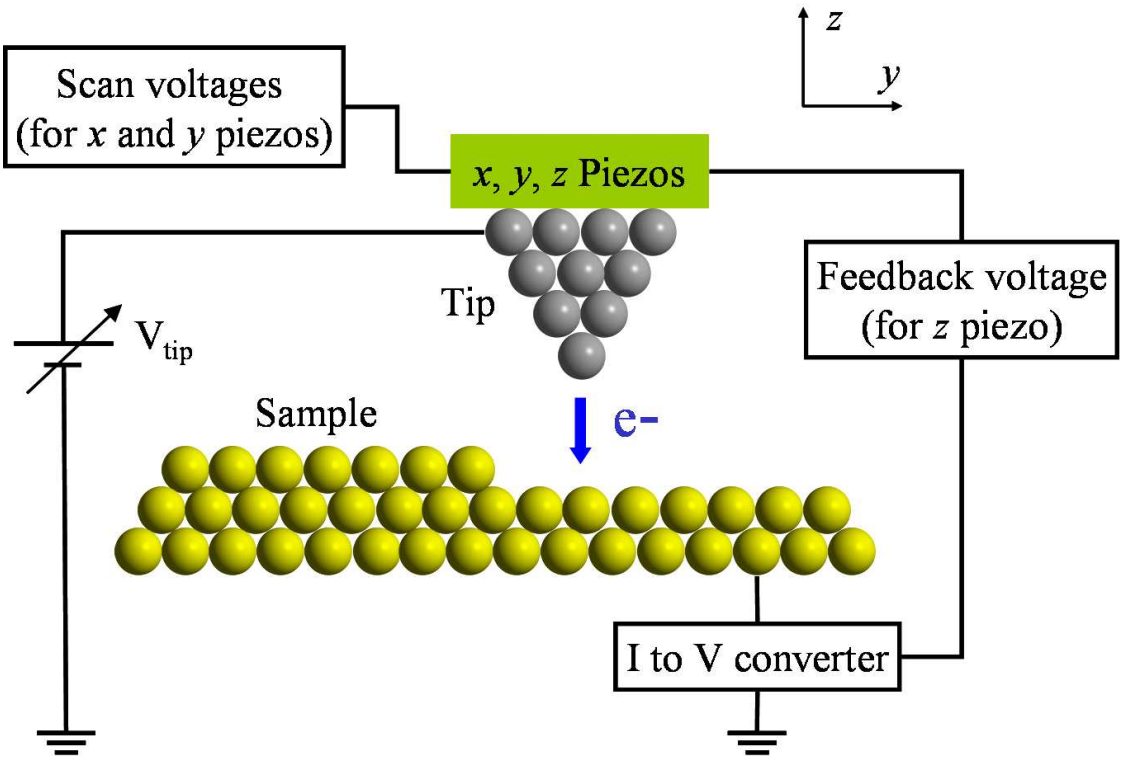

Figure 2.2: Diagram showing the basic setup of an STM. A constant voltage V_{tip} is applied to the tip while voltages are applied to piezos to move the tip in the x and y directions. The tunneling current is measured by a current to voltage converter connected to the sample and the tunneling current enters feedback electronics which controls the z piezo to maintain constant tunneling current.

The tunneling current is determined by the electron states in the tunneling window defined by the bias voltage (equation 2.2). What we plot is a surface where the integral of the LDOS is constant. Positive and negative biases probe the unoccupied and occupied states respectively. Topographic images can have strong dependence on the sign and value of the bias, since the spatial distribution of the molecular states can have large variation in energy.

For typical metal work functions ($\phi \sim 5\,\mathrm{eV}$), the current decreases by one decade for an increase of 1 Å in the tip-sample-separation. One can exploit such sensitive dependence to achieve atomic resolution of the surface, as shown in figure 2.3. Another fortunate consequence of the exponential dependence is that only the atoms closest to the surface will contribute to the tunneling current, so tip preparation techniques that change the apex of the tip are widely used under vacuum.

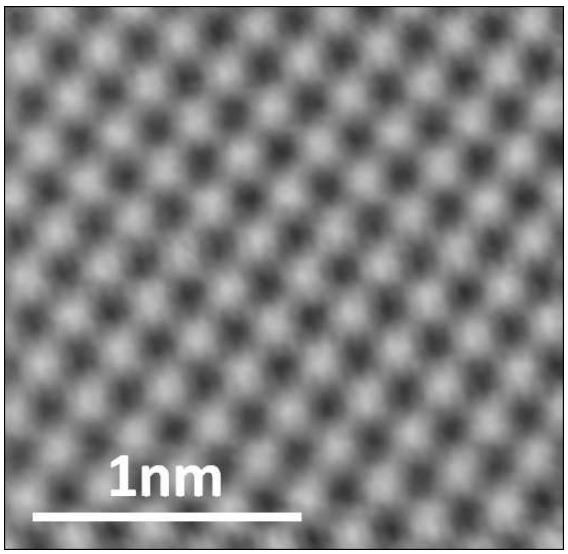

Figure 2.3: STM topograph showing the measured atomic lattice of a Ag(100) surface.

2.3 Elastic Spectroscopy

The electronic properties responsible for the tunneling current can be measured by examining how the tunneling current changes with bias voltage. The process for an STM to measure dI/dV spectroscopy is called scanning tunneling spectroscopy (STS). In STS, the tip is kept at a fixed position $\vec{r}_0$ and the bias voltage is changed while simultaneously recording the dI/dV signal. From equation 2.2,

$$\frac{dI}{dV} \propto \text{LDOS}(\vec{r}_0, E_F + e_c V) \tag{2.3}$$

Hence, dI/dV measures the sample local density of states. Simulated $I-V$ and dI/dV are shown in Figure 2.4.

While it is tempting to numerically differentiate $I(V)$, we instead use a lock-in amplifier to measure dI/dV since this technique effectively increases the signal-to-noise ratio. In this setup a small modulation voltage is added to the bias voltage and the resulting modulation current can be read using a lock-in amplifier. In our experiments, we use typical modulation voltages of $1-10\,\text{mV}$ rms with frequency of $\sim 451\,\text{Hz}$. To compensate for the capacitive coupling between the tip and sample, the lock-in phase is set 90° out of phase with the capacitive signal.

2.4 dI/dV Maps

As discussed in the previous section, dI/dV spectroscopy measures the local density of states at the tip apex. Since $\text{LDOS}(\vec{r}, E_0) = \sum_m |\psi(\vec{r})|^2 \delta(E - E_0)$, this is approximately

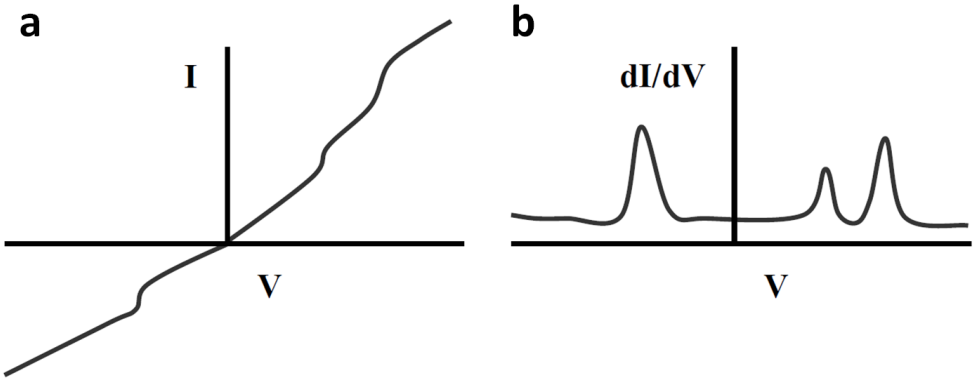

Figure 2.4: Simulated $I - V$ and dI/dV curves.

the density of states at energy E_0 multiplied by the square of all wavefunctions with energy E_0 at position $\vec{r}$, and so is highly spatially dependent. The spatial variations of the dI/dV spectroscopic features can be characterized by mapping dI/dV as a function of tip position.

To take such a dI/dV map, we keep the tip voltage constant and scan the surface in the x and y directions while keeping the feedback on (so that I is constant). We then measure dI/dV during this process and plot it as a function of (x, y). The resulting plot is called a dI/dV map.

Such energy-resolved spectroscopic mapping has been used to image the dispersion of surface states in metals [36]. In Chapter 6, we also use dI/dV maps to map out the spatial localization of different molecular orbitals.

2.5 Inelastic Electron Tunneling Spectroscopy

In the elastic tunneling process described in the previous sections, we assume electrons do not lose energy while traveling from the tip to the sample. However, it is possible for electrons to lose energy via other channels such as molecular vibration, that is, they can tunnel *inelastically*.

The effects of inelastic tunneling can be observed in STM spectroscopy data in two regimes: (1) as side peaks around an electronic resonance, (2) as symmetric steps around E_F. The first regime corresponds to inelastic tunneling into vibronic states near E_F, and leads to the formation of a series of equally spaced peaks in dI/dV. Such inelastic vibrational side-bands were first observed in single molecule transistor experiments [142, 143, 144], and then seen in STM for molecules separated from a conducting substrate by a thin insulating layer [157, 112, 188]. They are rarely seen for molecules directly on conducting surfaces. In this latter case the larger hybridization reduces the residence time of the electron on the molecule, thus decreasing the electron-vibration interaction, and thereby making the vibrational side-band much weaker in amplitude.

The second inelastic tunneling regime corresponds to an electron tunneling to an elec-

tronic state via a virtual transition from a more energetic state. For example, in the presence of a molecular vibrational mode that has an excitation energy of $E_{inel} = e_c V_{inel}$ (figure 2.5), under the situation when the bias voltage $|V| < V_{inel}$, electrons do not have enough energy to excite the vibration; i.e., they tunnel elastically through the molecule (blue arrows in figure 2.5a). Once $|V| > V_{inel}$, electrons can lose energy E_{inel} to excite the vibration (red arrows in figure 2.5a). This inelastic tunneling channel gives rise to a sudden increase of current at $|V| = V_{inel}$, which appears as steps in the dI/dV plot, and a peak and a dip at positive and negative bias in the d^2I/dV^2 plot, as schematically shown in figure 2.5b.

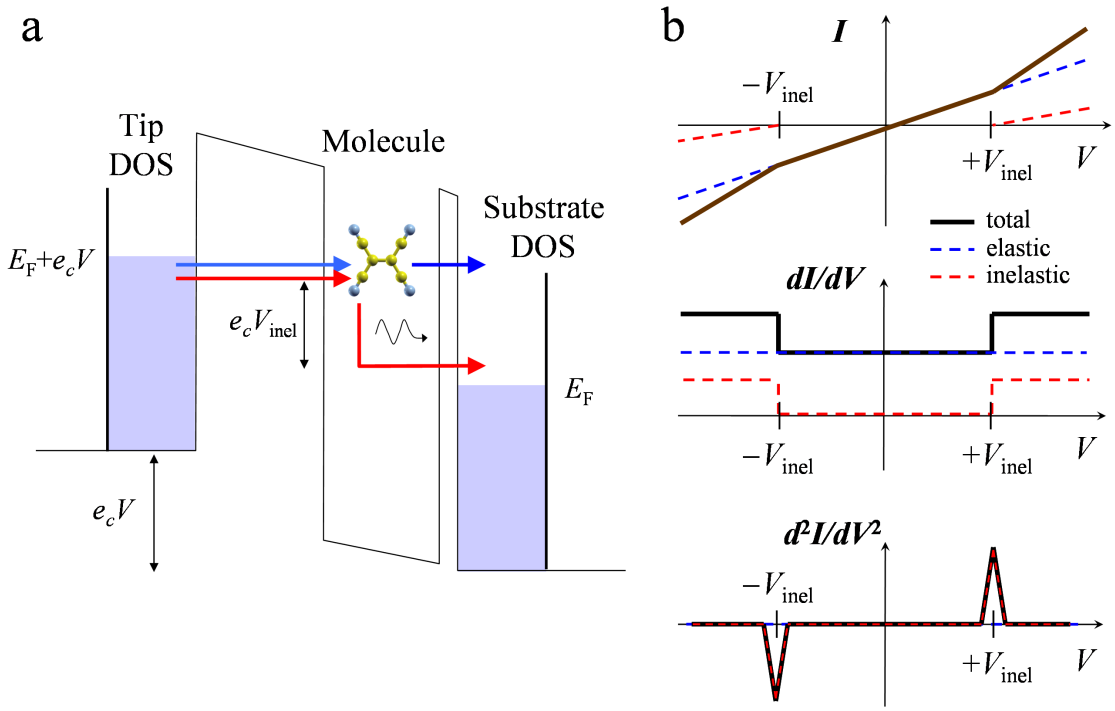

Figure 2.5: Sketch explaining why inelastic tunneling changes dI/dV symmetrically around $V = 0$. (a) Energy diagram showing possible elastic (blue arrows) and inelastic (red arrows) paths that tunneling electrons can take. (b) Elastic and inelastic contributions to $I(V)$, dI/dV, and d^2I/dV^2.

Inelastic tunneling spectroscopy was first observed in p-n junctions [77], followed by observations of molecular phonons in metal-oxide-metal tunneling junctions [85]. It was then widely used for the study of molecular vibrational properties. However, IETS on single molecules was only achieved decades later using STM and STS [171, 73]. The high spatial resolution of STM enables precise determination of the identity and arrangement of functional groups within a single molecule, as well as its adsorption site and orientation. The utilization of IETS will be discussed in chapter 4 and chapter 5 in the context of studying tetracyanoethylene (TCNE) molecules.

2.6 STM Manipulation

In addition to topographic imaging and spectroscopy acquisition, the STM can be used to manipulate atoms and molecules on the surface [38, 9, 35, 69, 72]. Different manipulation modes are schematically shown in figure 2.6. Under constant current mode, the STM tip is brought in close proximity to an adsorbate, a weak chemical bond is formed between the tip and the sample, depending on the force between the tip and the sample, the adsorbate can be pulled, slided, or pushed by the tip (figure 2.6a). There are other less common methods such as constant-height mode (figure 2.6b) and vertical manipulation mode (figure 2.6c) [10].

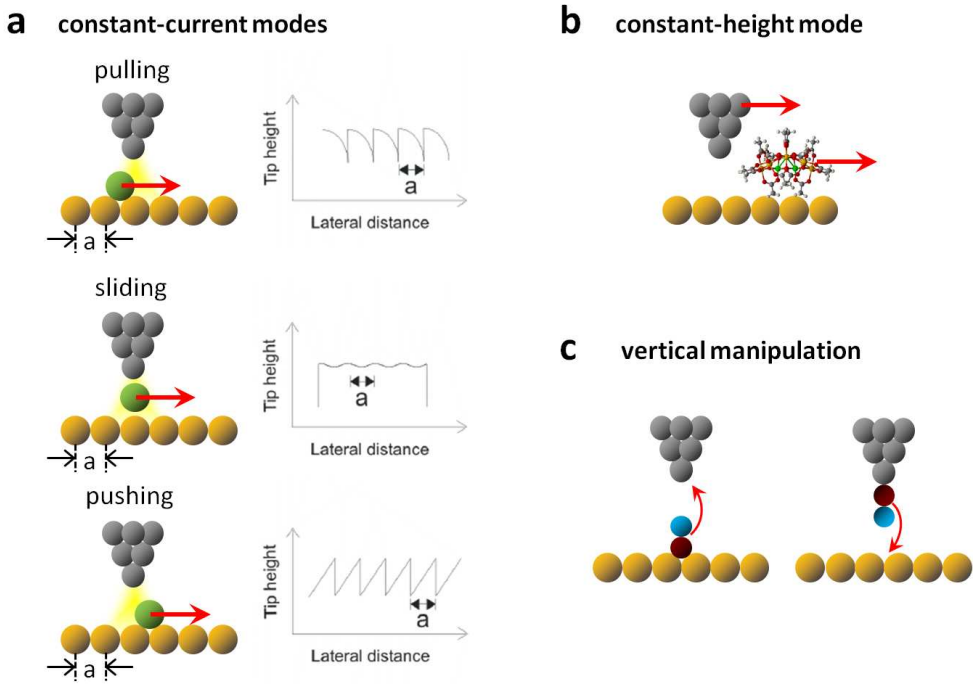

Figure 2.6: Diagrams of STM manipulation. (a) Different manipulation schemes under constant current mode. (b) Constant height mode for moving large molecules. (c) Vertically manipulating a molecule by picking it up and putting it down at other place.

The STM manipulation capability has been exploited to build patterns that modify the electronic structure of the underlying surfaces [35], and also carry out chemical reactions at the ultimate, single molecule scale by forcing atoms and molecules together [107, 71, 191, 159, 184, 126, 111]. In chapter 4, the method of building vanadium-tetracyanoethylene via STM manipulation will be presented.

3 Instrumentation

3.1 The Scanning Tunneling Microscope Instrument

Most of the experiments presented in this thesis were conducted using a home-built ultra-high vacuum (UHV) STM. This STM has a base pressure of $\sim 1 \times 10^{-10}$ torr and a base temperature of ~ 7 K. The original STM design and construction was carried out by M. F. Crommie, W. Chen, and V. Madhavan. Details of the STM design and improvement have been presented in the theses of Wei Chen [29], Vidya Madhavan [118], Tiberiu Jamneala [87], Michael Grobis [62], Xinghua Lu [116], and Ryan Yamachika [192]. Only a brief description will be given here.

Figure 3.1 shows an overview of the STM. The various parts of the system can be broken down into the following components:

1. UHV chambers and pumping systems
2. cryogenic system
3. vibrational isolation
4. STM scanner
5. electronics and software

A brief description of each component will be given below.

3.1.1 UHV Chambers and Pumping Systems

The system's chambers consist of four major parts: an analysis chamber, a transfer chamber, a microscope chamber, and a load-lock chamber. Each chamber has different functionality. The analysis chamber is mainly used for sample preparation, such as cleaning samples (§3.2.1) and depositing insulating layers (§3.2.2). It is equipped with a sputter

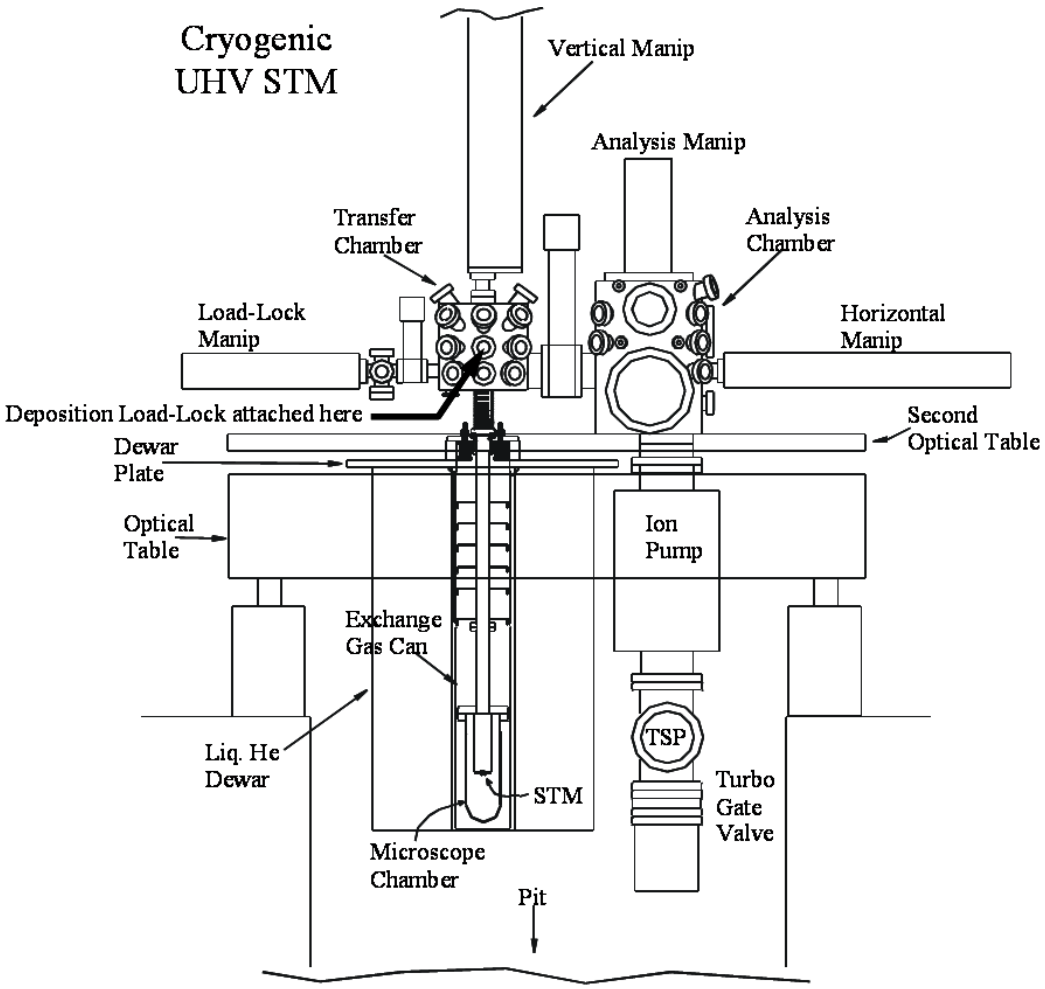

Figure 3.1: Overview of the STM chambers, pumping system, and cryogenic system.

gun, an electron-beam heater, a low energy electron diffraction (LEED) unit, and an Auger electron spectrometer. The transfer chamber is used for transferring sample between the analysis chamber, the microscope chamber and the load-lock chamber. It is equipped with metal electron-beam evaporators and molecule evaporators, so most of the atom/molecule deposition is performed in the transfer chamber. The STM scanner is located in the microscope chamber. Samples are transferred between ambient and UHV through the load-lock chamber. Sometimes we carry out molecule deposition in the load-lock chamber for added flexibility.

The chambers and pumping systems allow for a base pressure of $\sim 1 \times 10^{-10}$ torr. The chambers are made from 304 stainless steel to allow for baking above 100 °C during initial pump down and for low outgassing once at UHV. A combination of a 500 l/s turbo pump and a diaphragm-backed turbo pumping station is used to bring the system from ambient conditions to high vacuum. The turbo pumping system also pumps the system during bake-

out, which lasts $3-5$ days. During normal operation, the chambers are pumped by two ion pumps (a 75 l/s pump in the transfer chamber and a 500 l/s pump in the analysis chamber) and occasional running of the titanium sublimation pumps (TSPs).

3.1.2 Cryogenic System

The microscope chamber sits inside an 80 liter liquid He dewar. The hold time for this dewar is 12 days. A He exchange gas can separate the chamber from direct contact with the liquid He. The use of He exchange gas is important for three reasons, (1) minimize vibrations from liquid He boil off, (2) avoid the Paschen effect, i.e., avoid pressure ranges (~ 100 mTorr) where high voltage arcing can occur, and (3) control desired operating temperature. A series of radiation shields in the exchange can are employed to minimize the thermal radiation from the transfer chamber, which is at room temperature, from getting to the microscope chamber. All the wires in the exchange gas can that run from room temperature down to the microscope chamber are stainless steel coaxial cables to reduce heat loss since stainless steel has low thermal conductivity. This cryogenic setup allows operation at a base temperature of 7 K when the exchange gas pressure is ~ 5 mTorr of He gas.

3.1.3 Vibration Isolation

Extensive care is taken to minimize vibrational coupling to the STM. The UHV chambers are mounted on a dual stage optical table with vibrational isolation legs between each stage. The microscope chamber is suspended by two bellows which allow for acoustic mismatch between the transfer chamber and microscope chamber. The whole UHV system is enclosed in a sound proof room to minimize acoustic disturbances. Under normal conditions, ambient vibrational disturbances do not limit the noise. Though typically 3 mÅ rms of "vibrational" noise can be seen on the tip, this noise is thought to be electronic in origin. Even with this noise, high quality images can be readily achieved with 0.5 pA stabilization currents.

3.1.4 STM Scanner

The heart of the STM, where most experimental data is taken, is the STM scan stage (located in the microscope chamber). Figure 3.2 shows the schematics of the STM scanner and stage. The STM scanner, called "the bug", consists of a series of carefully machined macor pieces (body and support), piezoelectric (piezo) ceramics (coarse and fine motion), and a shielded metallic tip (shield cannot be seen in the figure). Fine (50 μm) gold wires bring electrical contact to the various STM components. The scanner rests on a piece called the walker plate. The plate consists of a thin glass plate (75 μm thick) below which reside a series of metallic electrodes, and below which lies another glass plate (not shown in figure 3.2). The electrodes are used for (1) clamping the bug electrostatically to the glass plate and (2) coarse motion of the bug along the glass plate. The STM tip is made from either W

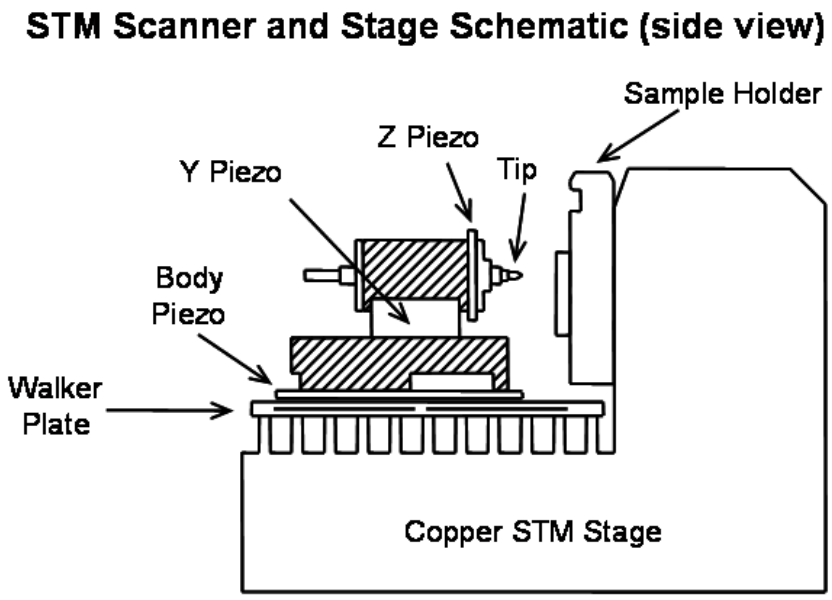

Figure 3.2: STM stage and scanner. The X piezo lies directly behind the Y piezo in this view and cannot be seen in the diagram. The sample receiver (the part that holds the sample holder) is not shown in the diagram.

or PtIr(80:20) wire (10 mil thick). Since a sharp tip apex is desired, it is common practice to chemically etch the tip [162].

3.1.5 STM Electronics and Software

The essential STM functionality is controlled by a combination of home-built electronics boxes (Z-Box, XY-Box, FE Box, Walker Box, Ground breaking box), commercial electronics (Ithaco 1211, Electronic Development Corporation 522, Data Precision 8200), and computer DAQ boards (GPIB, NI PCI-6052E, NI PCI-MIO16XE) all controlled by a central computer. In addition to the essential electronics, there is additional commercial electronics to do spectroscopy (HP 33120A function generator, Princeton Applied Research 5210 lock-in amplifier), an STM temperature controller (LakeShore 340), and a home-built audio box to aid with atomic/molecular manipulation (built by the UC Berkeley Physics Electronics Shop, Job #98-05).

All of the electronics for the STM is controlled by home-written software. The original version of the software was written in LabView, but since around 2002, newer versions have been written in C++. Nate Jenkins wrote most of this software with help from Mike Grobis. Yuri Zuev, Ryan Yamachika, Yen-Chia Chen, and I have corrected bugs and added new features to the software.

3.1.6 Coarse Approach and Fine Motion

Coarse motion is achieved by a series of electrical pulses on the body piezo and walker plate electrodes. For example, for the scanner to move forward, a complete cycle involves the following actions:

1. Apply high voltages ($\sim 500\,\mathrm{V}$) to the two back electrodes, to clamp the rear of the body piezo.
2. Remove any high voltage on the body piezo, to expand the body piezo forward since its back is clamped.
3. Apply high voltages to the front two electrodes, to clamp the front of the body piezo.
4. Remove high voltages on the back electrodes, to release the rear of the body piezo.
5. Apply high voltage on the body piezo, to contract the body piezo.

This entire sequence is called one step. Typical step sizes at $T = 7\,\mathrm{K}$ vary between $0.1\,\mu\mathrm{m}$ to $1\,\mu\mathrm{m}$ depends on the performance of the walking. The STM bug can move both perpendicular and parallel to the sample. To move the STM bug to a desired location, one takes as many steps as necessary in the correct direction.

Coarse Approach – Field Emission

The coarse movement step size ($\sim 0.1\,\mu\mathrm{m} - 1\,\mu\mathrm{m}$) is typically larger than the range of the Z-piezo ($\leq 0.1\,\mu\mathrm{m}$). This means that we can easily crash into the surface with one coarse step forward if we do not know how close the STM is to the surface. To roughly monitor the tip-sample distance, a process called "field emission" (FE) is used during coarse approach. By applying a high voltage to the tip, we may get a small current, we use feedback circuits to maintain a constant current, then in the FE regime, the tip voltage decreases as the distance decreases. The magnitude of the current and voltage gives us an idea of how far away the tip is from the surface. At the initial stage, the voltage applied to the tip is the maximum voltage $\sim -450\,\mathrm{V}$ when the tip is far (a few mm) from the surface and $I = 0\,\mathrm{nA}$. When the tip is $\sim 80\,\mu\mathrm{m}$ from the surface, $V_{tip} \sim -450\,\mathrm{V}$ and $I \sim 1\,\mathrm{nA}$. When $V_{tip} \sim -30\,\mathrm{V}$ and $I = 1\,\mathrm{nA}$, the tip is a few angstroms from the sample, and one may manually use the Z-piezo to move the tip towards the sample from that point on.

Coarse Approach – Capacitance Approach

Approaching a sample using field emission can destroy a spot due to the large voltages and electric fields required. This is why a more gentle method of approaching is necessary. Since the tip and sample form a capacitor, by measuring the tip-sample capacitance, we get an idea of how close the tip is to the surface. The tip-sample capacitance is measured by applying an ac voltage ($1\,\mathrm{V}$, $1\,\mathrm{kHz}$) to the tip and measuring the induced current in the

sample through the Ithaco 1211 current to voltage converter. Output of the Ithaco 1211 then goes to a lock-in, whose output is proportional to the tip-sample capacitance. When the tip is several angstroms away from the sample, the typical R output of the lock-in will be $70 - 80\,\mathrm{mV}$ when the Ithaco 1211 has a $10^{-10}\,\mathrm{A/V}$ gain and 1 ms time constant.

Fine Motion – Tunneling

Once the tip is within 20 nm of the surface, the electrodes clamping voltages are fixed and the remaining distance is traversed using the z-piezo. The voltage on the tip is lowered below the field-emission threshold and into the tunneling regime (within $\pm 3\,\mathrm{V}$). The feedback circuit is switched from controlling the tip voltage to controlling the z-piezo extension to keep the tunneling current constant. The fine motion of the tip is now controlled by x-, y-, and z-piezos. These three piezos have mutually orthogonal expansion axes, with the z-piezo's axis aligned roughly perpendicular to the surface. The z-piezo expands $\sim 1\,\mathrm{Å/V}$ while x- and y-piezos expand $\sim 10\,\mathrm{Å/V}$. They allow for sub-angstrom positioning of the tip along the surface. The scan range of the STM tip is about $500\,\mathrm{nm} \times 500\,\mathrm{nm}$.

3.2 Sample Preparation

Preparing clean and flat surfaces of substrates is critical for studying the intrinsic properties of molecules since impurities on the substrates may affect the properties of the molecules on them. For this reason, we clean and keep the samples under UHV of a base pressure $\sim 2 \times 10^{-10}\,\mathrm{torr}$.

3.2.1 Sputtering and Annealing

For single crystal noble metal substrates (Ag, Au, Cu), the cleaning procedures include standard repeated cycles of sputtering and annealing [128]. Argon sputtering bombards the surface with Ar^+ ions of kinetic energy between 0.5 keV and 2 keV, removing impurities on the surface. The sputtering is followed by annealing the substrate, which is heated to desorb impurities from the surface and to smooth out the surface. Annealing is done by electron-beam heating, where high energy ($\sim 1\,\mathrm{keV}$) electrons bombard the substrate and lose their energy in the form of heat. The mechanism of e-beam heating is similar to the mechanism of e-beam evaporation (§3.3.2).

3.2.2 Thin Insulating Layers

The use of an STM requires a non-insulating substrate in order for electrons to tunnel. However, the electronic structure of the adsorbates can be perturbed by underlying substrate electrons. To study the inherent properties of adsorbates, it is desirable to decouple them from the supporting substrate. We have tried and succeeded to grow epitaxial ultra-thin NaCl and CuN insulating layers to do this. Their growth methods are described below.

NaCl Islands

NaCl islands are grown by direct deposition of NaCl molecules. We use Knudsen cell evaporators (§3.3.1) to do the deposition. We first degas NaCl molecules to $550 - 555\,^{\circ}\mathrm{C}$ for a few seconds, then deposit at $\sim 540\,^{\circ}\mathrm{C}$. Figure 3.3 shows typical NaCl islands on Ag(100), depends on the coverage, they form two or three layer islands.

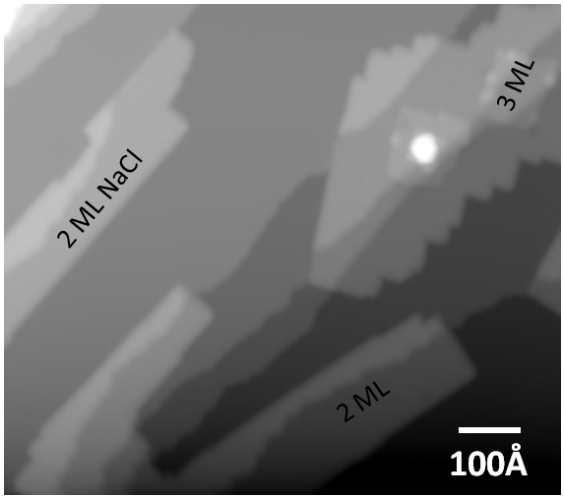

Figure 3.3: NaCl islands on Ag(100).

CuN Islands

CuN islands are grown by impinging N^+ ions onto a Cu(100) surface. More specifically, in our system, we usually sputter with N_2 pressure $\sim 1 \times 10^{-5}\,\mathrm{torr}$, ion energy of $0.5\,\mathrm{keV}$, for 20 minutes. This recipe results in $\sim 40\%$ coverage of CuN islands. Figure 3.4 shows a typical STM image of CuN/Cu(100), CuN form discontinuous islands because of the lattice mismatch between CuN and underlying Cu(100).

3.3 Deposition Techniques

In our experiments involving the study of different nanostructures via STM, a key step is to grow those nanostructures on a substrate. Depending on the size, form, and properties of the materials, we have developed various deposition techniques. This section will introduce common methods used in our experiments.

3.3.1 Knudsen Cell Evaporator

For molecules that can be sublimated in ultra high vacuum at temperatures above room temperature, we employ a Knudsen cell evaporator to thermally deposit them. Figure 3.5

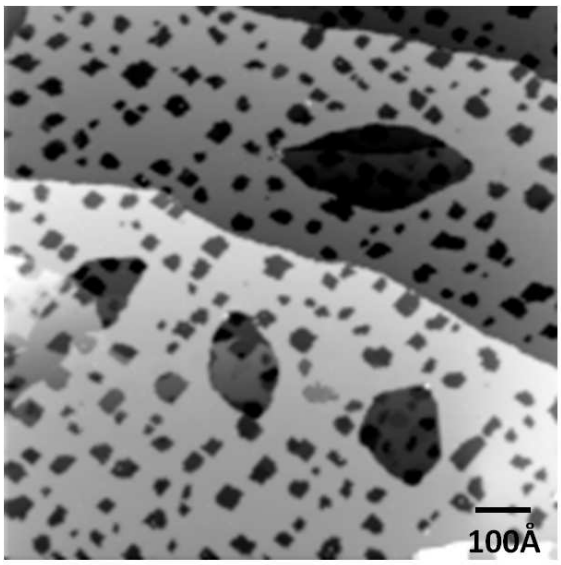

Figure 3.4: CuN islands on Cu(100).

shows the design of a Knudsen cell evaporator, a detailed description of the design can be found in Mike Grobis' thesis [62].

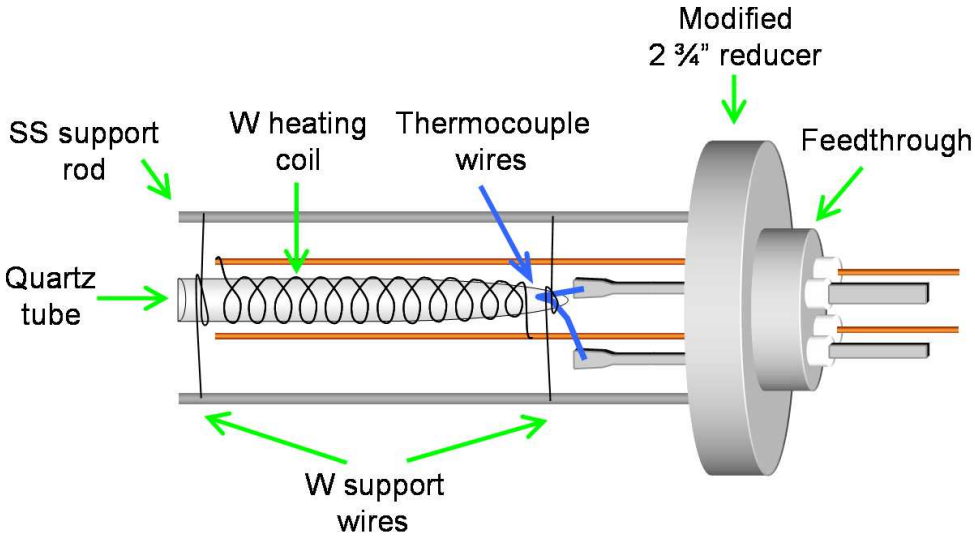

Figure 3.5: Schematics of a Knudsen cell evaporator.

To use the evaporator we put molecules into the central quartz tube, and then heat it by running a current through the tungsten heating coil. The temperature is measured by the thermalcouple, allowing us to evaporate molecules at any desired temperature. The temperature determines the molecular vapor pressure, and in this way we are able to control the amount of the molecules on the surface.

3.3.2 Electron Beam Evaporator

For depositing metals, which usually have much higher evaporation temperatures than molecules (higher than the melting point of the quartz crucible in the Knudsen cell), a Knudsen cell cannot be used. A different evaporator, called an *electron beam evaporator*, or e-beam evaporator is then utilized. Figure 3.6 shows the schematics of the e-beam heater designs. The feedthrough is usually a TSP feedthrough that can handle large currents and high temperatures. The filament is either thoriated tungsten wire, which begins to glow when $\sim 2\,\mathrm{A}$ is passed through it, or a Granville-Phillips ion gauge filament, which requires $\sim 5\,\mathrm{A}$ to glow. The metal is either directly attached to a Mo rod by wrapping W wire around it and the Mo rod (figure 3.6a), or one end of a wire (W, Mo, or Ta) is wrapped around and spot welded to the metal while the other end of the wire is wrapped around and spot welded to the Mo rod (figure 3.6b). The second method (figure 3.6b) has the advantage that there is less heat loss to the Mo rod since there is no direct contact between the hot metal and the Mo rod, which means less current is needed in the filament and the Mo rod will outgas less. However, this method has the disadvantage that when the metal and the wire get hot, they can bend and touch the shield, causing a short, that's why we developed the first method (figure 3.6a). A shield (drawn transparent in figure 3.6a) is normally placed around the metal and filament for two reasons, (1) it prevents metal from being evaporated in all directions, which prevents the metal from contaminating other evaporators or covering viewports; (2) it also changes the local electric field around the metal, the shield can significantly alter the number of atoms that fly towards the sample.

To use the evaporator, a high voltage ($2\,\mathrm{kV}$) is applied to the metal which we want to deposit, by running a current through the filament that near the high voltage metal, thermally emitted electrons are accelerated to the metal because of the high voltage on it. Those electrons hit the metal and release their energy in the form of heat, rapidly heating the metal. By controlling the current that flows from the filament to the metal through vacuum (called the emission current), we are able to control the temperature of the metal.

3.3.3 K Getter Evaporator

The deposition of K atoms is more difficult due to the high reactivity of K when exposed to moisture in the air. For the deposition of K atoms, K getters were purchased from SAES getters in Milan, Italy. To use these getters, a current of $\sim 5 - 8\,\mathrm{A}$ is passed through the getter, which causes K atoms to be released.

3.3.4 Leak Valve Evaporator

For depositing TCNE, since it sublimates at room temperature, a different method that employs a leak valve was used. Figure 3.7 shows a basic setup of a leak valve evaporator. The molecules are placed in a small glass belljar which is attached to a UHV leak valve. The leak valve is attached to the UHV chamber.

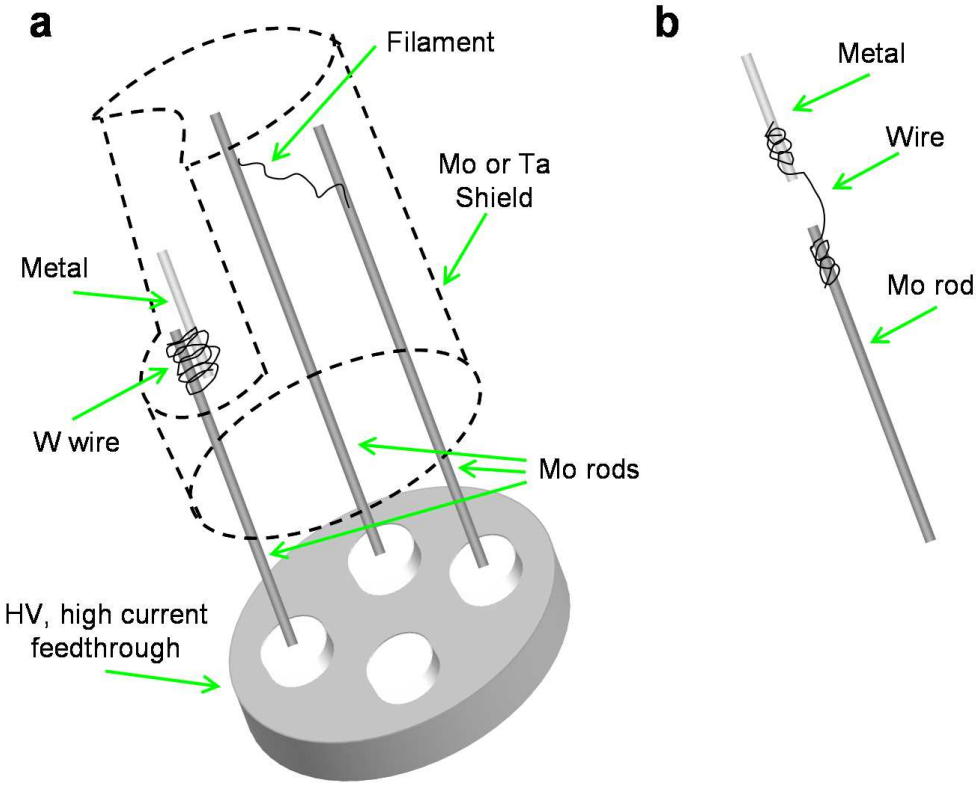

Figure 3.6: *e*-beam evaporator setup. (a) Complete schematic of an *e*-beam evaporator with the metal directly attached to the Mo rod and the shield is drawn transparent. (b) A second way of attaching the metal to the Mo rod by using a W, Mo, or Ta wire.

Because of the high vapor pressure of TCNE molecules at room temperature, the air in the belljar cannot be pumped directly through the UHV chamber's pumping systems, another method called "pump and flush" is used to clean the initial air enclosed in the belljar. A Tee fitting is attached to the belljar, the leak valve, and a pump/flush valve. The belljar is first pumped to rough vacuum ($\sim 10\,\mathrm{mTorr}$) and then filled with 1 atm of Ar gas. Note that since TCNE is toxic, when pump on it, the exhaust of the pump should go into a fume hood. This process of pumping and flushing with Ar needs to be repeated at least ten times to achieve the desired cleanness. Finally the belljar is pumped to rough vacuum and the pump/flush valve is closed. The TCNE at room temperature and in rough vacuum will sublimate, forming a gas of TCNE in the belljar and the leak valve. Opening the leak valve can control the molecular gas flow, thus control the molecule coverage on surfaces.

Since the TCNE gas can diffuse everywhere in the chamber, we must turn off ion gauges, ion pumps, or anything else with hot filaments or high energy electrons since they may break the molecule. Any broken molecules may end up on the sample surface, contaminating the surface.

With leak valve evaporators, we want the distance between the leak valve and the sample

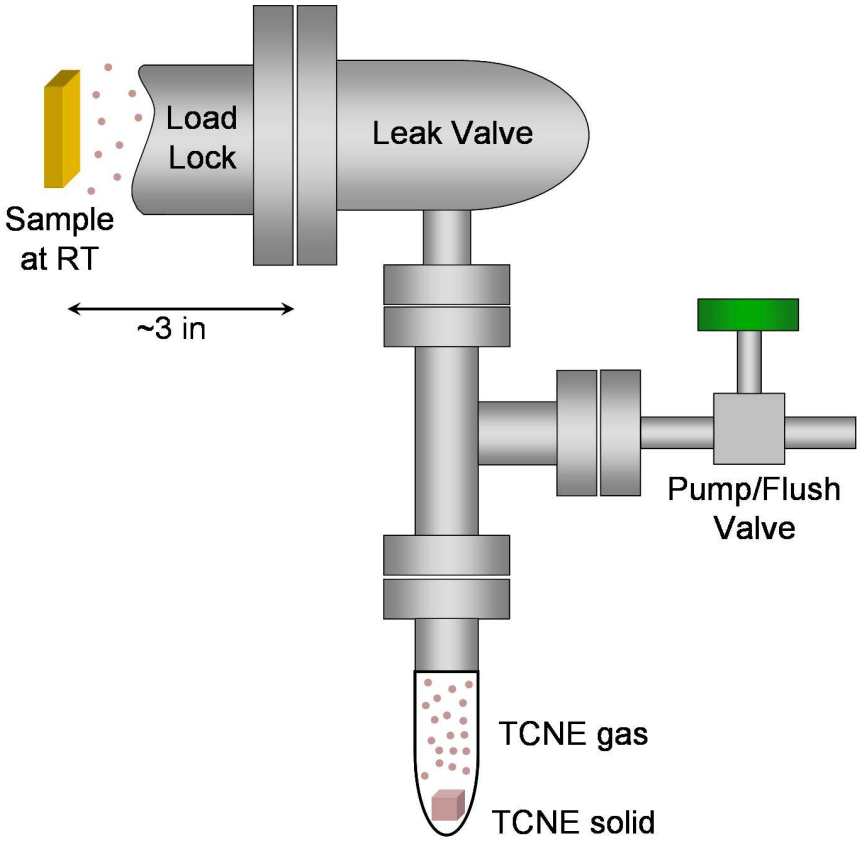

Figure 3.7: Leak valve evaporator setup for depositing TCNE onto a sample at room temperature.

to be small (a few inches) so that most of the molecules will hit the sample surface. If the distance is large, we would need higher pressure of TCNE gas to get the same amount of TCNE on the surface. Higher TCNE gas pressure means more TCNE contamination of the chamber and worse base pressure. For this reason, because of the geometry of our chamber, we developed two setups for deposition of TCNE at room temperature and low temperature.

RT Leak Valve Evaporator

We perform room temperature deposition of TCNE in the sample-transfer load lock chamber (figure 3.1). To do the deposition, after pumping and baking the load lock chamber to achieve UHV, we move the sample into the load lock and turn off ion gauges and ion pumps. When the leak valve is opened, the TCNE gas then hits the sample. The distance between the leak valve and sample is ~ 3 in in this setup (figure 3.7).

LT Leak Valve Evaporator

TCNE molecules are mobile on some surfaces at room temperature, for example, NaCl/Ag(100) (§4.3), in order to keep them isolated, we need to cool the sample to low temperature. We cannot do it in the sample-transfer load lock chamber, since the sample would rapidly warm up on the horizontal transfer manipulator. The sample can only be cooled in the transfer chamber, on the vertical transfer manipulator (figure 3.1). However, the distance between the sample and leak valve on the main chamber would be relatively large ($\sim 12\,\text{in}$) if we use the RT leak valve evaporator setup, so a different design is needed. To reduce the distance between the evaporator and sample, we attach a long threaded tube to a modified double-sided blank flange which is attached to the leak valve (figure 3.8). This modified double-sided blank flange (with knife edges on both sides) has a hole drilled completely through it and one side of the hole has 1/8" NPT threads so that we may screw a the threaded tube or pipe onto the end of it. The tube was made out of stainless steel 304. This assembly was then attached to a linear motion feedthrough which is attached to the deposition load lock (figure 3.1) on the main chamber. When the tube is completely moved toward the sample, the distance between the end of the tube and the sample is $\sim 5\,\text{in}$.

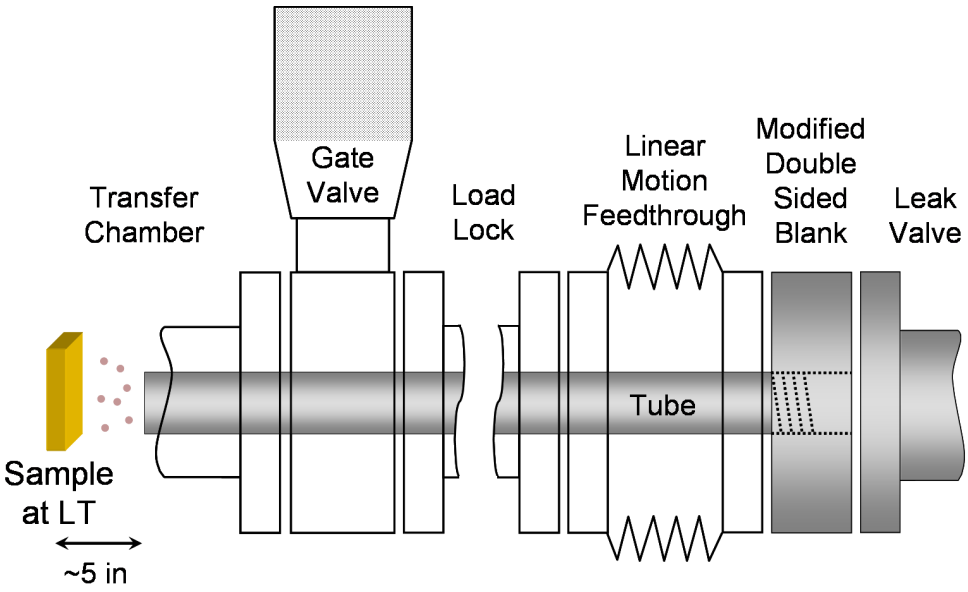

Figure 3.8: Leak valve evaporator for depositing TCNE onto a sample held at low temperature ($\sim 40 - 50\,\text{K}$). The schematic shows the evaporator when the tube has been moved toward the sample using the linear motion feedthrough. When the tube is moved sufficiently far away from the sample, the end of the tube is in the load lock, so we can close the gate valve.

To deposit TCNE with this setup,

1. Cool the sample in the STM chamber (figure 3.1) for several hours until the sample reaches 7 K.

2. Pumping and baking the deposition load lock until its base pressure cooled to room temperature is $\sim 1 \times 10^{-8}$ torr.

3. Cool the vertical manipulator with liquid N_2 for 30 minutes, then pick up the sample and move it into the transfer chamber (figure 3.1).

4. Turn off the ion gauge and ion pump in the transfer chamber.

5. Open the load lock gate valve, move the tube forward using the linear motion feedthrough.

6. Open the leak valve to deposit the molecules onto the surface.

7. After deposition, quickly put the sample back into the STM chamber. Retrieve the tube, close the load lock gate valve.

3.3.5 Spin Coating

The graphene nanoribbons (GNRs) used in our studies are produced by chemically unzipping carbon nanotubes [90]. The resulting GNRs are suspended in a 1,2-dichloroethane (DCE) organic solution of poly(*m*-phenylenevinylene- co-2,5-dioctoxy-*p*-phenylenevinylene) (PmPV). To deposit them on surfaces, we use a spin coating method. The sample is then heat treated in UHV chamber as a cleaning procedure.

Part II

Magnetic Nanostructures

4 Spin Coupling Mediated by TCNE

Molecule-based spintronics raises new possibilities for electronic and magnetic devices [20, 82]. However, for this concept to become reality, a more fundamental understanding of the interaction between the adsorbate and the substrate as well as the interaction between different spin centers, is necessary. This is due to the fact that spin coupling and magnetic anisotropy can change when molecules come into contact with each other and with a substrate [165, 8]. STM-based study of bottom-up created spin structures offers a powerful new technique to reveal local magnetoelectronic structure in these systems [28, 86, 179, 121].

To address the fundamental question of how molecules can tune spin coupling, we chose tetracyanoethylene (TCNE) as a molecular linker, and vanadium atoms as spin centers. The structure of TCNE is shown in figure 4.1. Bulk V(TCNE)$_x$ with $x \sim 2$ is the first known

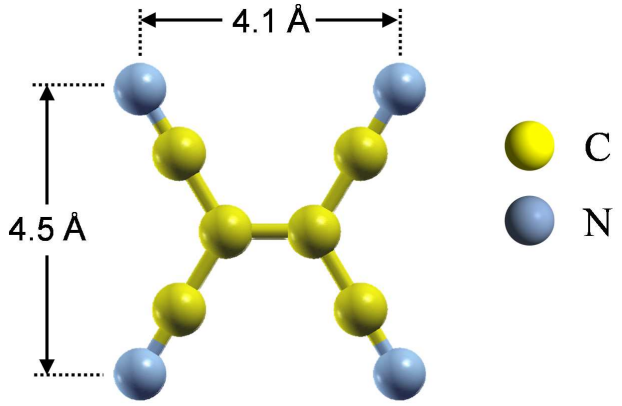

Figure 4.1: Structure of the TCNE molecule from DFT calculations.

room temperature organic magnet with a Curie temperature of around 400 K [119, 155, 175, 99], so is a good choice for spin coupling. Using STM to build and study V(TCNE) complexes helps to gain new insights into the magnetic coupling of this system.

Our approach to this issue is to use the molecular manipulation capabilities of an STM (§2.6). We manipulate TCNE and V(TCNE) and thus can control both the stoichiometry and structure of $V_x(TCNE)_y$ complexes. We then study their electronic and magnetic properties, and relate these properties with the exact structure of the complexes. We see evidence for controllable spin coupling through TCNE in $V_x(TCNE)_y$ complexes created by STM manipulation, suggesting that spin coupling can be controlled at atomic length scales. This result is based on our published paper, ref [184].

4.1 TCNE on Ag(100)

In order to build $V_x(TCNE)_y$ structures, we first needed to find a substrate where we could do manipulation, since there is not much previous work exploring TCNE on different substrates [41, 42, 139]. After trying various substrates, we found that Ag(100) works well for manipulating TCNE. The Ag(100) single crystal was cleaned by standard sputter-annealing proceedures and then exposed at $T = 300\,\mathrm{K}$ to TCNE molecules dosed through a leak valve (§3.3.4). The sample was then transferred *in situ* into the cryogenic STM.

For low coverage of TCNE on Ag(100), the molecules saturate step edges, but isolated monomers can be seen on terraces, as shown in figure 4.2a. Each isolated molecule appears as an oval protrusion ($\sim 6\,\text{Å} \times 7\,\text{Å}$) with a dark ring ($\sim 12\,\text{Å}$ in diameter) around it. STS performed on single TCNE/Ag(100) adsorbates reveals a broad HOMO state at $-0.6\,\mathrm{eV}$ (figure 4.2b). No other peaks are observed between -1.5 and $+2.5\,\mathrm{eV}$ relative to E_F. dI/dV mapping of individual TCNE molecules at the HOMO energy reveals many single molecule features not apparent in STM topography images: whereas the STM topograph (figure 4.2c) is a broad oval, the HOMO dI/dV map (figure 4.2d) shows a bright, elongated body that is intersected by a central line node and surrounded by four legs.

To model the observed molecular orbital, DFT calculations were performed on isolated neutral and negatively charged TCNE molecules ($TCNE^0$, $TCNE^-$, $TCNE^{2-}$) using the SIESTA code with a double-ζ basis set and the local density approximation. Figure 4.3 compares the calculated HOMO isosurfaces of $TCNE^0$ and $TCNE^{2-}$ with the experimental HOMO dI/dV map of TCNE/Ag(100). (The calculated singly occupied molecular orbital (SOMO) isosurface of $TCNE^-$ and the LUMO of $TCNE^0$ were all found to be structurally identical to the HOMO of $TCNE^{2-}$.) Although the HOMO of $TCNE^0$ shows an antinode in the molecule center, the HOMO isosurface of $TCNE^{2-}$ shows pronounced nodes across the central C=C bond and the four C≡N triple bonds. The overall shape of the theoretical $TCNE^{2-}$ HOMO isosurface is in very good agreement with the experimental dI/dV map of the HOMO state of TCNE/Ag(100) imaged at $-0.6\,\mathrm{V}$ (figure 4.3c). Therefore, we conclude that TCNE is negatively charged (i.e., either $TCNE^-$ or $TCNE^{2-}$) on Ag(100) due to charge transfer from the substrate, which is likely since TCNE is know to have a high electron affinity ($\sim 3\,\mathrm{eV}$). We can also confirm the orientation of TCNE on Ag(100) as drawn in the structural model of figure 4.2e.

To manipulate (slide) TCNE/Ag(100) requires a closer tip-surface interaction, with typ-

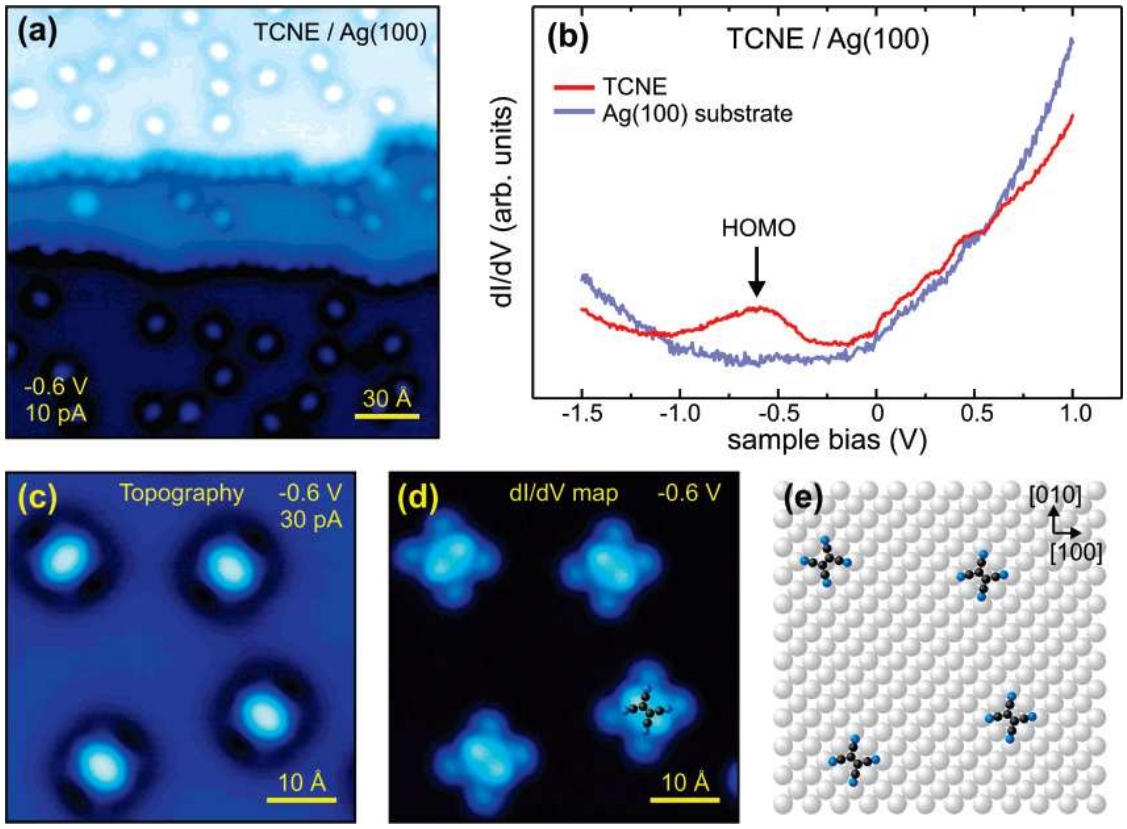

Figure 4.2: TCNE on Ag(100). (a) Topography at $V = -0.6\,\mathrm{V}$, $I = 10\,\mathrm{pA}$. (b) dI/dV spectroscopy of TCNE on Ag(100), showing the HOMO resonance at $V = -0.6\,\mathrm{V}$. (c) Topography of four TCNE molecules, $V = -0.6\,\mathrm{V}$, $I = 30\,\mathrm{pA}$. (d) dI/dV map at $V = -0.6\,\mathrm{V}$ (the HOMO energy). (e) Structural model of the images in (c) and (d).

ical sliding parameters being $V \sim 5\,\mathrm{mV}$, and $I \sim 1 - 2\,\mathrm{nA}$. TCNE molecules follow the tip trajectory, and can be moved with great precision.

4.2 $V_x(TCNE)_y$ Complexes

Once we found that Ag(100) works the best for manipulation, we created various $V_x(TCNE)_y$ structures. We deposited V atoms onto the cold sample using electron-beam evaporation (§3.3.2). Typical STM topographs of TCNE and V on Ag(100) is shown in figure 4.4a and d. V atoms appear as round protrusions on Ag(100) terraces.

While isolated V adatoms cannot be moved on Ag(100), TCNE molecules can be slid towards the V atoms using the sliding technique. After TCNE is attached to a V atom, the formed V(TCNE) complex displays a strong change in apparent height (figure 4.4b, e). Once merged, the entire fused V(TCNE) complex can be moved as a single unit along the surface by STM manipulation (figure 4.4e).

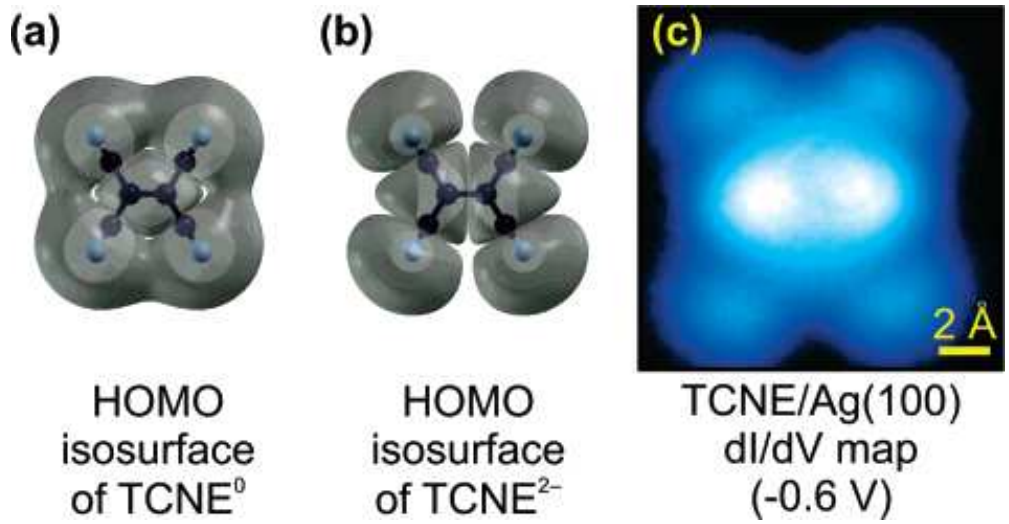

Figure 4.3: DFT calculated isosurfaces for the HOMO of (a) TCNE and (b) $TCNE^{2-}$, with (c) the experimental dI/dV map of the HOMO as a comparison.

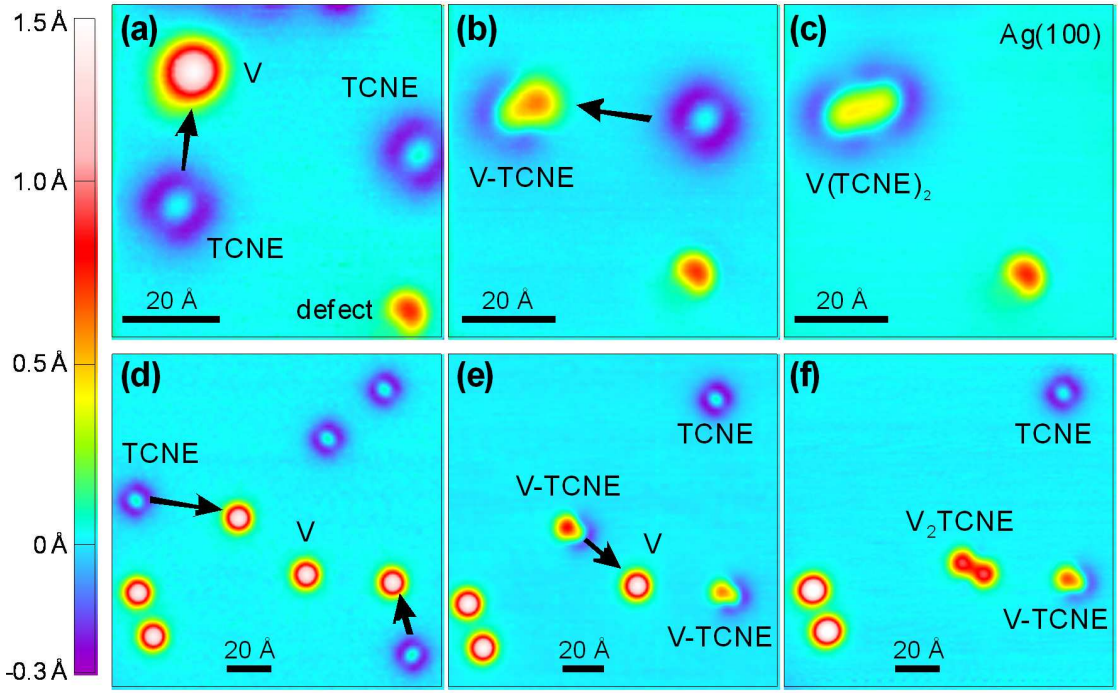

Figure 4.4: Construction of $V_x(TCNE)_y$ on Ag(100) using molecular manipulation. (a)–(c): formation of $V(TCNE)_2$ ($V = 1\,V$, $I = 5\,pA$). (d)–(f): formation of trans-$V_2(TCNE)$ ($V = 1\,V$, $I = 10\,pA$).

Larger $V_x(TCNE)_y$ structures can be built reliably by connecting TCNE or V(TCNE) with other building blocks. Figure 4.4a–c show constructing $V(TCNE)_2$ by attaching a TCNE to a V(TCNE), and figure 4.4d–f show the process of attaching a V(TCNE) to another V atom to form a $V_2(TCNE)$. There are other different structures built by the manipulation technique (figure 4.5). It is worth noting that there are various different stable isomers for

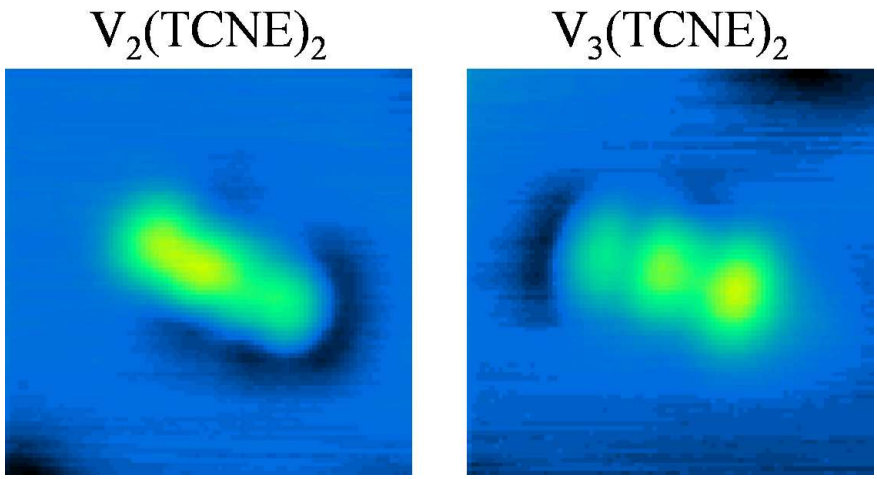

Figure 4.5: 4 nm × 4 nm topographs of $V_2(TCNE)_2$ ($V = 0.1\,V$, $I = 30\,pA$) and $V_3(TCNE)_3$ ($V = 0.1\,V$, $I = 30\,pA$).

each $V_x(TCNE)_y$ complexes. A particular isomer can sometimes be obtained by carefully controlling the manipulation process, but often an undesired isomer is constructed instead. This lack of complete control makes it difficult to reproducibly create large $V_x(TCNE)_y$ structures, and makes it harder to get good statistics on each structure. However, for smaller $V_x(TCNE)_y$ structures, there are fewer possible ways for V atoms to attach to TCNE molecules, making it easier to get reproducibility.

We have mainly built and studied four different $V_x(TCNE)_y$ complexes, namely, V(TCNE) (figure 4.6a), $V(TCNE)_2$ (figure 4.6b), trans-$V_2(TCNE)$@27° (figure 4.6c), and trans-$V_2(TCNE)$@11° (figure 4.6d). The angle of the trans-$V_2(TCNE)$ denotes the V-V angle relative to the [001] direction of the substrate. These two isomers exhibit an overall difference in size, the distance between V atoms being slightly larger (by ~ 1 Å) in the $V_2(TCNE)$@27° molecule as compared to the shorter $V_2(TCNE)$@11°. Figure 4.6 also shows structural models, which are derived from atomic resolution images of these structures.

In order to understand the magnetoelectronic behavior of the newly synthesized $V_x(TCNE)_y$ complexes, we performed STS experiments on these structures with subnanometer resolution (figures 4.7 and 4.8). Three different features are observed in the spectroscopy: (i) molecular orbital resonances, (ii) vibrational inelastic features, and (iii) Kondo resonances. Molecular orbital resonances are seen at "high" biases ($|V| > 100\,mV$), while inelastic features are seen at "low" biases ($|V| < 50\,mV$), and Kondo resonances are observed to straddle the Fermi energy at $V = 0$.

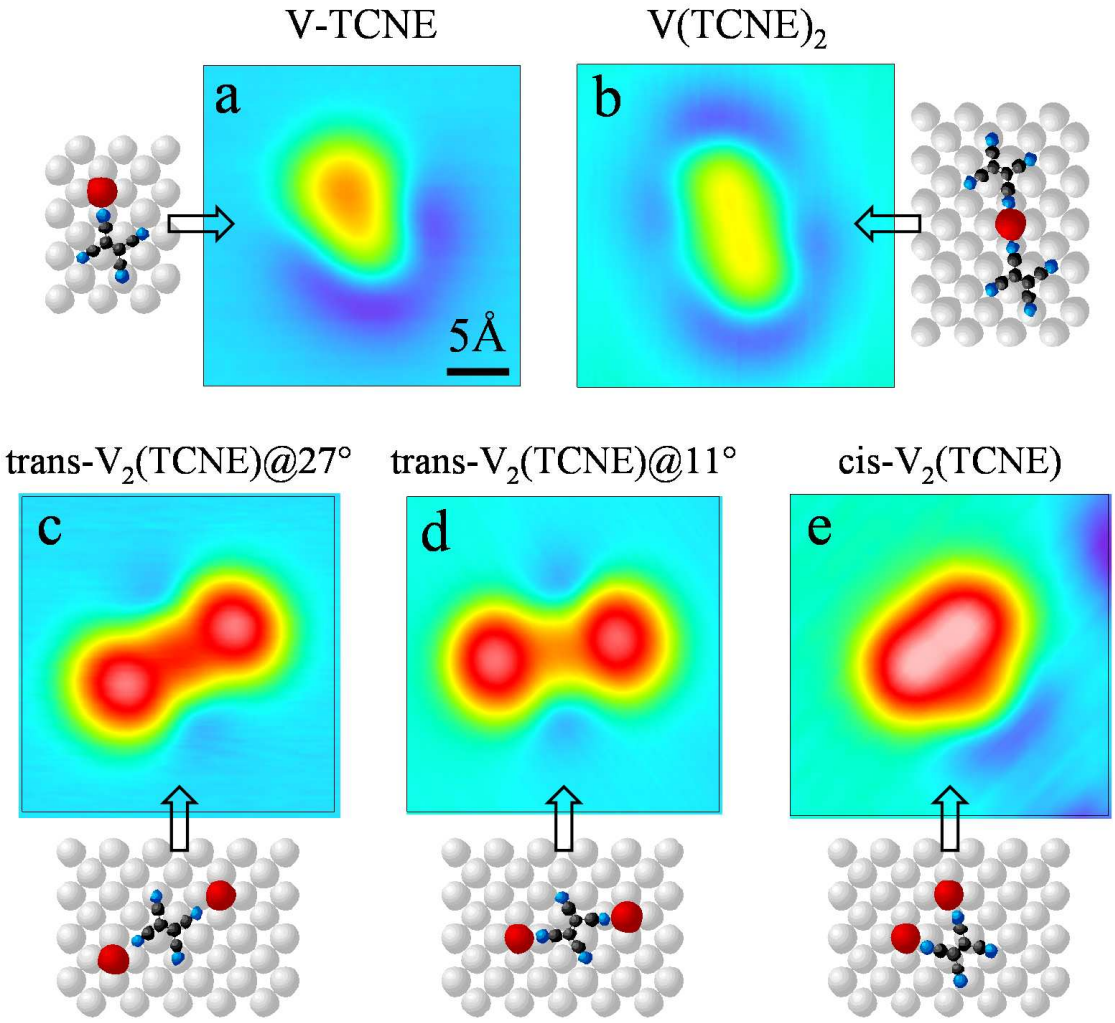

Figure 4.6: Highly resolved STM images and structural models of (a) V(TCNE) ($V = 1\,\mathrm{V}$, $I = 10\,\mathrm{pA}$), (b) $V(TCNE)_2$ ($V = 1\,\mathrm{V}$, $I = 5\,\mathrm{pA}$), (c) trans-V_2(TCNE)@27° ($V = 1\,\mathrm{V}$, $I = 50\,\mathrm{pA}$), (d) trans-V_2(TCNE)@11° ($V = 1\,\mathrm{V}$, $I = 5\,\mathrm{pA}$), and (e) cis-V_2(TCNE) ($V = 1\,\mathrm{V}$, $I = 5\,\mathrm{pA}$) on Ag(100). The models are derived from the STM images.

Spectroscopy done at high biases shows the orbital resonances for $V_x(TCNE)_y$ complexes. In the data of figure 4.7, these resonances are marked by the label "E_d", since they are believed to arise from V d orbitals. STS of V-TCNE complexes (figure 4.7a) shows a pronounced broad molecular resonance at $E_d = -0.17\,\mathrm{V}$ that has strong amplitude on the V site and slightly lower amplitude on the TCNE region of the complex. This resonance does not exist for bare TCNE on Ag(100) (figure 4.2b). When two TCNE molecules are attached to a single V atom, the orbital resonance shifts to a slightly reduced energy $E_d = -0.25\,\mathrm{V}$ (figure 4.7b) and becomes localized to the V atom and cannot be seen over adjacent TCNE molecules. When two V atoms are bonded to a single TCNE molecule, the molecular orbital

shifts upward slightly to $E_d = -0.15\,\mathrm{V}$ and has amplitude on both the V and the TCNE regions of the complex. This behavior is seen identically for both trans-V_2(TCNE).

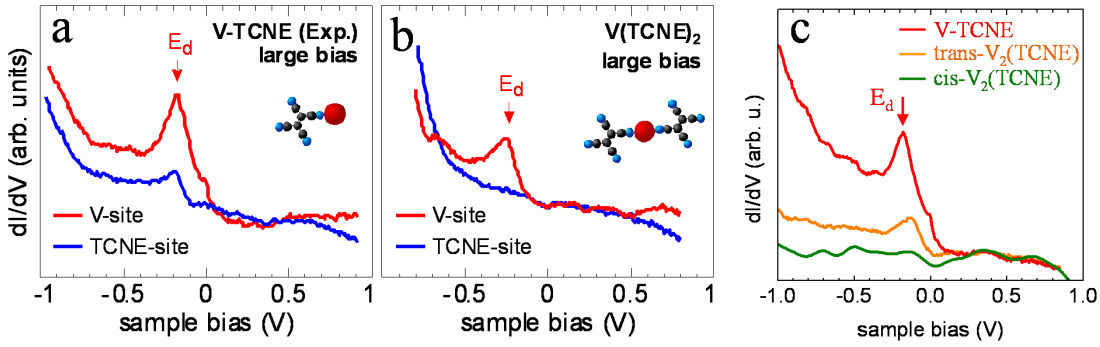

Figure 4.7: Large bias spectroscopy on (a) V(TCNE), (b) $V(TCNE)_2$, and (c) a comparison of spectroscopy between V(TCNE), trans-V_2(TCNE) and cis-V_2(TCNE). The state around $-0.2\,\mathrm{eV}$ is believed to arise from the V d-orbital, so is denoted as E_d.

The spectroscopy done at low biases of $|V| < 80\,\mathrm{mV}$ is shown in figure 4.8. Two prominent features are seen at low biases. One is the inelastic features (marked with the label "E_{vib}" in figure 4.8). These are seen as steps in dI/dV or peaks (dips) at positive (negative) voltage in d^2I/dV^2, and they arise as new tunneling channels are opened due to molecular excitations (§2.5). For bare TCNE (figure 4.8a), a very clear inelastic mode exists at $\sim 30\,\mathrm{mV}$. We identify this as the TCNE rocking or wagging mode that is known to lie at this energy from optical spectroscopy measurements and DFT calculations [124, 23]. When a single V atom is attached to a single TCNE molecule, however, a new mode appears at 45 mV that is localized to the V site (figure 4.8b). We identify this as the V-N stretch vibration, and its energy corresponds well to the V-N stretch mode measured in other structures by optical spectroscopy [6]. The presence of the V-N stretch vibration provides strong evidence that V atoms connected to TCNE via STM manipulation are covalently bonded. When two TCNE molecules are connected to one V atom, the V-N stretch mode is no longer detectable, but the TCNE rocking/wagging mode is still seen over the TCNE molecules (figure 4.8c).

Another feature in figure 4.8 is Kondo resonances. A Kondo resonance is the spectral signature of a many-body electron cloud that occurs as the itinerant spins of a nonmagnetic metal screen the spin of a local magnetic moment [109, 117]. V(TCNE) exhibits a Kondo resonance having amplitude on both the V atom and the adjacent TCNE molecule (figure 4.8b) with a width of $\Gamma = 11 \pm 2\,\mathrm{mV}$, indicating a Kondo temperature of $T_K \sim 65\,\mathrm{K}$. Figure 4.8c shows that the Kondo resonance remains for the $V(TCNE)_2$ complex ($\Gamma = 6 \pm 1\,\mathrm{mV}$, i.e., $T_K \sim 35\,\mathrm{K}$), except that it now has amplitude only on the V atom. The spatial dependence of the Kondo resonance for both V(TCNE) and $V(TCNE)_2$ thus mirrors the spatial dependence of the molecular orbital at E_d.

The situation is different when two V atoms are connected to a single TCNE molecule in the trans-V_2(TCNE) configuration. For V_2(TCNE)@27°, the high bias spectra show an

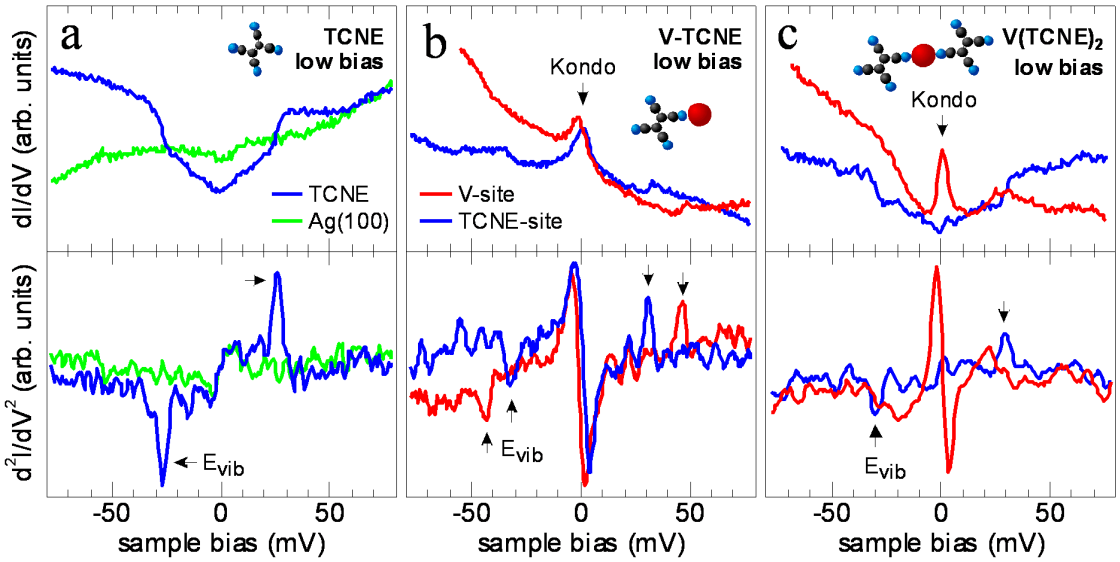

Figure 4.8: dI/dV and d^2I/dV^2 spectra of (a) TCNE, (b) V(TCNE), and (c) $V(TCNE)_2$. The inelastic vibrational mode is denoted as E_{vib}, and the resonance at the Fermi energy is denoted as Kondo resonance.

E_d resonance on both V and TCNE (figure 4.9a). At low bias, the Kondo resonance also remains (in this case, $\Gamma = 10 \pm 2\,\text{mV}$, i.e., $T_K \sim 60\,\text{K}$), and again the spatial distribution of the Kondo resonance mirrors that of the E_d orbital resonance (figure 4.9c). However, for V_2TCNE@11°, there is no Kondo resonance to be seen on either the V or the TCNE sites (figure 4.9d) despite the fact that the E_d orbital resonance amplitude remains unchanged across the entire V_2TCNE@11° complex.

To help explain the data, first-principles SP-DFT calculations of the magnetoelectronic structure of isolated $V_x(TCNE)_y$ complexes were performed using the NRLMOL code [146, 84, 147, 145]. All atoms in the calculation were treated within an LCAO formulation at the all-electron level. The basis sets used here are roughly equivalent to triple-ζ or better. The generalized gradient approximation was used to approximate the exchange-correlation functional [149]. Structures were relaxed until all forces were below 0.001 Hartree/Bohr. Figure 4.10a shows the local density of states (LDOS) calculated for a V(TCNE) complex. The majority-spin LDOS shows a pronounced filled state at $E_d = -0.20\,\text{eV}$, implying that the experimental orbital resonance seen at this same energy is a majority-spin statearising from a V d orbital. Calculations of a V_2(TCNE) complex (figure 4.10b) also show a dominating V d resonance at $E_d = -0.12\,\text{eV}$, similar to what is seen for the experimental case (figures 4.7c and 4.9a,b). This agreement between theory and experiment occurs only when the simulated V(TCNE) and V_2(TCNE) complexes are charged with one electron, which we assume is drawn from the Ag substrate in the experiment. In this case the FM state is lower in energy than the antiferromagnetic state by 170 meV. The SP-DFT calculations thus support the conclusion that orbital resonances seen experimentally at E_d indicate the

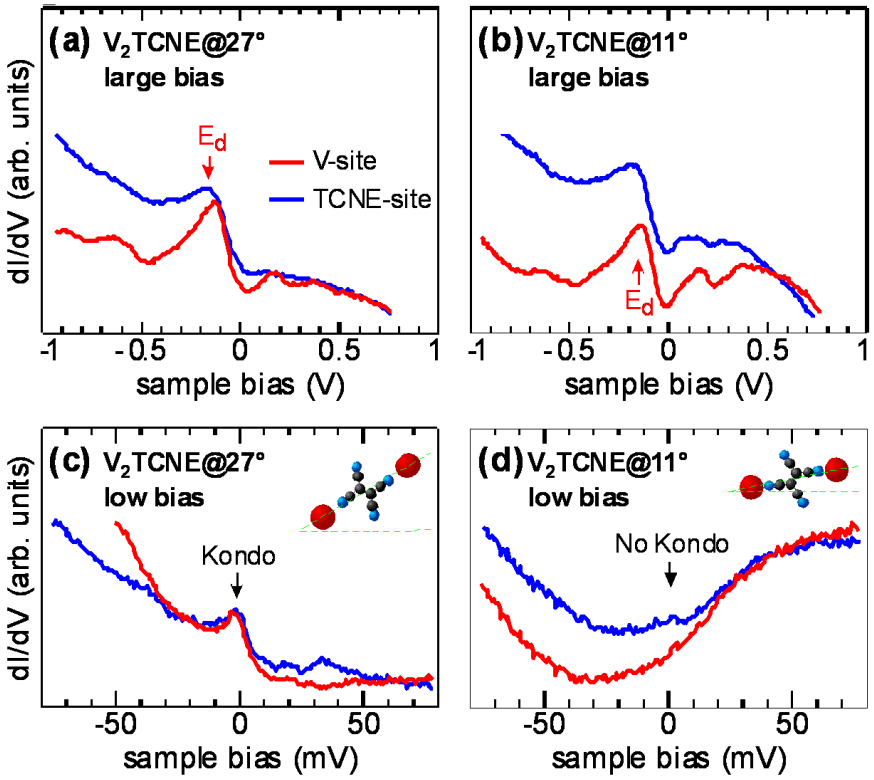

Figure 4.9: High bias dI/dV spectroscopy on (a) V_2(TCNE)@27°, (b) V_2(TCNE)@11°, and low bias spectroscopy on (c) V_2(TCNE)@27°, (d) V_2(TCNE)@11°.

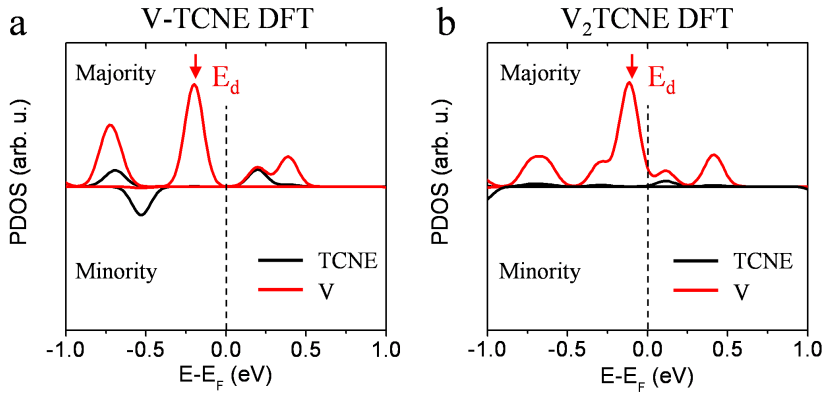

Figure 4.10: SP-DFT calculations of V(TCNE) and V_2(TCNE). The state believed to arise from the V d-orbital is marked with E_d.

presence of a local moment and that these moments are FM coupled for anionic V_2(TCNE).

The reason that the Kondo effect is quenched for V_2(TCNE)@11° and not for V_2(TCNE)@27° is because the 11° complex is more strongly FM coupled through the TCNE molecule than the 27° complex. Although our SP-DFT calculations are not accurate enough to distinguish between these two cases, we can see from the structure of the 11° complex (figure 4.6d) that the V atoms are closer together than for the 27° complex (figure 4.6c). This couples them more strongly to the TCNE ligand, thus providing stronger FM coupling. As this coupling strength rises above the single-moment Kondo temperature, the two V atoms form a FM complex rather than two individually screened magnetic moments. FM coupled spin complexes are well known to have a lower Kondo temperature than single impurities, thus explaining why the Kondo effect is quenched for the 11° complex [88]. The fact that the binding energies of the spin-containing orbital states at E_d, as well as their widths (i.e., their hybridization with the substrate), are identical for both V_2(TCNE)@11° and V_2(TCNE)@27° provides further evidence that quenching of the Kondo effect comes from tunable ligand-induced FM exchange coupling rather than a simple shifting of the single-impurity Kondo temperature.

4.3 V(TCNE) on NaCl

Magnetic nanostructure on conducting surfaces generally has its electronic structure perturbed by the underlying substrate electrons, therefore, it is desirable to have a thin insulating layer decoupling the nanostructure from the substrate. NaCl is an easily grown insulator which was used to accomplish this (§3.2.2). NaCl was thermally evaporated onto a Ag(100) single crystal held at room-temperature, then the sample was cooled to $\sim 40\,\mathrm{K}$ for deposition of TCNE. Figure 4.11a shows topography of TCNE on the second and third layers of NaCl. Spectroscopy shows a LUMO around 1.5 V for TCNE on a second layer NaCl, and 1.8 V for TCNE on a third layer NaCl (figure 4.11)c. We can move TCNE controllably on NaCl.

Unfortunately, after depositing V atoms and manipulating TCNE and V together, we did not see any evidence of spin in V(TCNE) (or it was not detectable under our experimental condition). And we were not able to manipulate V(TCNE) or V to create larger structures.

4.4 Conclusions

This chapter discussed our work of manipulation and characterization of $V_x(TCNE)_y$ magnetic nanostructures on Ag(100) surface. Central to this technique is our discovery that V and TCNE can be induced to form a rigid chemical bond through STM manipulation. The molecular orbital from which V-based spin is derived in the resulting complexes can be directly observed in STS measurements. For complexes consisting of one V atom and either one or two TCNE molecules, this spin is screened by the Ag substrate via the formation of a Kondo resonance. However, for trans-V_2(TCNE), the Kondo effect can be switched on

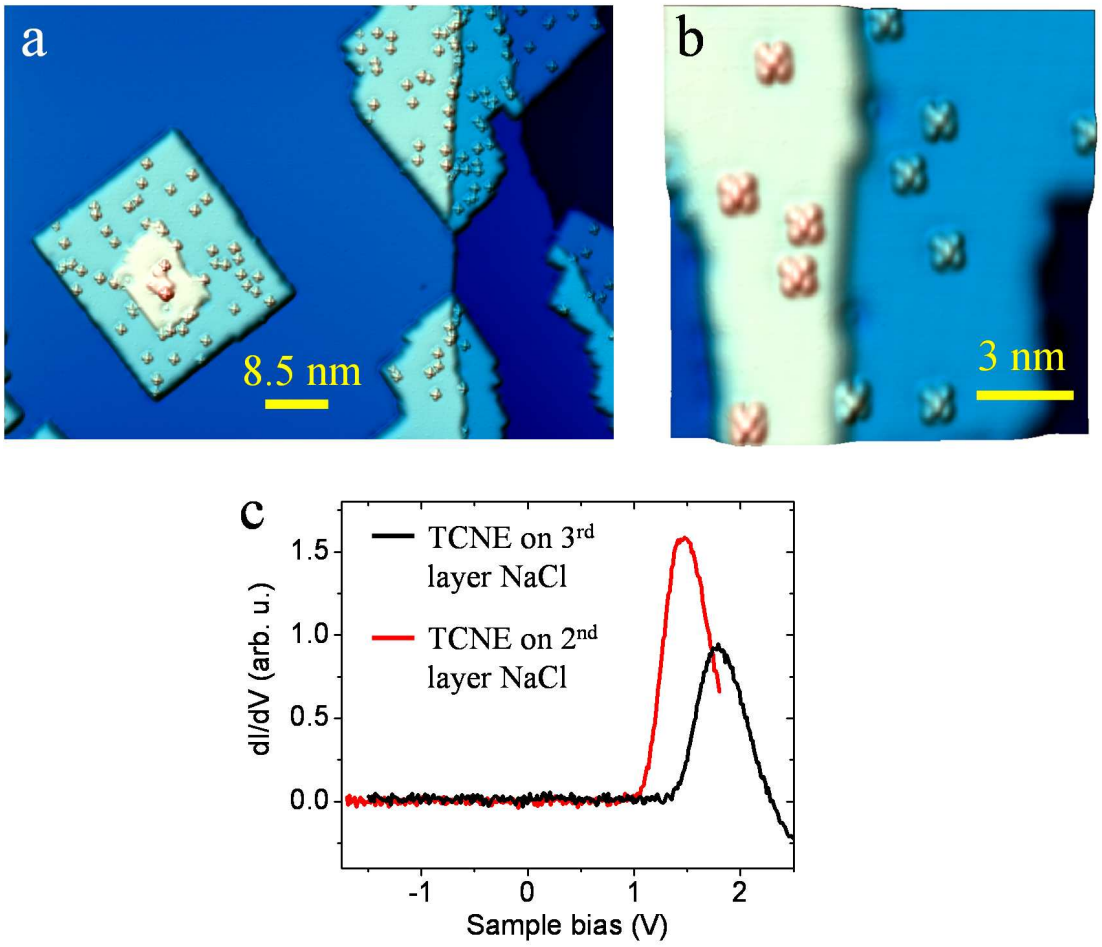

Figure 4.11: Topograph of TCNE on NaCl. (a) Large area showing mainly second layer NaCl islands with isolated TCNE on them ($V = 1.4\,\mathrm{V}$, $I = 1\,\mathrm{pA}$). (b) Zoom-in image on a second layer NaCl island with isolated TCNE molecules. (c) Spectroscopy on TCNE on the second and third layer NaCl islands.

and off by a minute structural change that leaves the spin-containing orbital essentially unchanged. It is explained by the stronger ferromagnetic coupling of the two V atoms through TCNE molecules in the shorter V_2(TCNE).

This direct use of a molecule as a mediating unit between spin centers enables a new type of spin-coupling engineering. For example, the influence of molecular size on magnetic coupling might be studied systematically by replacing TCNE with closely related molecules (e.g., tetracyanoquinodimethane (TCNQ)), or the effects of chemical interactions might be studied by varying functional end groups. Such a bottom-up strategy opens new paths for designing quantum spin structures with atomic-scale precision.

5

TCNE Monolayer Adsorption Site Determination

The precise determination of adsorption sites is critical for understanding many physical phenomena, e.g., heterogeneous catalysis [76, 48], transport in molecular electronics [161], and competing many-body interactions [49]. The STM has proven to be a powerful tool for structure determination of atomic surfaces and small molecules. However, as molecular size and degrees of freedom increase for larger molecules, exact determination of adsorption sites remains a challenge [174]. In most cases, site determinations are only successful for isolated adsorbed molecules, although the necessary simultaneous imaging of the atomic lattice and molecular orbitals is typically very difficult. Even then, great care has to be taken when interpreting atomic-scale contrast in STM images [75, 94, 16]. The use of STM manipulation techniques to compare adsorbate positions with well-known markers has been found to be a successful strategy [123, 21, 104], but this technique cannot be applied to the study of a close-packed molecular monolayer where different molecular arrangements coexist.

As we increase the coverage of TCNE molecules on a Ag(100) surface, they form a densely-packed monolayer. Utilizing density functional theory (DFT) and STS [101], adsorption sites can be analyzed, although not always conclusively. Analysis of STS structure by inelastic effects during electron tunneling allows a deeper understanding of molecular behavior at a surface. Such inelastic electron tunneling spectroscopy (IETS) has become a very successful tool to detect vibrational, photon, and even spin excitations (§2.5). In particular, IETS gives the vibrational fingerprint of adsorbates with extraordinary spatial resolution, thus allowing chemical analysis capabilities at the atomic scale [73].

This chapter will discuss using IETS and DFT to determine the adsorption sites of a TCNE monolayer on Ag(100). We found that while elastic scanning tunneling spectroscopy only shows subtle variations of the local electronic density of states for TCNE at different positions, vibrational modes are very sensitive to the local atomic environment. The high spatial resolution of IETS permits us to map the vibrational signature variation about the surface. Combined with density functional theory, this quantitative information allows for a precise structure determination.

5.1 TCNE Monolayer on Ag(100)

The sample was prepared following the same procedure as in section 4.1, except it was exposed to a higher dose of TCNE vapor, which resulted in TCNE monolayer islands on the Ag(100) surface. After deposition, the sample was transferred *in situ* to the cryogenic STM. Topography images were taken in constant-current mode, and STS and IETS were performed by measuring the differential conductance dI/dV and the 2nd derivative d^2I/dV^2 as a function of the sample bias V by standard lock-in techniques (modulation $1 - 10\,\mathrm{mV}$ (rms), frequency $\approx 451\,\mathrm{Hz}$) under open-feedback conditions.

Figure 5.1 shows STM images of the closed-packed TCNE monolayer on Ag(100). A clear pattern with local regular order can be observed. Molecules arrange in rows along the [110] direction with an intermolecular distance of $8.9 \pm 0.2\,\text{Å}$, i.e., three times the Ag(100) surface lattice constant. Neighboring rows do not form a rectangular arrangement since the molecules are shifted along the [110] direction in order to create a dense packing. Figure 5.1a shows a highly resolved STM image of the monolayer pattern. The molecular shape seen here mainly reflects the lowest unoccupied molecular orbital (LUMO) of neutral TCNE and permits determining molecular orientations [183, 12]. Within each row, all TCNEs orient identically with the C=C double bond being either parallel or perpendicular to the row. From row to row, the molecular orientation always changes by 90°. When the double bond lies along the row direction, the LUMO shape looks slightly distorted with two cyano legs appearing less pronounced than the other two. This is in good agreement with Tersoff-Hamann simulations based on DFT (figure 5.1b) [176].

The apparent height of the monolayer exhibits a significant bias dependence (figure 5.1c, d). For positive sample bias, each molecule is seen as an almost round protrusion with only slight height differences. However, when $V < -0.3\,\mathrm{V}$, molecular shapes are distorted and TCNEs in some rows appear much higher than in others. Overall, we identify three different heights and mark the corresponding rows of TCNE with "A", "B", and "C", respectively. From the highly resolved STM images, we can already make a first connection between the different electronic properties and the structure: B molecules always have the C=C double bonds oriented perpendicular to the row direction, while A and C molecules always have it aligned parallel.

While this local order is observed throughout the entire monolayer, we do not observe long-range order. Rather, the pattern is easily perturbed by local defects or missing molecules. This results in a variation of combinations of A, B and C rows. In regions with more defects, the pattern consists of alternating A and B rows only (cf. figure 5.1a), leading to a chevron pattern with a rectangular $14.4\,\text{Å} \times 8.9\,\text{Å} = (5 \times 3)$ unit cell that contains two TCNEs. In other areas, we observe a larger regular chevron structure with an A-B-C-B-A... sequence, resulting in a (10×3) unit cell with four molecules. The largest chevron pattern observed consists of eight molecular rows, as seen in figure 5.1c. This pattern reveals a fourth row (B') that, however, seems to behave similar to B rows. This patterns spans a unit cell of (20×3) containing eight molecules.

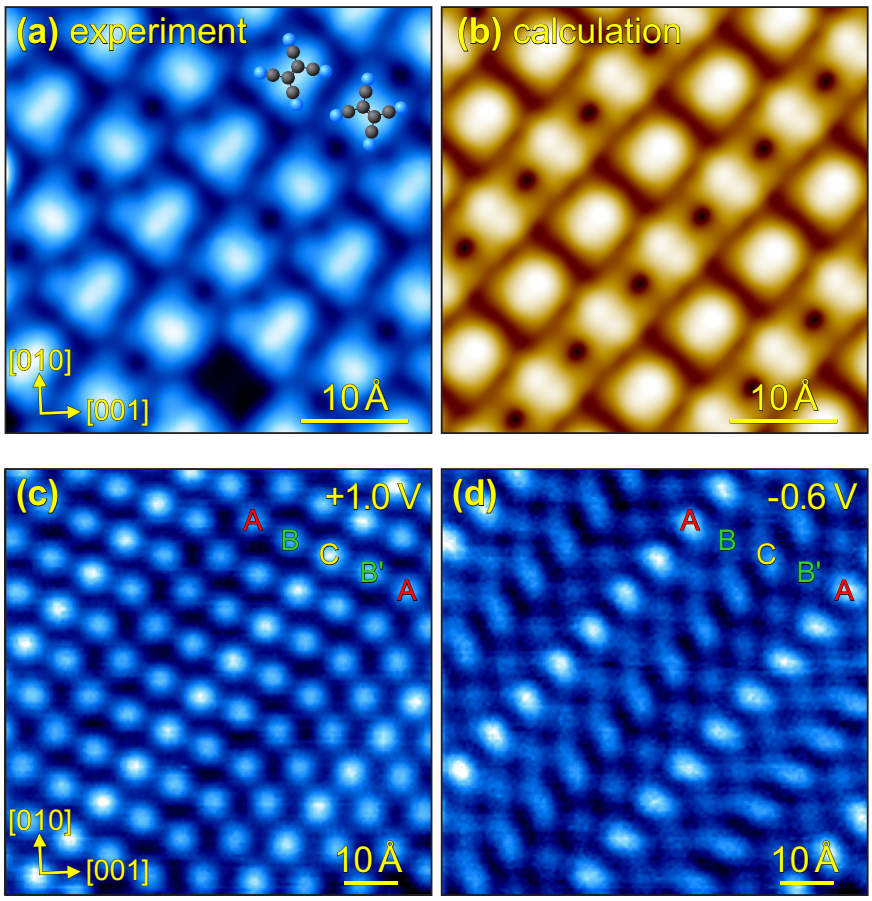

Figure 5.1: Structural analysis of the TCNE monolayer. (a) Highly resolved STM image of the TCNE monolayer on Ag(100). The intramolecular contrast is dominated by the TCNE LUMO, thus revealing molecular orientation. (b) Tersoff-Hamann STM image at 0.1 V derived from the calculated structure (cf. figure 5.3). (c, d) STM images show the same area at +1 V and −0.6 V, respectively. The strong bias-dependent image contrast indicates distinct variations of the LDOS for different adsorption sites.

5.2 STS and IETS of TCNE Monolayer

In order to better understand the molecular LDOS variations, we performed spatially resolved STS measurements on all TCNE molecules within the monolayer pattern. As expected from the topographical analysis, we find that all molecules within a row exhibit identical tunneling spectra. We can therefore summarize all spectroscopic features by showing a representative spectrum for each row (figure 5.2a). Compared to the spectrum on a bare Ag(100) terrace, all TCNE spectra exhibit only minor differences at positive bias (i.e., unoccupied states), while we observe a significant increase in the dI/dV signal at negative sample bias (i.e., occupied states). B and B' rows show identical spectra and exhibit a monotonous increase as we go to larger negative bias. Molecules in C rows show a simi-

lar monotonous LDOS increase, but with a larger slope. The largest slope is observed for TCNE in A rows, and the dI/dV spectrum shows an additional pronounced broad peak at $-0.66\,\mathrm{V}$. This spectroscopic feature is reminiscent of that observed for isolated TCNE on Ag(100), where molecules were found to be adsorbed on top of Ag atoms [183].

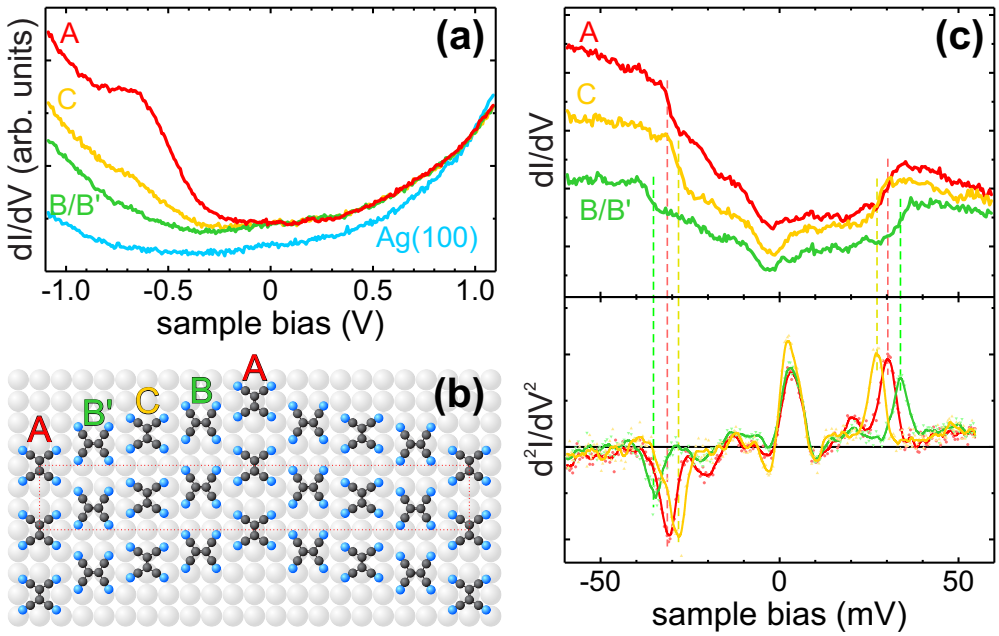

Figure 5.2: STS and IETS data of TCNE molecules at different adsorption sites within the monolayer. (a) Large-bias spectra reveal LDOS differences below the Fermi energy. Spectra for molecules in row A resemble those of isolated TCNE on Ag(100) [183]. (b) A rough structural model of the (20×3) unit cell based only on topography and LDOS analysis suggests A molecules on top of Ag atoms and C molecules on bridge sites, whereas exact adsorption positions of B and B' are not yet clear. (c) Highly resolved dI/dV and d^2I/dV^2 spectra reveal a molecular vibration whose exact energy depends on the adsorption site. For clarity, the Ag-background signal was subtracted from spectra in (c).

The observed structural and electronic features described up to this point allow us to propose a rough structural model (figure 5.2b) where the rows of TCNE molecules form a commensurate structure on the Ag(100) surface with local $(5n \times 3)$ unit cells $(n = 1, 2, 4)$. The spectral resemblance with isolated TCNE suggests that molecules in row A are likely to be adsorbed on top of Ag atoms [183]. Assuming an arrangement of molecules A-B-C-B'-A along a straight line, we find that for C molecules the bridge site is a probable adsorption position with high symmetry. However, B and B' molecules would then lie in a position of very low symmetry. Within our experimental accuracy, we cannot rule out that these molecules relax laterally to a bridge or hollow site, both being only about 0.7 Å away. Therefore, our experimental structure model, as displayed in figure 5.2b, cannot provide precise assignments of adsorption sites in B rows.

The situation changes altogether when we take a look at the vibrational structure of the TCNE molecules by performing STS with high energy resolution (figure 5.2c). Again, we find that all molecules within a specific row exhibit identical spectra. In all cases dI/dV spectra show pronounced step-like features at about $+30$ and -30 meV with a conductance change of $2-3\%$. This is a well-known signature of IETS (figure 5.2c, top) [171]. The energy of this feature is in good agreement with reported values of the in-plane rocking mode as well as the out-of-plane wagging mode of TCNE [125], and it has been observed via STM-IETS for TCNE in various local environments [184, 31]. Upon closer inspection, we find that the exact IETS energy depends on the location of TCNE within the monolayer pattern. This can be seen clearly in the d^2I/dV^2 spectra (figure 5.2c, bottom). Molecules exhibit a mode energy of 30.7 ± 0.5 meV in row A, 34.3 ± 1.0 meV in row B, and 27.7 ± 0.4 meV in row C, (based on a statistical analysis of 32 molecules). Hence, the observed three different mode energies are clearly resolvable and distinguishable. Stiffening or softening of vibrational modes can be caused by local variations of intermolecular or molecule-substrate interactions. Therefore, the observed energies serve as quantitative fingerprints that can help to identify the three different adsorption sites of TCNE and thus lead to a precise structure model of the monolayer on Ag(100).

5.3 DFT Calculations on TCNE Monolayer Vibrational Modes

In order to determine the adsorption sites, we performed DFT simulation of the molecular layer. DFT calculations of vibrational energies of adsorbed molecules on a surface are at best within 10% of the experimental values [18]. Hence, the assignment of modes based on numerical identification is not possible. However, mode frequency shifts are better quantities to examine since they rely on physical trends rather than precise absolute magnitudes. Recent theories based on DFT permit us to simulate the IETS strength at the quantitative level and hence obtain better insight into the experimental data [114, 50]. The combination of energy shifts and IETS simulations has proven to be a good strategy to identify molecular modes and molecular species reliably [18, 135].

Our simulations employed a many-body perturbation extension of the Bardeen tunneling theory [113]. Here we simplify the tunneling description by assuming that the tip electrons are s-waves, as in the Tersoff-Hamann approximation [114]. Our DFT calculations reveal that the different molecular species have different environments. To describe this we will restrict our discussion to the smallest unit cell containing only molecules A and B. This system was modeled by a (5×3) molecular unit cell with 5 Ag substrate layers. The first two substrate layers and molecules have been relaxed until forces on the atoms were less than $0.01\,\mathrm{eV/\AA}$. We used the `vasp` code and the PBE implementation for the exchange and correlation functional [102, 103, 150]. Figure 5.3a, b shows the geometry of this type of TCNE monolayer on Ag(100). A color code has been chosen in (b) in order to emphasize the degree of distortion of Ag atoms in the surface layer due to molecule-substrate interactions. Type

A molecules sit on top of a silver atom with substrate-mediated intermolecular interactions among A molecules since the substrate distortion aligns parallel to the molecular rows of the same species. Type B molecules are on bridge sites and are completely surrounded by high-lying Ag atoms. The molecules are adsorbed via the N–Ag local interactions, and the arrangement provides denser packing.

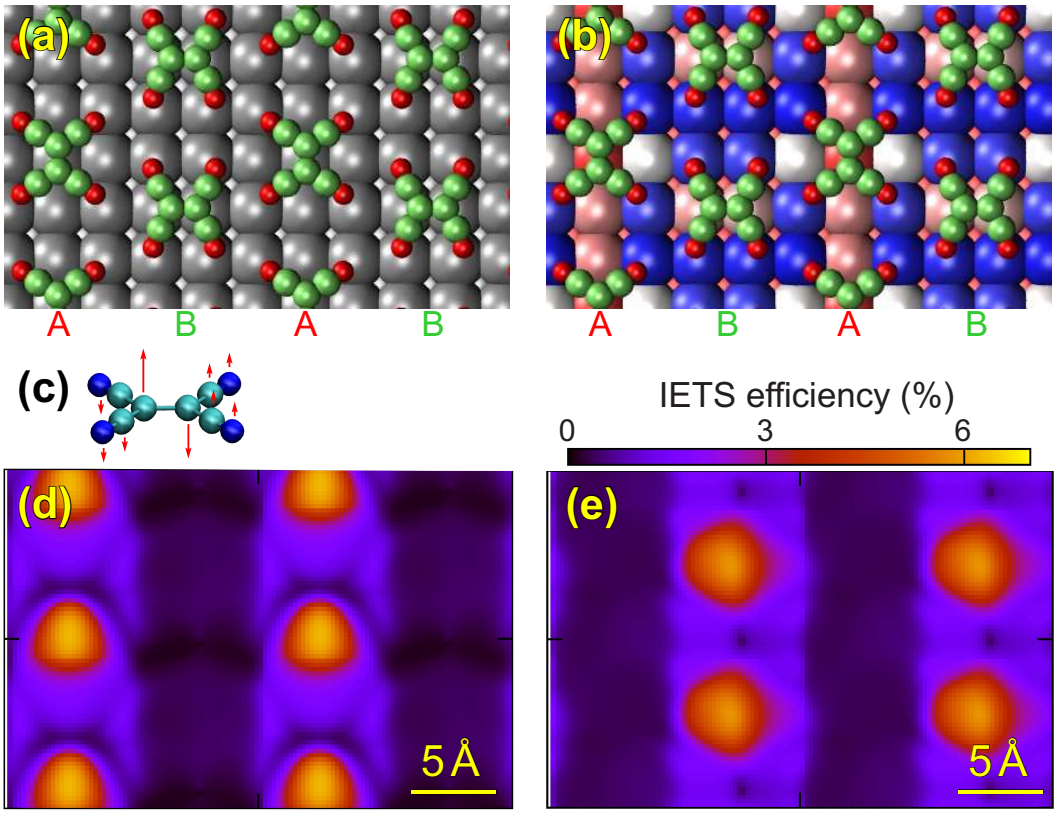

Figure 5.3: DFT calculations and IETS simulations of the (5×3) TCNE monolayer on Ag(100). (a) Atomic scheme of the surface structure showing types A and B molecules in different orientations on top and bridge sites, respectively. (b) Same as in (a) with vertical relaxation of surface atoms color-coded (white: $z = 0\,\text{Å}$, red: $z = -0.4\,\text{Å}$, blue: $z = 0.4\,\text{Å}$). (c) Scheme of the out-of-plane wagging mode that is excited in STM-IETS. (d, e) IETS efficiency in % of tunneling electrons plotted for the out-of-plane wagging mode of type A and B molecules, respectively. The theoretical frequencies of the modes in (d) and (e) are 26.7 meV and 28.8 meV, respectively.

For a closer comparison of theory with the experiments we have simulated the IETS of seven molecular modes located between 23 and 50 meV. Of the two possible modes determined as good candidates for the experimental IETS signal, the simulations only yield one candidate, the out-of-plane wagging mode illustrated in figure 5.3c. This mode appears at two different resonance energies for molecules A and B, respectively. The out-of-plane wagging mode of type A molecules is located at $E_A = 26.7\,\text{meV}$, while that of type B molecules

is found at $E_B = 28.8\,\text{meV}$. The maximum fraction of computed inelastic electrons is 7%, whereas all other modes yield inelastic fractions below 1%. The direction and magnitude of the energy shift $E_B - E_A = 2.1\,\text{meV}$ are in good agreement with the experimentally determined shift of $3.7 \pm 1.2\,\text{meV}$. The frequency shift of the other molecular modes do not always follow this trend. Especially, the second experimentally identified candidate, the in-plane rocking mode, is found at 30.8 meV for molecule A and at 28.3 meV for molecule B in the simulations, i.e., the shift is opposite to the experimentally observed one. The simulations hence show that only the out-of-plane wagging mode is excited in the experiment.

The localization of the inelastic excitations can be shown when plotting the IETS efficiency in a spatially resolved manner. Figure 5.3d shows a map of conductance change with bias when the mode at energy E_A is excited. The IETS simulations clearly reflect the spatial distribution of type A molecules with a maximum IETS signal at the molecular center, in agreement with the experimental findings. When the mode at energy E_B is excited, it is localized to type B molecules, as shown in figure 5.3e.

We now discuss why only the out-of-plane-wagging mode is observed in IETS. In order to have a sizeable IETS signal, two conditions must be met, one regarding the symmetry of vibrational modes and involved electronic states [115] and the other one regarding the degree of influence of the actual mode on the tunneling current [19]. From the analysis of the constant current images we know that the electronic structure about the Fermi energy is dominated by the TCNE LUMO, which is also true in the simulated electronic structure (cf. figure 5.1b). A careful analysis reveals that other levels with weight on the molecular electronic structure lie several eV away from the Fermi energy. Hence, non-zero matrix elements of the electron-vibration coupling basically involve electronic states with large LUMO contributions [115]. Therefore, two LUMO-like levels yield a non-zero matrix element if the mode is symmetric with respect to the system's symmetry elements. Due to the adsorption geometry, the in-plane rocking mode cannot contribute since it is antisymmetric with respect to the mirror plane containing the two central C atoms, while modes like the out-of-plane wagging mode can contribute to the matrix elements. The out-of-plane wagging mode further presents a strong modulation of the N–Ag coupling, since the molecule is moving its N atoms toward and away from the surface. Thus, the out-of-plane wagging mode is qualitatively a strong mode in IETS. Since the out-of-plane wag is the only mode with a strong IETS signal and the correct energy shift, we conclude that type A molecules are adsorbed on top of Ag atoms, and type B molecules are located on bridge sites.

5.4 Conclusions

For TCNE adsorbed onto Ag(100), we have shown that the molecules adsorb onto three nonequivalent positions within the monolayer, as seen in STM images and local STS spectra. While STS only shows subtle differences in the LDOS and cannot help determine specific adsorption sites, we find that vibrational modes, as observed in IETS, give quantitative differences in the mode energy of a particular vibration due to local changes of molecule-

substrate interactions. This inelastic information serves as a reliable input for comparisons with DFT calculations and allows unprecedented accuracy in the structural determination of the TCNE monolayer.

We have demonstrated that IETS can indeed yield accurate information on molecular binding geometries within a defect-free densely-packed molecular monolayer. The high chemical and spatial sensitivity permits detection of small variations that easily lead to meV changes, i.e., well within the typical IETS energy resolution. Such IETS information can potentially be used for other complex molecular systems where topographic methods alone are insufficient to attain reliable structural characterization.

Part III

Photovoltaic Molecules

6 Energy Level Alignment in a Bipolar Molecule

6.1 Introduction to Organic Solar Cells

The fact that we have only finite fossil fuel energy (as well as the issue of carbon buildup in our atmosphere) has evoked much research and industrial interest in developing inexpensive renewable energy sources. Organic photovoltaic cells are based on low-cost organic polymer/molecule materials, and are easily manufactured via vacuum evaporation, solution cast or printing technologies, thus provide a promising alternative technology to harvest and utilize solar energy [137, 4, 106, 172, 60, 152, 197, 64, 80, 58, 153]. Furthermore, organic solar cells offer the flexibility of chemically engineering the energy gap by modifying donor/acceptor components. They also show high absorption coefficients exceeding $10^5\,\mathrm{cm}^{-1}$ [79], so a large amount of light can be absorbed with a small amount of material. Charge carrier mobilities can be as high as $10\,\mathrm{cm}^2/\mathrm{V{\cdot}s}$, making them competitive with amorphous silicon.

The major challenges of organic solar cells include low power conversion efficiency [59], instability of devices, and low strength compared with their inorganic counterparts. More effort is needed to further improve their performance.

6.1.1 Photovoltaic Principles of Organic Solar Cells

In an organic solar cell, two dissimilar materials are brought together. The material with smaller ionization potential and electron affinity serves as a donor, while the other serves as an acceptor. Resulting energy level alignment displays a desired "type-II heterojunction" at the interface [93].

Unlike inorganic solar cells, where free charge carriers are separated by large, well-defined p-n junctions [44], in organic solar cells, photo-generated excitons are separated at microscopic donor-acceptor interfaces. More specifically, the photovoltaic mechanism can be classified into four major steps, as shown in figure 6.1.

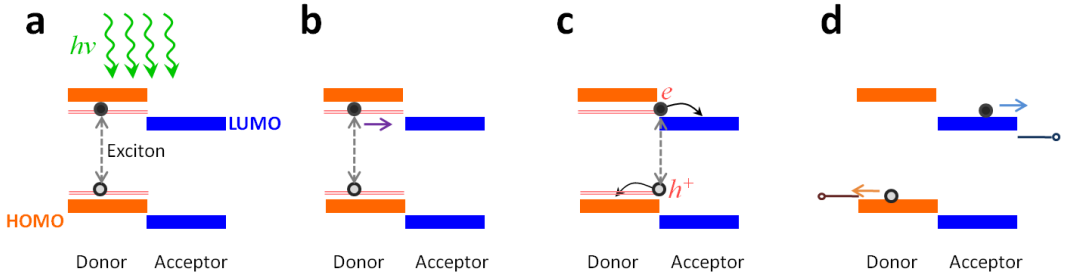

Figure 6.1: Photovoltaic principles of organic solar cells. (a) Exciton creation after light absorption. (b) Exciton diffusion. (c) Exciton dissociation at the interface. (d) Charge transport to respective electrodes.

The photovoltaic process [26] first involves exciton generation due to photon absorption. Due to the relatively large bandgap (more than 2 eV) of typical organic semiconductors, only a small portion (about 30%) of sunlight can be absorbed. The energy of the initially formed exciton can be described by an optical bandgap, E_{opt}, as depicted in figure 6.1a. After the creation of excitons, ideally, they should diffuse to the interface region (figure 6.1b). The exciton diffusion length is usually around 10 nm. At the interface, on the condition that $E_{opt} \geq E_{bg,hj}$, where $E_{bg,hj}$ is the effective heterojunction bandgap, excitons will dissociate (figure 6.1c) [61]. In the last step, free charge carriers are transported to respective electrodes(figure 6.1d).

From this mechanism, we can see the key difference in the organic system is that it is primarily controlled by interfacial processes. It is therefore important to characterize and understand the heterointerface.

6.1.2 Organic Photovoltaic Materials

Based on the principles of organic solar cells, donor and acceptor materials need to have the ability to absorb sunlight and transport charge carriers. Both properties are commonly found in materials with delocalized π electron systems, so they are widely used in organic solar cells. Because of the industrial manufacturing procedures, research is mainly on solution processable polymers/molecules, and thermally evaporated small molecules [78].

Depending on electron affinity and ionization potential, organic semiconductors can be classified into two categories: p-type hole-conducting materials that work as donors, and n-type electron-conducting materials that work as acceptors. Important representative p-type materials include (i) phthalocyanine and derivatives, (ii) derivatives of thiophene, and (iii) derivatives of phenylene vinylene backbones such as poly[2-methoxy-5-(3,7-dimethyloctyloxy)]-1,4-phenylenevinylene) (MDMO–PPV) (as shown in the left column of figure 6.2). For n-type materials, representatives are (i) perylene and derivatives, (ii) C_{60} and soluble derivatives such as PCBM (1-(3-methoxycarbonyl) propyl-1-phenyl[6,6]C_{61}) [189] (right column of figure 6.2).

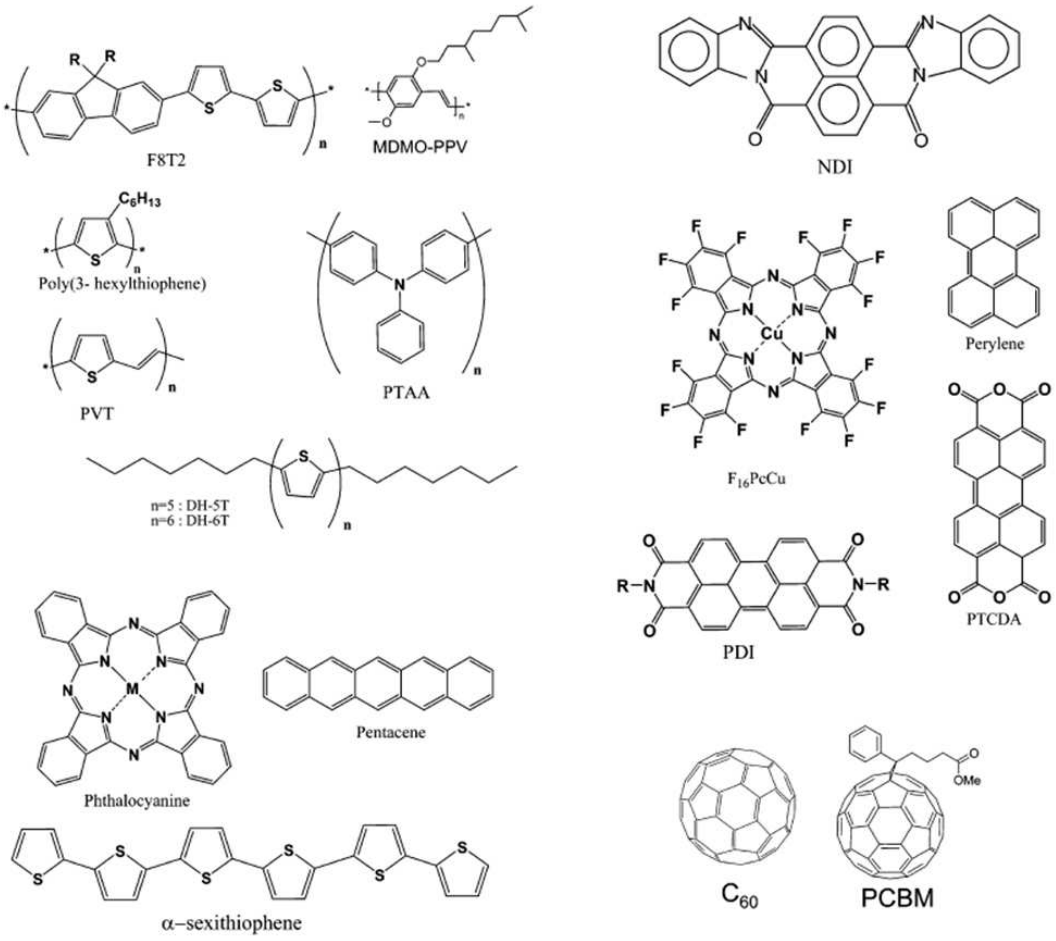

Figure 6.2: Examples of polymers and molecules used in organic solar cells [63]. Left colume: p-type materials. Right column: n-type materials.

6.1.3 Device Architectures

The simplest form of organic photovoltaic cells is the single layer cell, where an organic layer is sandwiched between two electrodes having different work functions (figure 6.3a) [92, 54, 185, 56, 91]. Excitions can be dissociated either by the built-in electric field created by the two electrodes, or the Schottky barrier at the interface of the organics and the metal. However, in practice, the built-in electric field is seldom sufficient to separate the excitons. Also, due to the limited exciton diffusion length (on the order of 10 nm), only excitons in a small region near the contacts can be dissociated [78]. Both factors result in a low efficiency for single layer photovoltaic cells.

Heterojunction solar cells contain two kinds of materials in the active region. In the bilayer setup, donor and acceptor materials are stacked together with a planar interface (figure 6.3b) where the charge separation occurs [172, 151, 163, 154]. The advantage over

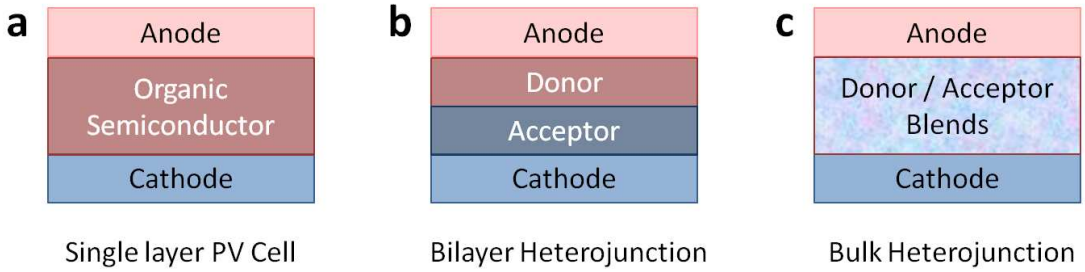

Figure 6.3: Sketches of organic photovoltaic cell morphology. (a) Single layer solar cell. (b) Bilayer heterojunction solar cell. (c) Bulk heterojunction solar cell.

single layer solar cells is in the separation of free charge carriers, i.e., electrons are transported in the acceptor material while holes are transported in the donor material, thus greatly reducing the charge recombination rate. However, the performance of bilayer solar cells is also limited by the exciton diffusion length, only a small fraction of the generated excitons can reach the heterojunction interface.

To address this problem, bulk heterojunction solar cells were invented [197, 64, 198]. The active region in these systems is composed of a mixture of donor and acceptor materials (schematically shown in figure 6.3c), so that each donor-acceptor interface is within the distance of the exciton diffusion length. Ideally, all excitons can be dissociated within their lifetime. Charges are separated in different materials, and hence recombination is reduced to a large extent. In order for charge carriers to reach their respective electrodes, donor and acceptor materials have to form a bicontinuous and interpenetrating network. Therefore, the performance of bulk heterojunction solar cells largely depends on the nanoscale morphology of the blend.

6.2 Bipolar Molecules

As mentioned in the previous section, the donor/acceptor interface is particularly important for the photovoltaic process. However, due to the spatially confined interface region and the morphology of photovoltaic cells, it is hard to characterize the interface. For the study of nanoscale electronic properties, STM is a particularly suitable tool. Previous STM work on donor/acceptor blends, however, has suffered from strong coupling to a metal substrate [57], or poorly resolved interfaces [83].

Bipolar molecules that incorporate donor and acceptor components within a single molecule address this issue. By characterizing the internal electronic structure of a single bipolar molecular heterojunction, we are able to study subnanometer features of the intramolecular donor-acceptor interface. Such molecules also create exciting device opportunities such as for diodes, LEDs, and photovoltaic devices [39, 164]. For many of these PV applications, it is important for bipolar molecules to have "type-II heterojunction" (§6.1.1).

The flexibility of chemical engineering molecules can enable such energy level alignment.

The bipolar molecules used in our experiment were bithiophene naphthalene diimide (BND) molecules. They internally incorporate both donor (thiophene) and acceptor (naphthalene) regions (figure 6.4). When placed on an epitaxial NaCl film, these molecules exhibit staggered orbital energy level shifts and orbital localization over interface distances down to the length scale of a single covalent bond, with the highest occupied molecular orbital (HOMO) and lowest unoccupied molecular orbital (LUMO) on the thiophene and napthalene sides, respectively. The measured energy gap is around 1.7 eV.

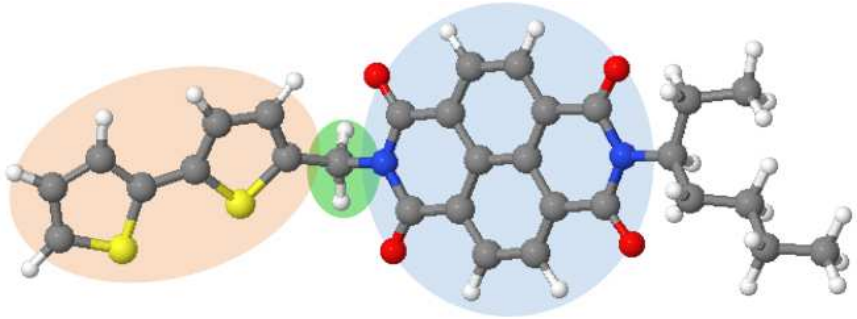

Figure 6.4: Structure of bithiophene naphthalene diimide (BND) molecule. Red shade is the donor part (bithiophene) and blue shade is the acceptor part (naphthalene diimide). They are connected by a bridge –CH_2–, and are protected by a tail –$CH(C_2H_5)$–C_4H_9.

6.3 BND Molecules on NaCl/Ag(100)

Previous STM study has shown that the electronic structure of donor/acceptor interface is strongly influenced by a metal substrate [57]. To study the intrinsic properties of BND molecules, we decoupled them from a metal substrate with a thin layer of NaCl (§3.2.2). The Ag(100) single crystal substrate used in this experiment was cleaned by standard sputter/annealing procedures. NaCl was then thermally evaporated onto the Ag(100) held at room temperature. After cooling the sample to $T \sim 30 - 40\,\mathrm{K}$, we deposited BND molecules from a Knudsen cell evaporator onto the cold substrate. The cooling procedure immobilized and isolated molecules. The sample was then transferred *in situ* to the cryogenic STM.

Figure 6.5 shows an STM image of isolated BND molecules resting on an epitaxial NaCl bilayer near a patch of bare Ag(100) surface. The coverage of BND molecules was kept low in our experiment so that the molecules could be characterized in the single molecule regime. The typical footprint of a BND molecule is $\sim 20\,\text{Å} \times 30\,\text{Å}$ for $V = 1.0\,\mathrm{V}$ and $I = 1.0\,\mathrm{pA}$ (the elongated direction of the molecule is marked by a black dashed line in figure 6.5). This shape is consistent with the expected size of BND molecules. We observe a significant fraction (70%) of BND-derived adsorbates on NaCl to have shapes with a markedly different footprint than the elongated BND species shown in figure 6.5 (they are either significantly smaller, "round", or bent). We assume that these other morphologies

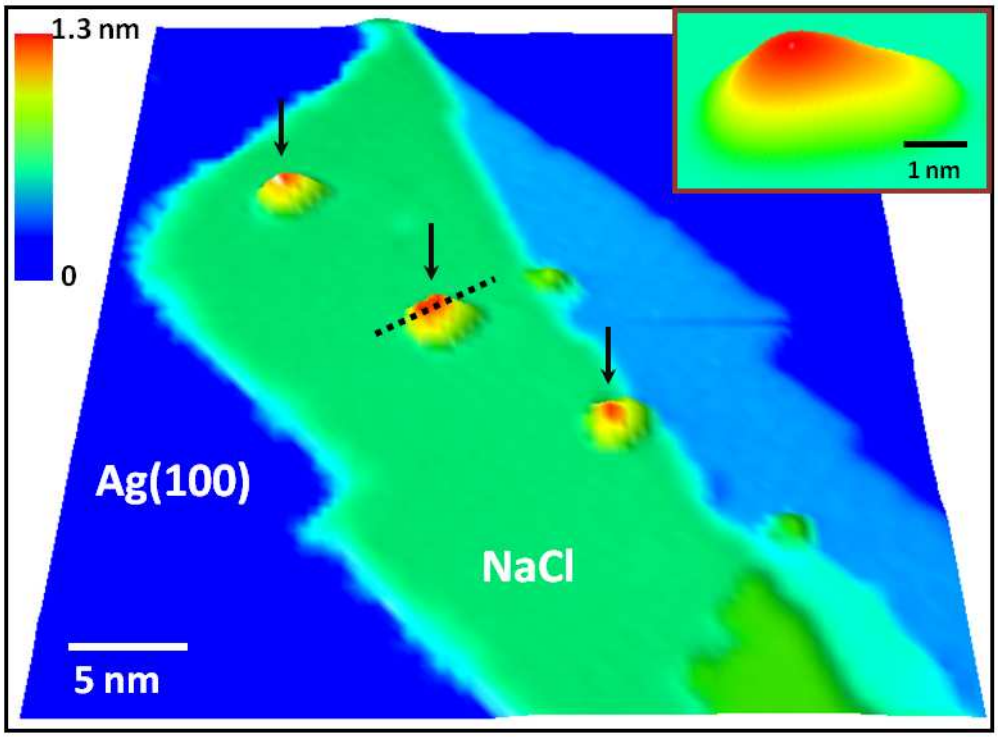

Figure 6.5: Constant current topograph of BND molecules on a NaCl island obtained at $T = 7\,\mathrm{K}$ ($V = 1\,\mathrm{V}$, $I = 1\,\mathrm{pA}$). The light green and light blue regions are NaCl bilayer terraces while the dark blue area is the bare Ag(100) surface (black arrows point at BND molecules, the black dashed line indicates the elongated direction of a bipolar BND molecule). Inset: zoom-in image of a BND molecule.

are either broken BND fragments or BND molecules in different conformational states. In order to check that the elongated species shown in figure 6.5 is not a fragment or cluster, we separately deposited bithiophenes and naphthalene diimide monomers onto NaCl bilayers under similar conditions. Neither class of monomer yielded molecular morphologies similar to the elongated species shown in figure 6.5.

We examined the local electronic structure of the elongated molecular species using STM spectroscopy. dI/dV spectra were recorded sequentially while holding the STM tip stationary at 2 Å intervals along the centerline above the molecule (see dashed line in figure 6.5). We have observed three kinds of behaviors, (i) bipolar behavior indicative of a single-molecule type II heterojunction in 30% of the elongated molecules (shown in figure 6.6), (ii) a spatially uniform (delocalized) HOMO-LUMO gap across the whole molecule in 40% of elongated molecules (figure 6.7a), and (iii) a LUMO level with no corresponding HOMO level on one side of the molecule while HOMO and LUMO states appear on the other side within our $\pm 1.5\,\mathrm{V}$ windows (seen in 30% of elongated molecules) (figure 6.7b).

The spectra for molecule species (i) exhibit four states: (1) a HOMO-1 state at $-1.11 \pm 0.04\,\mathrm{V}$, (2) a HOMO state at $-0.78 \pm 0.12\,\mathrm{V}$, (3) a LUMO state at $0.92 \pm 0.09\,\mathrm{V}$, and

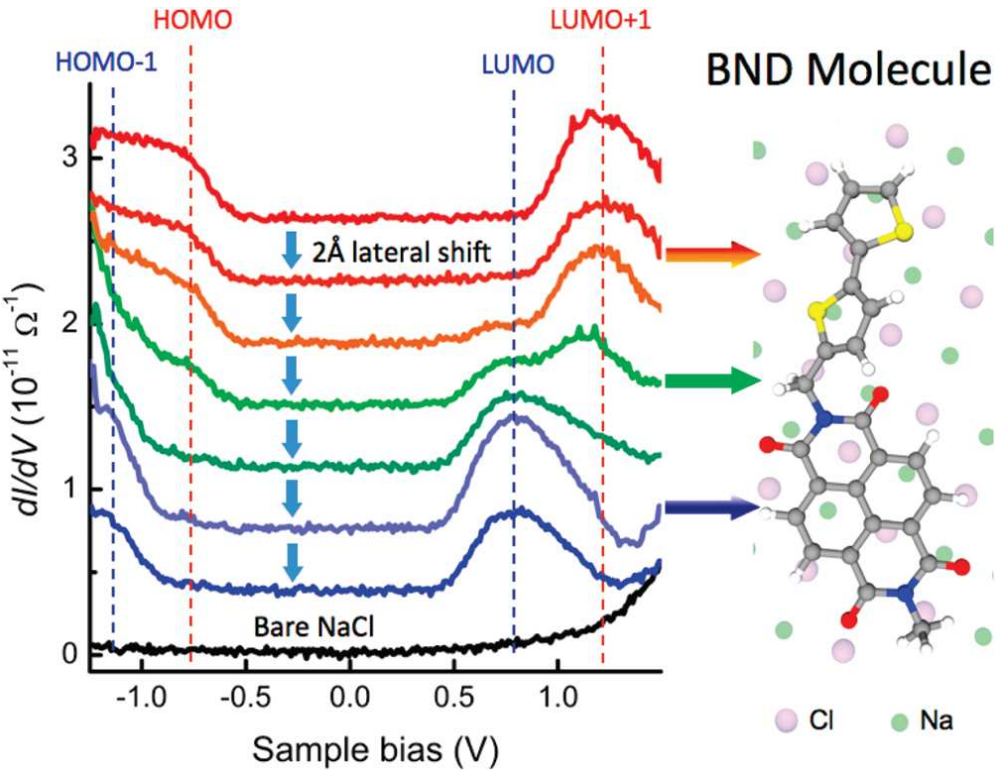

Figure 6.6: dI/dV spectroscopy of a bipolar BND molecule on NaCl at $T = 7\,\mathrm{K}$. The dI/dV spectra were taken with the STM tip held over different spots along the elongated axis of a single molecule at 2 Å increments. Large arrows indicate where on the molecule (sketch at right) different spectra were obtained as the tip was moved from the bithiophene region (red curves) to the bridge region (green curves) and then to the naphthalene region (blue curves). The bottom (black) curve is the dI/dV spectrum of the bare NaCl bilayer. Molecular sketch shows "flattened" BND conformation on NaCl from calculations.

(4) a LUMO+1 state at $1.30 \pm 0.10\,\mathrm{V}$ (these energies were determined by fitting all four states to Lorentzian peaks, including additional data not shown in figure 6.6, and the error represents the standard deviation of fitted peak center points). The HOMO-LUMO gap is seen to be $1.70 \pm 0.15\,\mathrm{V}$. Perhaps the most striking feature of the data is the intramolecular spatial localization observed for these four states. HOMO and LUMO levels are observed to strongly localize on opposite sides of a single BND molecule. LUMO+1 and HOMO-1 levels are observed to localize on the same sides as the HOMO and LUMO states, respectively. An interface region is seen between the two sides of the molecule that shows all four states coexisting over a narrow width of 4 ± 1 Å, which is about twice a covalent bond length. dI/dV spectra do not change significantly on either side of the molecule until this interface region is entered.

Spatial localization of the molecular orbitals for a single bipolar BND molecule can be seen more directly in the images of figure 6.8. Figure 6.8a and c show dI/dV maps for

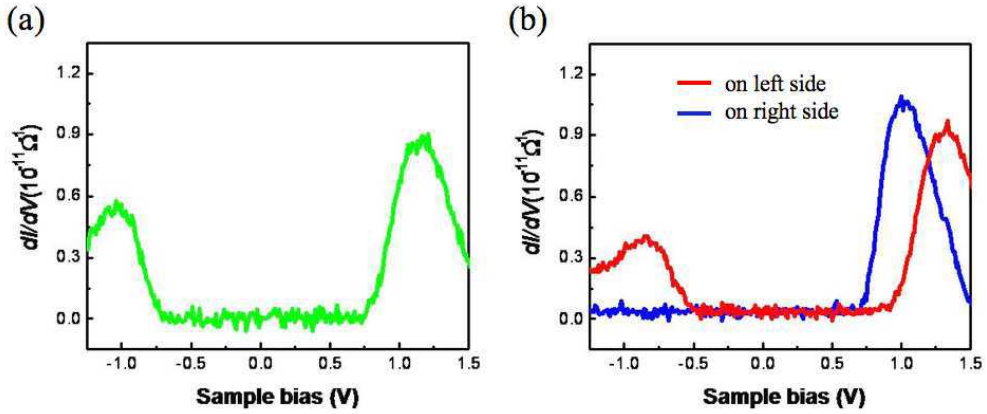

Figure 6.7: (a) Spectroscopy of molecules having behavior (ii) shows a spatially uniform HOMO-LUMO gap across the whole molecule. (b) Spectroscopy of molecules having behavior (iii) show a LUMO level on one side of the molecule with no corresponding HOMO level in $\pm 1.5\,\mathrm{V}$ window, while HOMO/LUMO states can be seen on the other side of the molecule.

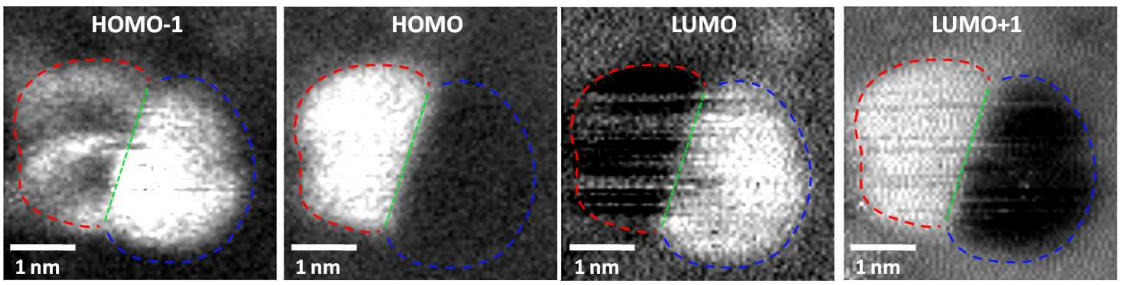

Figure 6.8: Energy-resolved dI/dV maps of the local density of states of a single bipolar BND molecule. (a) and (c), dI/dV maps taken at $V = -1.1\,\mathrm{V}$ and $V = 1.1\,\mathrm{V}$, revealing localization of HOMO-1 and LUMO orbitals onto right side of molecule(dashed blue line outlines naphthalene region). (b) and (d), dI/dV maps taken at $V = -0.6\,\mathrm{V}$ and $V = 1.3\,\mathrm{V}$, revealing localization of HOMO and LUMO+1 orbitals onto left side of molecule (dashed red line outlines bithiophene region).

a single BND molecule obtained at sample voltage of -1.1 and $1.1\,\mathrm{V}$. Spatial localization of the HOMO-1 and LUMO level can be clearly seen on the right side of the molecule (outlined in blue). Figure 6.8b and d show dI/dV maps of the same molecule taken at a sample voltage of -0.6 and $1.3\,\mathrm{V}$. Spatial localization of the HOMO and LUMO+1 level can be clearly seen on the left side of the molecule (outlined in red) with a relatively sharp interface region.

6.4 DFT Calculations on BND Molecule

In order to identify the origin of type II heterojunction behavior in single BND molecules, to correlate BND electronic behavior with molecular geometry, and to better understand the role of substrate screening on the BND electronic structure, We theoretically studied different conformational states of the BND molecule both in gas phase and on a NaCl substrate within the density-functional theory (DFT)/local density approximation (LDA) framework using the SIESTA code [136, 168]. On NaCl we observe stable configurations where the naphthalene plane of the molecule is adsorbed flat on the NaCl, while the bithiophene plane can either stick out from the surface (an "orthogonal" conformation) or lie flat on the NaCl (a "flattened" conformation). The BND molecular orbitals hybridize very weakly with the NaCl states, except for one notable exception. When the oxygen atoms in the naphthalene align with the sodium atoms in NaCl, then the HOMO-1 orbital of the BND molecule strongly hybridizes with the valence band states of NaCl. This chemisorbed state explains the absence of an apparent HOMO level for experimental case (iii) discussed above, while experimental case (ii) can be explained by the orthogonal conformations of BND molecules where we believe that the experimental spectra are dominated by the HOMO and LUMO+1 states of the extracted bithiophene plane. Desirable type II heterojunction behavior (experimental case i) can be explained by the flattened physisorbed case, sketched in figure 6.6.

We modeled our single-molecule spectroscopy results by computing the quasi-particle energy spectrum of an isolated BND molecule in the flattened conformation from first principles and by treating the influence of dielectric and metallic components of the substrate within an image charge framework. We first calculated the BND electronic ground state with DFT [97] employing norm-conserving pseudo-potentials, a plane-wave basis set and LDA for the exchange-correlation potential [97, 148, 177, 96]. Excited-state quasi-particle energies were obtained by solving the Dyson equation within the GW approximation for the electron self-energy operator [81, 68]. Here the self-energy is expressed in terms of the one-particle Greens function, G, constructed using the Kohn-Sham orbitals, and the intramolecular screened Coulomb interaction, W, calculated within the random-phase approximation. Substrate screening-induced renormalizations of the quasi-particle energies of an adsorbed BND molecule were modeled via an image charge model [130]. The position of the image plane was determined separately from a DFT calculation of the screening of an applied uniform electric field at a NaCl bilayer on Ag(100) [105].

Figure 6.9 shows a graphical representation of the calculated quasi-particle states. Here the horizontal axis is electron energy with respect to the vacuum level, the vertical axis represents lateral position along a single bipolar ("flattened") BND molecule, and the plot intensity is proportional to the quasi-particle local density of states (LDOS) (red for states on the donor side and blue for states on the acceptor side with an energy broadening of 0.1 eV). Two sketches of a BND molecule are included in the figure, one showing the spatial distribution of the calculated HOMO orbital and the other showing the LUMO orbital (the alkene tail on the naphthalene side of the synthesized BND molecule is not included in the

GW calculation since the presence of the tail does not significantly affect the molecular electronic structure). The calculated HOMO orbital is seen to strongly localize on the thiophene (donor) side of the molecule, while the LUMO orbital strongly localizes to the naphthalene (acceptor) side of the molecule. The LUMO+1 and HOMO-1 orbitals are also localized to the thiophene and naphthalene sides, respectively, and an interface region having a width of a few angstroms can be seen near the central C–N bond where all four orbitals overlap spatially. The HOMO-LUMO gap calculated here is 2.3 eV and the HOMO/HOMO-1 and LUMO/LUMO+1 energy differences are 1.2 and 1.8 eV, respectively. This leads to a calculated type II heterojunction behavior that is qualitatively very similar to what is seen experimentally for a single BND molecule (figures 6.6 and 6.8), providing further evidence that the experimental data reflect true bipolar behavior for a single, integrated donor-acceptor molecule.

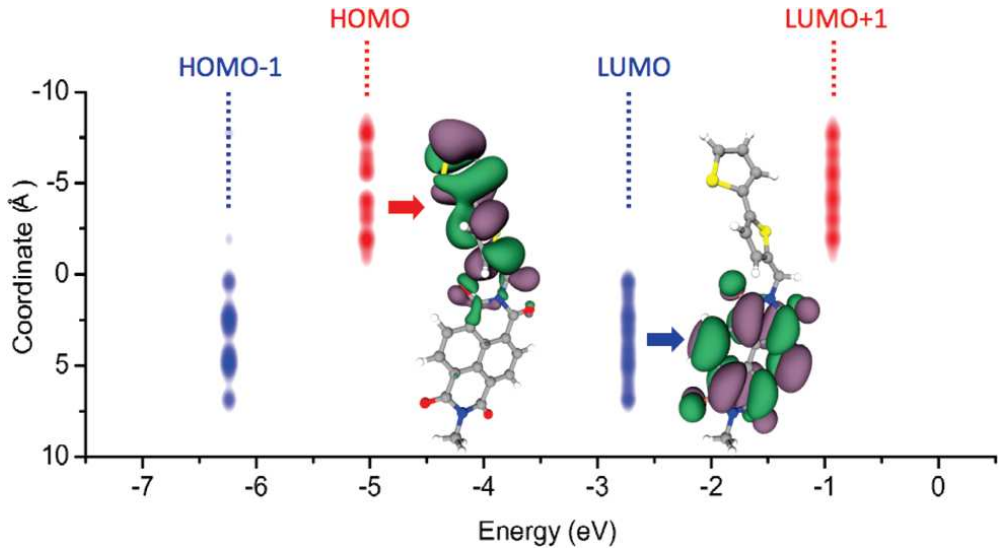

Figure 6.9: Quasi-particle local density of states (LDOS) of the bipolar BND molecule (flattened conformation) calculated within the GW approximation as a function of lengthwise coordinate along the molecule and of energy. HOMO-1 and LUMO (blue) are localized on the naphthalene (acceptor) side of the molecule while HOMO and LUMO+1 levels (red) are localized on the bithiophene (donor) side. The LDOS has been broadened by 0.1 eV in energy. The isosurfaces of the HOMO and LUMO wave functions are superimposed on properly scaled sketches of the molecule (green and purple colors correspond to opposite signs of the wave function phase).

A discrepancy does exist between the magnitude of the theoretical HOMO-LUMO gap and nearby energy levels as compared to the experimental levels. There are many factors at play here [130]. We find that when the DFT Kohn-Sham eigenvalues are used, then the calculated LDA HOMO-LUMO gap of an isolated BND molecule is only 0.7 eV, much smaller than the experimental value of 1.7 eV. The GW self-energy correction using the LDA Kohn-Sham orbitals for G opens the HOMO-LUMO gap to 4.0 eV. When screening from the

substrate is modeled by an image charge model [130], the theoretical quasi-particle HOMO-LUMO gap drops down to 2.3 eV, a value much closer to our experimental result. Some of the factors that likely play a role in the remaining discrepancy between experimental and theoretical gap values are the following: (i) use of LDA Kohn-Sham orbitals can introduce error to the calculated quasi-particle energies [24], (ii) use of the generalized plasmon-pole model for the frequency dependence of the inverse dielectric matrix is known to work very well for solids [81] but has not been extensively tested for molecules, and (iii) use of the simple image charge model may not capture all of the effects of interaction with the substrate.

There is much that we learn through comparison of our experimental and theoretical results. First, the simulated LDOS map of figure 6.9 helps us to identify the experimental localized HOMO and LUMO regions as thiophene (donor) and naphthalene (acceptor) regions of the BND molecule, respectively. The calculations additionally suggest that the large fraction of BND molecules not showing precise type II heterojunction behavior likely arise from different surface conformations of BND. The importance of substrate screening is also highlighted as a significant factor in the reduced HOMO-LUMO gap (such substrate-induced HOMO-LUMO gap screening has been observed in different molecular systems [130, 160, 180]). This effect could potentially be used as a means of tuning molecular band gaps to control the behavior of devices incorporating bipolar molecular elements. We also note that the power conversion efficiency of photovoltaic molecular devices depends on LUMO/LUMO+1 energy level differences relative to excitonic binding energies, as well as HOMO-LUMO spatial overlap at the donor/acceptor interface [61]. By tuning molecular bridge structure, we expect to gain a higher degree of control over such properties [122, 2].

6.5 Conclusions

We have studied the electronic properties of single BND molecules on NaCl/Ag(100) using STM and DFT. By performing STS with angstrom-level resolution, we find that individual BND molecules exhibit staggered orbital energy level shifts and orbital localization over interface distances down to the length scale of a single covalent bond. HOMO and LUMO+1 states are localized to the bithiophene side, while HOMO-1 and LUMO levels are localized to the naphthalene side, leading to an overall type II heterojunction level alignment. This single-molecule type II heterojunction behavior is consistent with *ab initio* theoretical modeling that predicts similar behavior in the electronic spectrum of an isolated BND molecule. Comparison between our experimental and theoretical results reveals a strong renormalization of the BND HOMO-LUMO gap due to the surface environment and suggests new strategies for enhancing the device performance of this class of molecules.

7

Self-Assembly of Bipolar Molecules on Au(111)

The previous chapter focused on the electronic properties of isolated bipolar BND molecules. However, for device applications it is desirable to learn the collective behavior of large assemblies of these molecules. For example, if the molecules self-assemble into ordered domains, charge carrier mobilities might be greatly enhanced [66]. Or if the molecules form inter-penetrating networks, the small exciton diffusion length might facilitate the exciton dissociation process [131, 33]. This chapter presents our work on studying the behavior of self-assembled BND molecules on a Au(111) surface.

The molecules we investigated are a modified version of the previous BND molecule (§6.2). Instead of a -CH_2- bridge, the donor (bithiophene) and the acceptor (naphthalene diimide) are directly connected (a schematic model is shown in figure 7.1). This molecule has fewer configurations on surfaces, and thus is more suitable for self-assembly studies.

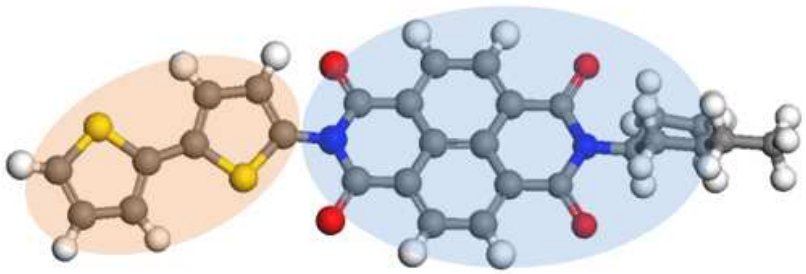

Figure 7.1: Structure of the directly bonded bithiophene naphthalene diimide molecules. Red shade is the donor part (bithiophene) and blue shade is the acceptor part (naphthalene diimide), they are connected by a C–N bond.

7.1 Molecules on Au(111) Terraces

We have studied the self-assembly properties of these molecules on Au(111). The Au(111) substrate was cleaned by standard sputter-annealing procedures and then exposed at $T = 300\,\mathrm{K}$ to the direct BND molecules that were thermally evaporated from a Knudsen cell evaporator. The sample was then transferred *in situ* to the cryogenic STM for measurement.

Figure 7.2 shows STM topographs of the molecules on Au(111) terraces. Isolated molecules are seen on the elbow sites of the Au(111) herringbone reconstructed surface [187, 11]. They appear as oval protrusions with typical size of $\sim 20\,\text{Å} \times 30\,\text{Å}$ for positive sample bias, with one side appears higher than the other side (figure 7.2a). In the fcc region of the herringbone, the molecules aggregate into chain structures (figure 7.2b). Comparing these images with the single molecule morphology indicates that the molecules within the chain are anti-parallel with each other. A schematic drawing of the chain formation is shown in figure 7.2d.

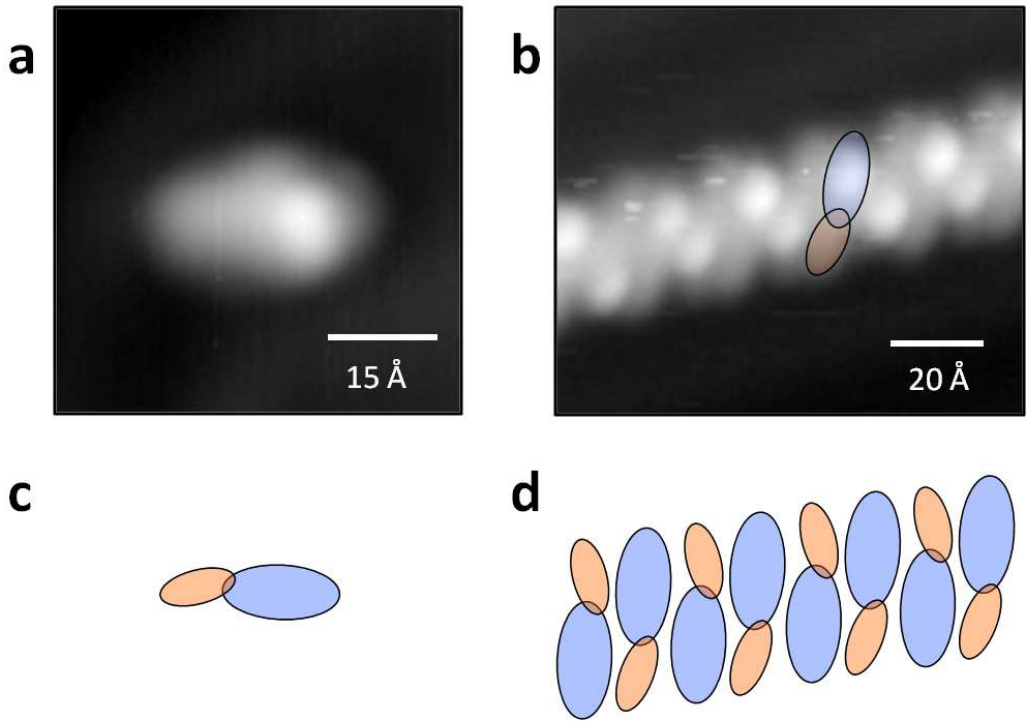

Figure 7.2: Topographs of direct BND molecules on Au(111) terraces. (a) A single molecule near the elbow site of Au(111) reconstructed surface ($V = 1.1\,\mathrm{V}$, $I = 1.0\,\mathrm{pA}$). (b) A molecular chain in the fcc region ($V = 1.0\,\mathrm{V}$, $I = 2.0\,\mathrm{pA}$). (c) Schematic drawing of an isolated molecule. (d) Schematic drawing of a molecular chain.

The formation of anti-parallel chain structure can be explained by the bipolar nature of the molecule. Because of the difference in the electron affinity and ionization potential, the bithiophene side is more positive while the naphthalene diimide side is more negative.

The electrostatic interaction results in an anti-parallel chain in order to minimize electric potential energy.

7.2 Molecules near Step-edges

Near step-edges, however, direct BND molecules self-assemble in a much different way. Figure 7.3a shows a large-scale topograph image where a lot of step-edges are visible, the step-edges are decorated by molecules. A zoom-in image shows that those molecules form parallel chains (figure 7.3b).

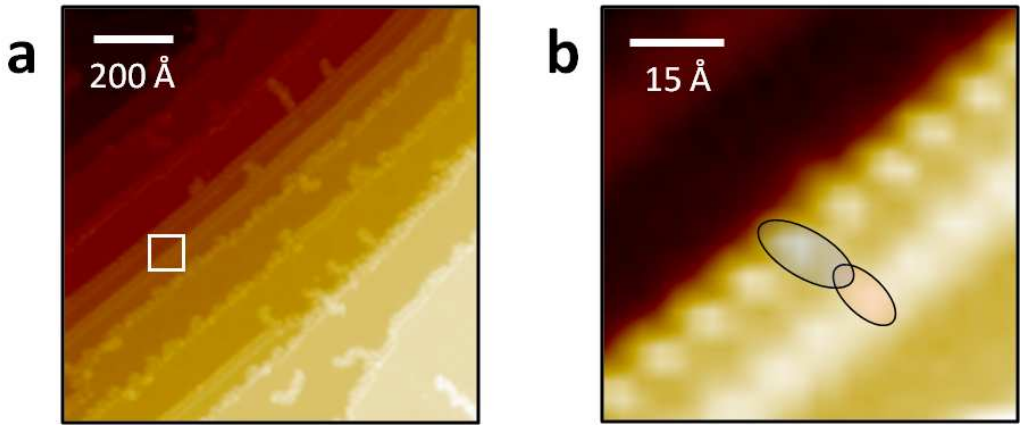

Figure 7.3: Topographs of direct BND molecules on Au(111) step-edges. (a) Large-scale image shows molecules aggregate at step-edges ($V = 1.5\,\mathrm{V}$, $I = 2\,\mathrm{pA}$). (b) Zoom-in image shows the molecules form parallel chains ($V = 1.5\,\mathrm{V}$, $I = 2\,\mathrm{pA}$).

This different assembly behavior can be explained by the Smoluchowski effect [166]. To minimize the surface energy, the electrons near step-edges, instead of taking the original step-like distribution, are smoothed out, resulting in positive net charge on the upper terrace, and negative net charge on the lower terrace, as schematically shown in figure 7.4a. Note that the bithiophene part is more positive, direct BND molecules tend to align along the step-edge on the lower terrace (figure 7.4b).

7.3 Conclusions

This chapter presents our preliminary work on the self-assembly behavior of bipolar molecules. By depositing directly connected BND molecules on Au(111) substrate, we found that these molecules tend to self-assemble into anti-parallel chains on terraces. Near step edges, due to the Smoluchowski effect, they form parallel chains. These results indicate that in order for these molecules have device applications, a careful design of the environment is needed.

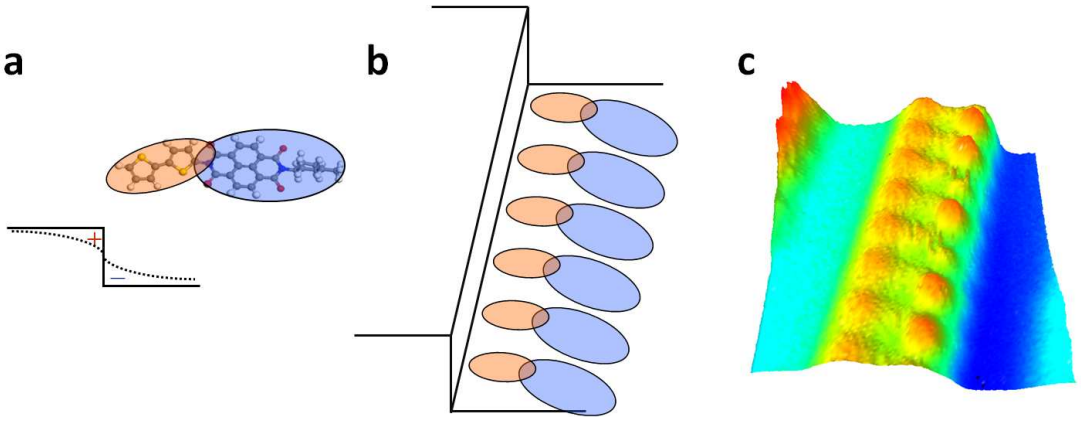

Figure 7.4: Schematic and STM images of parallel molecular chains.(a) Schematic drawing of charge distribution near step-edges. (b) Schematic drawing of a parallel chain near a step edge. (c) STM image of a parallel molecular chain along a step edge ($V = 1.5\,\mathrm{V}$, $I = 2\,\mathrm{pA}$).

The STM instrument (§3.1) used in these studies has the limitation that there is no optical access, thus we have only studied electronic properties so far. In the future, we would like to directly study local optical and transport properties of molecular devices and test how these properties vary with atomic and molecular structure.

Part IV

Graphene Nanoribbons

8

Edge States of Chiral Graphene Nanoribbons

A central question in the field of graphene-related research is how graphene behaves when it is patterned at the nanometer scale with different edge geometries. A fundamental shape relevant to this question is the graphene nanoribbon (GNR), a narrow strip of graphene that can have different chirality depending on the angle at which it is cut. Such GNRs have been predicted to exhibit a wide range of behaviour, including tunable energy gaps [169, 43], and the presence of one-dimensional (1D) edge states [129, 1, 186] with unusual magnetic structure [51, 170]. Most GNRs measured up to now have been characterized by means of their electrical conductivity, leaving the relationship between electronic structure and local atomic geometry unclear [30, 65, 110].

The STM provides the unique capability to study the local structural and electronic information with sub-angstrom precision, and thus is particularly suitable for studying how GNR electronic structure depends on the chirality of atomically well-defined GNR edges. Our STS measurements reveal the presence of 1D GNR edge states, the behaviour of which matches theoretical expectations for GNRs of similar width and chirality, including width-dependent energy splitting of the GNR edge state. This chapter is based on a published paper, reference [173].

8.1 Graphene Nanoribbons on Au(111)

The GNRs used in this work were chemically synthesized using carbon nanotube (CNT) unzipping methods [100, 90] by our collaborators at Stanford University [90]. GNRs were deposited onto clean Au(111) surfaces using a spin-coating method (§3.3.5). Au(111) substrates were first cleaned by sputtering and annealing in ultra-high vacuum (UHV) before spin-coating. The samples were then transferred into the UHV chamber of our STM system (base pressure $\sim 2 \times 10^{-10}$ torr). After heat treatment up to 500 °C in UHV, the samples were transferred *in situ* onto the STM stage for measurements. STM topography was obtained in constant-current mode using a PtIr tip, and dI/dV spectra were measured using

lock-in detection of the a.c. tunneling current driven by a $\sim 451\,\mathrm{Hz}$, $1-5\,\mathrm{mV}$ (r.m.s.) signal added to the junction bias (the sample potential referenced to the tip) under open-loop conditions.

Figure 8.1a shows a room temperature image of a single monolayer GNR (GNR height is determined from linescans, such as that shown in figure 8.1a inset; some multilayer GNRs were observed, but we focus here on monolayer GNRs). The GNR of figure 8.1a has a width of 23.1 nm, a length greater than 600 nm, and exhibits straight, atomically smooth edges. Figure 8.1b shows a low temperature STM image, exhibiting finer structure in both the interior GNR terrace and the edge region. Such GNRs are seen to have a "bright stripe" running along each edge.

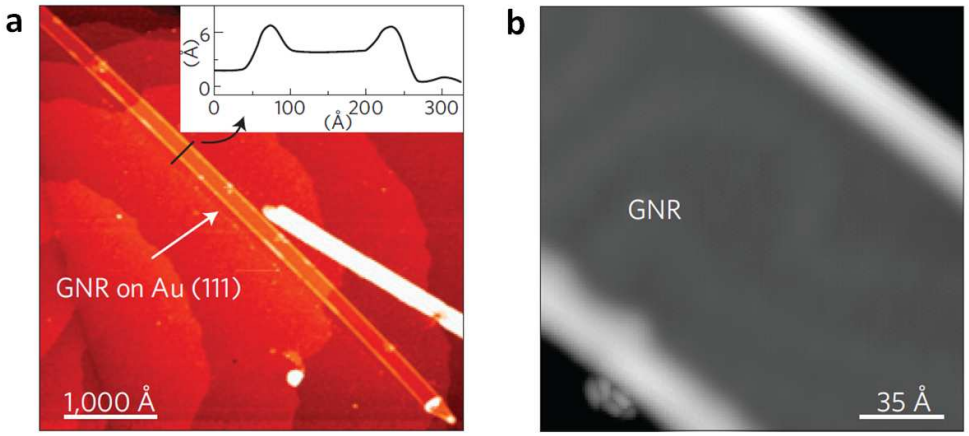

Figure 8.1: Topography of graphene nanoribbons (GNRs) on Au(111). (a) Constant-current STM image of a monolayer GNR on Au(111) at room temperature ($V = 1.5\,\mathrm{V}$, $I = 100\,\mathrm{pA}$). Inset shows the indicated line profile. (b) Higher resolution STM image of a GNR at $T = 7\,\mathrm{K}$ ($V = 0.2\,\mathrm{V}$, $I = 30\,\mathrm{pA}$, greyscale height map).

This stripe marks a region of curvature near the terminal edge of the GNR that has a maximum extension of $\sim 3\,\text{Å}$ above the mid-plane terrace of the GNR and a width of $\sim 30\,\text{Å}$ (see line scan in figure 8.1a inset). Such edge-curvature was observed for all high-quality GNRs examined in this study (more than 150, including GNRs deposited onto a Ru(0001) surface). This is reminiscent of curved edge structures observed previously near graphite step-edges [3].

During our large-scale topography scan on GNR samples at room temperature, we also observed other interesting byproducts during the synthesis process. Figure 8.2a and b shows a partially unzipped CNTs. An interesting question for the unzipping process is whether the unzipping direction is along the axis direction or along a spiral direction of the precursor CNTs. From a simple geometric relationship, we know that the ratio between the width of a GNR and the diameter of a CNT for partially unzipped CNTs should be π if the unzipping direction is along the axis direction (a schematic model is drawn in figure 8.2c), while the ratio should be smaller than π if the unzipping direction is along a spiral direction.

We measured the height of the CNT part (denoted as h) and the width of the GNR part (denoted as w) of the partially unzipped CNTs. The average ratio between the width of the GNR part and the measured height of the CNT part (w/h) is 3.2 ± 0.1. This average ratio is from 4 partially unzipped CNTs (and on each one, w/h is averaged from more than 10 line profiles of either part). This result implies that the unzipping process is along the axis of the precursor CNTs.

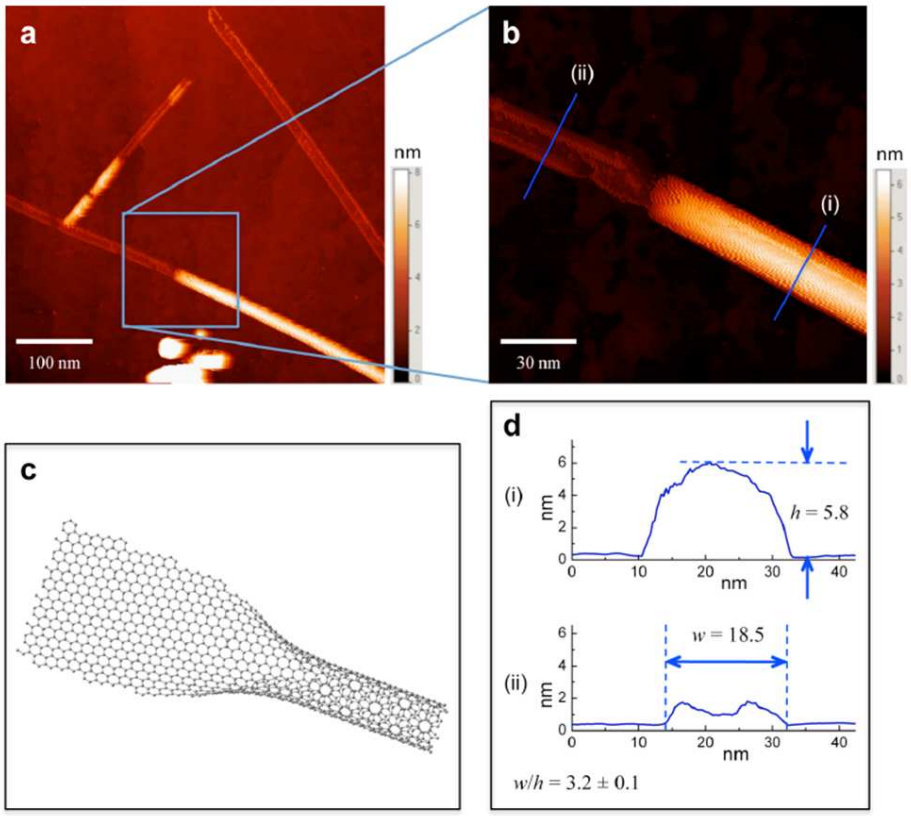

Figure 8.2: Characterization of partially unzipped CNTs. (a) STM image of partially unzipped CNTs ($V = 1.5\,\mathrm{V}$, $I = 100\,\mathrm{pA}$). (b) A zoom-in image of the GNR-CNT transition region of a partially unzipped CNT ($V = 1.5\,\mathrm{V}$, $I = 100\,\mathrm{pA}$). (c) Schematic drawing of a partially unzipped CNT with the unzipping direction along the axis direction of a precursor CNT. (d) Line profiles of the GNR part and the CNT part of the partially unzipped CNT in (b). The corresponding positions of the line profiles are marked by blue lines in (b).

We have also directly observed folded GNRs via STM, as shown in figure 8.3a and b. By comparing the curved edges of straight GNRs with the folded GNR edges we are able to show that the straight GNR edges are, in fact, terminal edges and are not folded or "scrolled". Figure 8.3a and b show STM images of folded GNRs on Au(111) with the folded edges marked by blue arrows. On different sections of the folded GNRs we are able to also observe the straight terminal curved edges that are typical for straight GNRs, as marked

by a green arrow in figure 8.3a. Roughened GNR edges (as marked by the white arrows in figure 8.3b) do not show such curvature (§9).

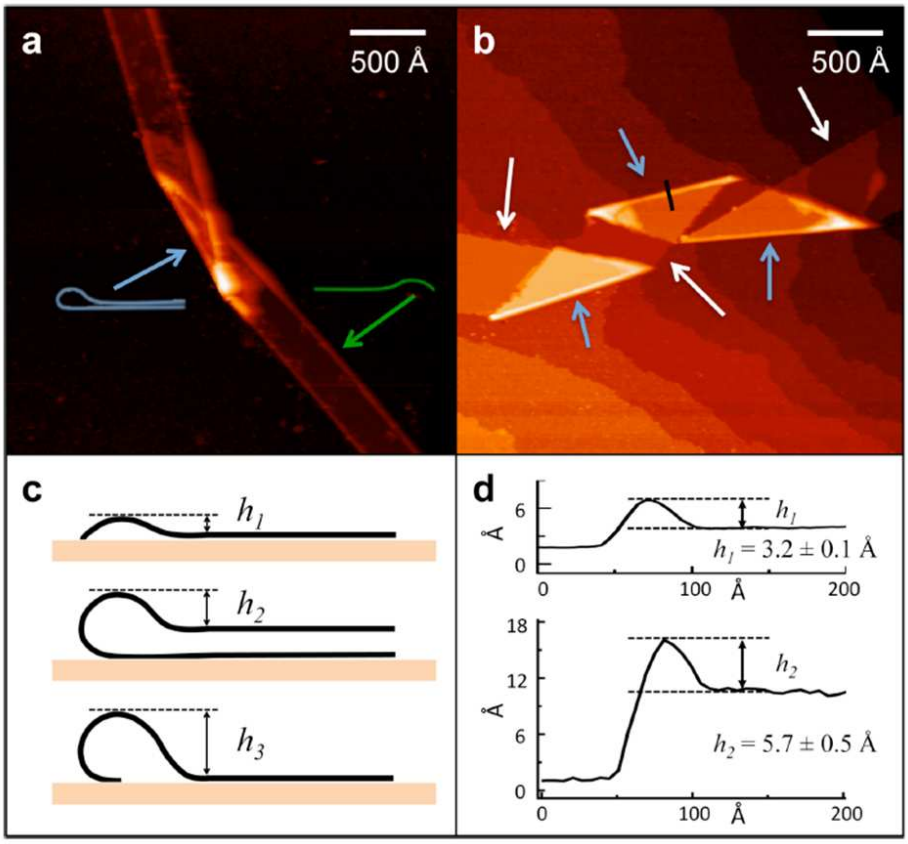

Figure 8.3: Comparison between terminal curved edges and folded edges. (a) Room temperature STM image of a folded GNR with atomically smooth edges ($V = 1.5\,\mathrm{V}$ and $I = 50\,\mathrm{pA}$). The blue arrow indicates a folded edge while the green arrow shows a terminal curved edge. (b) Room temperature STM image of a folded GNR etched by hydrogen plasma ($V = 1.8\,\mathrm{V}$ and $I = 50\,\mathrm{pA}$). The blue arrows indicate folded edges and the white arrows indicate roughened edges (the plasma etching (§9) has no effect on the folded edge characteristics). (c) Schematic structural model for a terminal curved edge, a folded edge, and a scrolled edge. (d) Line profiles of GNR terminal curved edge and GNR folded edge (compare to sketch in (c)). The top line profile is for terminal curved edges with "hump" height h_1 (typical linescan position of a straight GNR) and the bottom line profile is for folded edges with hump height h_2 (typical linescan position marked by the black line in b). h_2 is seen to be nearly twice as large as h_1, allowing these different edge geometries to be easily distinguished experimentally via STM. The terminal curved edges of straight GNRs are thus seen to not exhibit a folded structure.

We are able to quantitatively distinguish terminal curved edges from folded edges as

shown in the STM linescans of figure 8.3d. Due to the different curvature for these two classes of edges (as schematically drawn in the top and middle panels in figure 8.3c), the height of terminal curved edges (h_1) is expected to be less than that of folded edges (h_2) relative to the central flat terrace of a GNR. Figure 8.3d shows the results of actual measurement of h_1 and h_2. By averaging results from more than 4 different folded edges (h_2 is averaged from more than 10 line profiles for each different edge), we obtain an average $h_2 = 5.7 \pm 0.5$ Å for folded edges. For the terminal curved edges of straight GNRs, however, (as shown in figure 8.3a and figure 8.1) we obtain an average $h_1 = 3.2 \pm 0.1$ Å (obtained from averaging more than 10 linescans). h_2 is seen to be nearly a factor of two larger than h_1, allowing us to unambiguously distinguish between these two cases experimentally. We thus conclude that the terminal curved edges of straight GNRs are not folded. Another possible fold configuration is schematically shown in the bottom panel in figure 8.3c. From a simple geometric argument the height h_3 should be larger than h_2. Thus we can also rule out this possible structure for explaining the terminal curved edges of straight GNRs.

The chirality of a GNR is characterized by a chiral vector (n, m) or, equivalently, by chiral angle θ, as shown in figure 8.4a. GNRs having different widths and chiralities were deposited on a clean Au(111) surface and measured using STM. The atomic resolution of the LT STM allow us to unambiguously determine the chirality of GNRs. The lower part of figure 8.4b is the gold surface and the upper part is the GNR. The color contrast is optimized for showing periodic structure near the edge. We can clearly see rows of protrusions in the direction of the yellow line. In each row the protrusions have a spacing ~ 2.5 Å, indicating the rows are along the zigzag direction. Another zigzag direction is along the blue line. And the black line indicates the terminal edge orientation. The two ends of the back line connect adjacent equivalent sites, which can be determined by the relative position of the black line on the dim dots. By simply projecting this edge vector onto the basis vectors of graphene lattices (the yellow and blue arrows), the GNR chirality can be unambiguously determined. The GNR in figure 8.4b is an $(8, 1)$ GNR, corresponding to chiral angle of $\theta = 5.8°$.

8.2 Edge State of GNRs

To explore the local electronic structure of GNR edges, we have performed STS measurement on different positions (as marked) near the edge of the $(8, 1)$ GNR pictured in figure 8.5a, the dI/dV spectra are shown in figure 8.5c and d. dI/dV spectra measured within 24 Å of the GNR edge typically show a broad gap-like feature having an energy width of ~ 30 meV. This is very similar to the behaviour observed in the middle of large-scale graphene sheets, and is attributed to the onset of phonon-assisted inelastic electron tunneling for $|E| \geq 65$ meV [200]. This feature disappears further into the interior of the GNR, as expected, because of increased tunneling to the Au substrate [108]. Very close to the GNR edge, however, we observe further features in the spectra. The most dominant of these features are two peaks that rise up within the elastic tunneling region (that is at energies below the phonon-assisted inelastic onset) and which straddle zero bias. For the GNR shown in

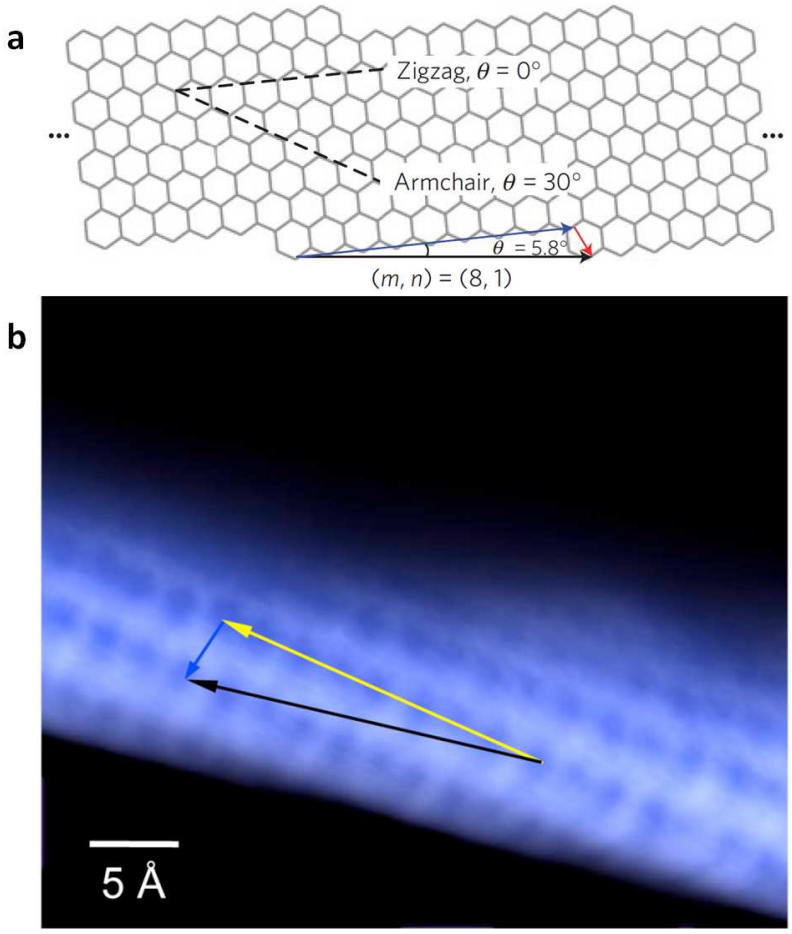

Figure 8.4: Determination of chirality of GNRs.(a) A schematic drawing of an $(8, 1)$ GNR. The chiral vector (n, m) connecting crystallographically equivalent sites along the edge defines the edge orientation of the GNR (black arrow). The blue and red arrows are the projections of the $(8, 1)$ vector onto the basis vectors of the graphene lattice. Zigzag and armchair edges have corresponding chiral angles of $\theta = 0°$ and $\theta = 30°$, respectively, whereas the $(8, 1)$ edge has an chiral angle of $\theta = 5.8°$. (b) STM image of an $(8, 1)$ GNR ($V = 0.3\,\mathrm{V}$, $I = 60\,\mathrm{pA}$). The lower part is the Au surface, and the upper part is the GNR. The black line is parallel to the edge orientation, connecting two neighboring equivalent sites. The yellow and blue arrows are along the zigzag directions of graphene lattices. The edge periodicity is 8α along the yellow line (α is the lattice constant of graphene), and 1α along the blue line.

figure 8.5a (which has a width of $19.5 \pm 0.4\,\mathrm{nm}$) the two peaks are separated in energy by a splitting of $\Delta = 23.8 \pm 3.2\,\mathrm{meV}$. Similar energy-split edge-state peaks have been observed in all the clean chiral GNRs that we investigated spectroscopically at low temperature. For example, the inset to figure 8.5c shows a higher resolution spectrum exhibiting energy-split edge-state peaks for a $(5, 2)$ GNR having a width of $15.6\,\mathrm{nm}$ and an energy splitting of

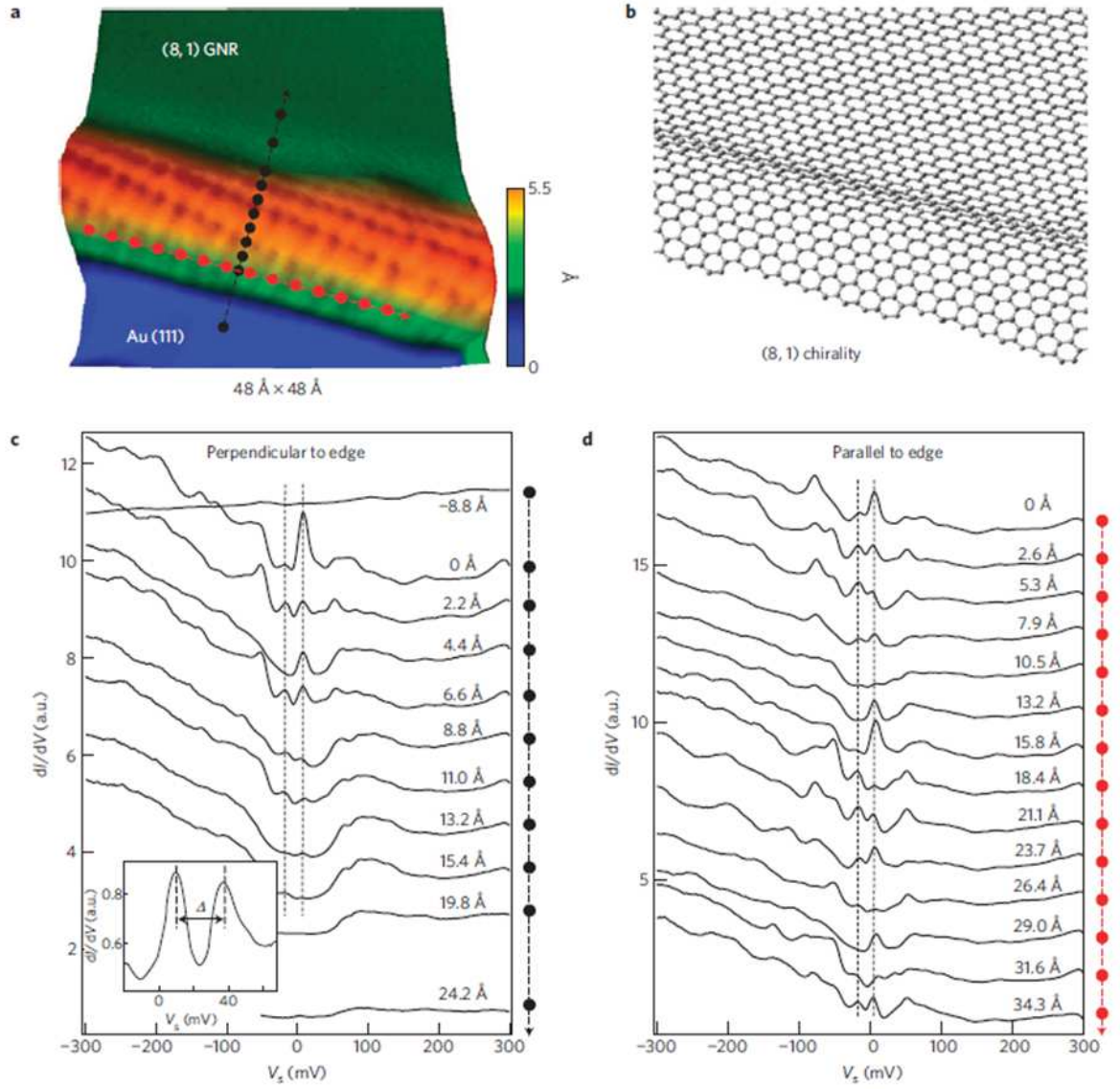

Figure 8.5: Edge states of GNRs. (a) Atomically-resolved topography of the terminal edge of an (8, 1) GNR with measured width of 19.5 ± 0.4 nm ($V = 0.3$ V, $I = 60$ pA, $T = 7$ K). (b) Structural model of the (8, 1) GNR edge shown in (a). (c) dI/dV spectra of the GNR edge shown in (a), measured at different points (black dots, as shown) along a line perpendicular to the GNR edge at $T = 7$ K. Inset shows a higher resolution dI/dV spectrum for the edge of a (5, 2) GNR with width of 15.6 ± 0.1 nm (initial tunneling parameters $V = 0.15$ V, $I = 50$ pA; wiggle voltage $V_{rms} = 2$ mV). The dashed lines are guides to the eye. (d) dI/dV spectra measured at different points (red dots, as shown) along a line parallel to the GNR edge shown in (a) at $T = 7$ K (initial tunneling parameters for (c) and (d) are $V = 0.3$ V, $I = 50$ pA; wiggle voltage $V_{rms} = 5$ mV).

$\Delta = 27.6 \pm 1.0$ meV. The two edge-state peaks are often asymmetric in intensity (depending on specific location in the GNR edge region), and their mid-point is often slightly offset from the Fermi energy (within a range of ± 20 meV). As seen in the spectra of figure 8.5c, the amplitude of the peaks grows as one moves closer to the terminal edge of the GNR, before falling abruptly to zero as the carbon/gold terminus is crossed.

The spatial dependence of the edge-state peak amplitude as one moves perpendicular from the GNR edge is plotted in figure 8.6a and shows exponential behavior. In this plot, peak amplitude and energies are determined by fitting Lorentzian curves to the two peaks observed in the measured spectra at each location in figure 8.5c over the range $-30\,\text{mV} < V < 30\,\text{mV}$. The energy positions of these peaks were found to be 6.7 ± 1.6 mV and -17.2 ± 2.2 mV. The positional dependence of the average peak amplitude of these two peaks is plotted. Error bars (shown when larger than plotted points) reflect the range of Lorentzian parameters that result in a good fit to the data. The edge-state spectra also vary as one moves parallel to the GNR edge, the parallel dependence of the edge-state peak amplitude is plotted in figure 8.6b, and oscillates with an approximate 20 Å period, corresponding closely to the 21 Å periodicity of an $(8, 1)$ edge.

We have also characterized monolayer GNRs having different chiralities and widths (the lengths of the GNRs used in these measurements are greater than 500 nm). In figure 8.6c, we plot the width dependence of the measured energy gap of GNR edge states for a broad range of chirality ($3.7° < \theta < 16.1°$). Energy gaps determined by Lorentzian fits to dI/dV peaks (centre-to-centre width), error bars reflect standard deviation due to spatial variation in spectra. GNR width measured as distance between the GNR edge mid-heights on opposite sides, error bars reflect standard deviation due to spatial variation along GNR axis. The measured edge-state energy splitting shows a clear inverse correlation with GNR width. Our gap values tend to be smaller than those observed previously for lithographically patterned GNRs (probably because of uncertainty in the edge structure of lithographically obtained GNRs [65]).

8.3 Theoretical Calculations on GNRs

To compare our experimental data with theoretical predictions for GNRs, we used a Hubbard model Hamiltonian, solved selfconsistently in the mean-field approximation [51], for an $(8, 1)$ GNR having the same width as the actual $(8, 1)$ GNR shown in figure 8.5a. The Hamiltonian:

$$H = -t \sum_{\langle ij \rangle, \sigma} [c^{\dagger}_{i\sigma} c_{j\sigma} + h.c.] + U \sum_{i} n_{i\uparrow} n_{i\downarrow} \tag{8.1}$$

consists of a one-orbital nearest-neighbour tight-binding Hamiltonian with an on-site Coulomb repulsion term. In this expression $c^{\dagger}_{i\sigma}$ and $c_{j\sigma}$ are operators that create and annihilate an electron with spin σ at the nearest-neighbor sites i and j respectively, $t = 2.7$ eV is a hopping integral [158], $n_{i\sigma} = c^{\dagger}_{i\sigma} c_{i\sigma}$ is the spin-resolved electron density at site i, and U is an on-site Coulomb repulsion. This GNR model is defined only by the π-bonding network. The termi-

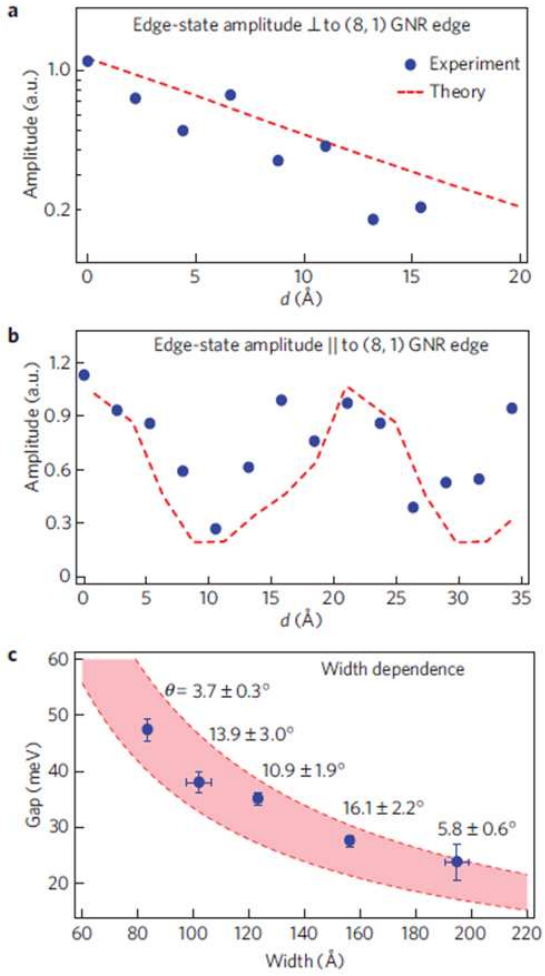

Figure 8.6: Position- and width-dependent edge-state properties. (a) Solid blue dots show experimental edge-state peak amplitude at points along a line perpendicular to the carbon/gold edge terminus (same positions as shown in figure 8.5c). Dashed red line shows the calculated LDOS at locations spaced perpendicular to the edge terminus for an (8, 1) GNR at the energy of the DOS peak nearest the band-edge. Theoretical LDOS values include a single globally constant offset to model the added contribution from Au surface LDOS, and a single globally constant multiplicative factor to model the unknown total area of the STM tunnel junction. (b) Solid blue dots show experimental average edge-state peak amplitude (same positions as shown in figure 8.5d). Dashed red line shows the theoretical edge-state LDOS for an $(8, 1)$ GNR at points parallel to the edge terminus (calculated as in (a)). The edge-state LDOS amplitude oscillates parallel to the edge with a 21 Å period. (c) Width dependence of the edge-state energy gap of chiral GNRs. From left to right, the chiralities of experimentally measured GNRs are $(13, 1)$, $(3, 1)$, $(4, 1)$, $(5, 2)$, and $(8, 1)$ respectively, corresponding to a range of chiral angle $3.7° < \theta < 16.1°$. The pink shaded area shows the predicted range of edge-state bandgaps as a function of width, evaluated for chiral angles in the range $0° < \theta < 15°$ ($U = 0.5t$, $t = 2.7\,\text{eV}$, [194]).

nal σ-bonds at the GNR edges are considered to be passivated and do not alter the π-system (this should, in general, correctly model a range of different possible edge-adsorbate bonding configurations [170, 74], including the likely oxygen-related functional group termination of our own GNRs [90]). The out-of-plane curvature seen experimentally near GNR edges is not included in this model because the measured radii of curvature are sufficiently large (> 20 Å) that they are not expected to significantly affect GNR electronic structure [17] (we tested this conjecture by including the observed curvature in some calculations, and found that it has no significant effect – either from σ-π coupling or from pseudofield effects – on the calculated GNR electronic structure). The effect of the gold substrate here is taken only as a charge reservoir that can slightly shift the location of E_F within the GNR band structure and reduce the magnitude of the effective U parameter by means of electrostatic screening (the experimental charge-induced energy shifts seen here are within the range of charge-induced energy shifts observed previously for CNTs on Au [37]).

We first calculated the GNR electronic structure for $U = 0$, which effectively omits the electron-electron interactions responsible for the onset of magnetic correlations. This results in the theoretical band structure and density of states (DOS) shown as blue dashed lines in figure 8.7a, b. The finite width of the GNR leads to a family of subbands in the band structure, with no actual bandgap (figure 8.7a). A flat band at $E = 0$ due to localized edge states leads to a strong van Hove singularity (that is, a peak) in the DOS at $E = 0$ (figure 8.7b). The DOS in this case does not resemble what is seen experimentally.

We next calculated the $(8, 1)$ GNR electronic structure for $U > 0$. Here the electron-electron interactions lift the degeneracy of the edge states by causing ferromagnetic correlations to develop along the GNR edges and antiferromagnetic correlations to develop across the GNR. This leads to a spin-polarization of the edge states that splits the single low-energy peak seen in the $U = 0$ DOS into a series of van Hove singularities, thus opening up a gap at $E = 0$. Such behaviour is seen as solid red lines in the band structure and DOS of figure 8.7a, b. We identify the lowest-energy pair of van Hove singularities with the pair of peaks observed experimentally near zero bias for GNR edges. We focus our experiment/theory comparison on the low-energy regime ($|E| \leq 65$ meV) because higher energy experimental features are complicated by the onset of phonon-assisted inelastic tunneling [22] (the low-energy edge-state peaks, by contrast, do not have the characteristics of inelastic modes).

We find that our experimental spectroscopic edge-state data for the $(8, 1)$ GNR is in agreement with model Hamiltonian calculations for $U = 0.5t$. The theoretical bandgap of 29 meV is very close to the experimentally observed value of 23.8 ± 3.2 meV (the value of U used here is lower than a value obtained previously from a first-principles calculation [193], presumably because of screening from the gold substrate). Our experimentally observed energy-split spectroscopic peaks thus provide evidence for the formation of spin-polarized edge states in pristine GNRs (such splitting does not arise for the non-magnetic $U = 0$ case described above).

We are further able to compare the spatial dependence of the calculated edge states with the experimentally measured STS results. The dashed line in figure 8.6a shows the

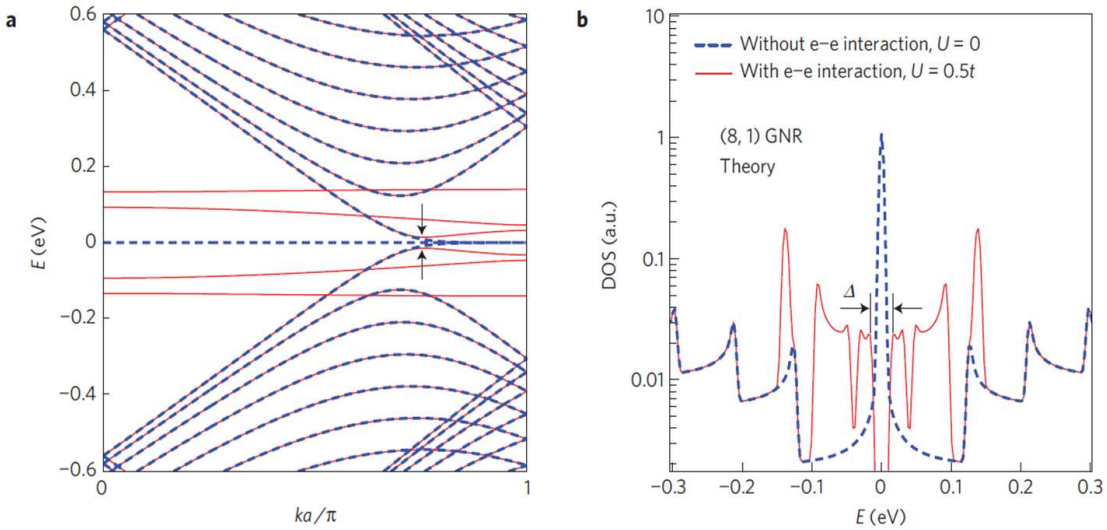

Figure 8.7: Theoretical band structure and density of states (DOS) of a 20-nm-wide $(8, 1)$ GNR. (a) Dashed blue line shows the calculated GNR electronic structure in the absence of electronelectron interactions ($U = 0$). Solid red line shows the calculated GNR electronic structure for $U = 0.5t$ ($t = 2.7\,\text{eV}$). Finite $U > 0$ splits degenerate edge states at $E = 0$ into spin-polarized bands, opening a bandgap (arrows). (b) Dashed blue line shows the $(8, 1)$ GNR DOS for the $U = 0$ case. The peak at $E = 0$ is due to the degeneracy of edge states in the absence of electronelectron interactions. Solid red line shows the $(8, 1)$ GNR DOS for $U = 0.5t$. The opening of the bandgap (arrows) reflects the predicted energy splitting due to the onset of magnetism in spin-polarized edge states for $U > 0$, and compares favourably with the experimental data for the $(8, 1)$ GNR of figure 8.5.

theoretical LDOS calculated at the energy of the low-energy edge-state peaks as one moves perpendicularly away from the GNR edge and into the $(8, 1)$ GNR interior. The predicted exponential decay length of $\sim 12\,\text{Å}$ is in reasonable agreement with the experimental data. The variation seen in the calculated LDOS of the edge state in the direction parallel to the GNR edge also compares favourably with our experimental observations (figure 8.6b). The oscillation in edge-state amplitude is seen to arise from "kinks" in the zigzag edge structure resulting from the chiral nature of the $(8, 1)$ GNR edge (see the edge structure of figure 8.5b, each of the two dips in spectroscopic amplitude occurs at the location of a kink).

We are similarly able to compare the GNR width dependence of our experimentally measured edge-state gaps to theoretical calculations. As the measured GNRs having different widths also have different chiralities, we have calculated the theoretical edge-state gap versus width behaviour over the chirality range $0° < \theta < 15°$ (it will be useful in the future to measure the local electronic properties of armchair GNRs ($\theta = 30°$), which are predicted to have no edge states). The pink shaded region in figure 8.6c shows the results of our calculations, and compares favorably with our experimentally observed width-dependent edge-state gap. This provides strong evidence that the edge-state gap we observe experimentally is

not a local effect, as might occur, say, in response to some unknown molecules bound to the GNR edge, but rather depends on the full GNR electronic structure, including interaction between the edges.

8.4 Conclusions

With our high resolution STM, we have demonstrated unambiguously and for the first time that it is possible to create graphene nanoribbons with atomically smooth edges. Furthermore, we demonstrate that these chiral nanoribbons exhibit an electronic edge state that has novel spatial dependence and energy splitting. By comparing experimental nanoribbon edge state data with theoretical simulations, the excellent agreement provides evidence for the existence of spin-polarized edge states coupled magnetically across the width of a single microscopic nanoribbon.

9 Controlling the Edge Termination of GNRs

The edges of graphene exhibit several unique features, such as the presence of localized edge states, and are anticipated to provide a powerful means of controlling the electronic properties of this two-dimensional material [129, 170, 195]. Such edge-dependent behavior is expected to be even more pronounced in ultra-narrow strips of graphene, dubbed nanoribbons, where edges make up an appreciable fraction of the total nanostructure volume, thus creating new nanotechnology opportunities. The previous chapter has presented the observation of edge states in chiral GNRs, however, due to the complex chemical synthesis procedures [90] and the curved edge morphology (figure 8.1), it was not possible to control and correlate nanoribbon edge electronic structure with specific chemically defined terminal edge group.

In this chapter, we will report the ability to control the microscopic edge termination of high quality GNRs via hydrogen plasma etching. We find that hydrogen plasma etches away the original unknown edge groups and develops segments with different chiralities along the edge. Using a combination of high-resolution scanning tunneling microscopy and first-principles calculations, we have determined the exact atomic structure of plasma-etched GNR edges and established the chemical nature of terminating functional groups for zigzag, armchair and chiral edge orientations. We find that the edges of hydrogen-plasma-etched GNRs are generally free of structural reconstructions and are terminated by hydrogen atoms with no rehybridization of the outermost carbon edge atoms. Both zigzag and chiral edges show the presence of edge states.

9.1 Hydrogen Plasma Treated GNRs on Au(111)

The investigated GNRs were obtained by hydrogen plasma treatment [190] of GNRs deposited onto a Au(111) substrate and then plasma etched. The GNRs were chemically fabricated using carbon nanotube unzipping methods [90]. The Au(111) substrate was cleaned by standard sputter-annealing procedures in ultra-high-vacuum (UHV) before be-

ing transferred *ex situ* for spin-coating of GNRs. The sample was subsequently exposed to hydrogen plasma [190] for 15 minutes. The sample was then placed back into the UHV chamber where it was annealed up to 500 °C for several hours before being transferred *in situ* for UHV STM measurements. The measurements were performed using an Omicron VT-STM operating at room temperature.

Prior to hydrogen plasma treatment, these GNRs typically exhibit curved edges [173, 140, 3] that hinder access via STM to the very outermost edge atoms. The chemical nature of the pre-etched outermost atoms is therefore unknown, but based on the GNR chemical treatment they are likely terminated with some form of oxygen-containing functional groups [90]. Figure 9.1a shows a typical room temperature STM image of a GNR that has been deposited onto Au(111) before being etched by hydrogen plasma. The line profile indicates typical edge curvature, where the curved part of the edge has a width of 5 nm and a height of 0.3 nm above the center terrace region of the GNR.

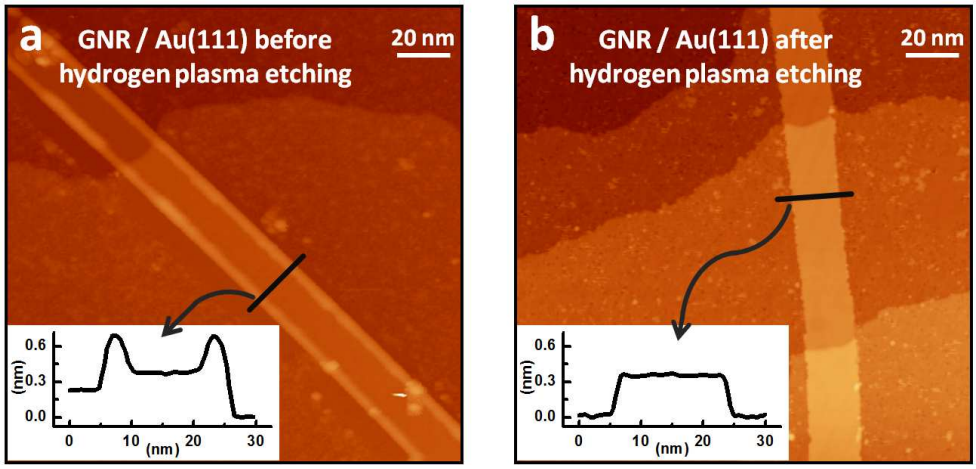

Figure 9.1: Effect of hydrogen plasma treatment on GNRs deposited on a Au(111) substrate. (a) Room temperature constant-current STM topograph ($V = 1.5\,\mathrm{V}$, $I = 100\,\mathrm{pA}$) of a GNR before hydrogen plasma etching. (b) Room temperature STM image of a GNR after hydrogen plasma treatment ($V = 1.97\,\mathrm{V}$, $I = 50\,\mathrm{pA}$). Insets show the indicated line profiles.

The effect of hydrogen plasma treatment on these GNRs is two-fold. First, the hydrogen plasma etches away the original edge groups, and substitutes them with hydrogen (the simplest possible monovalent edge termination). Second, the edges become significantly rougher and develop short segments (several nanometers long) that display different chiralities within the same GNR (figures 9.1b, 9.2a-e) (the entire GNR thus does not achieve global thermodynamic equilibrium that would result in an overall preferred edge orientation). The combination of these two factors changes the interaction between the edges and the substrate, resulting in a flat, uncurved morphology with the outermost edge atoms being more exposed. Figure 9.1b shows that the bright strips due to edge curvature are no longer visible in etched GNRs. Instead, the etched GNRs are flat, with a height of $\sim 3.3\,\text{Å}$ for

typical imaging parameters (there is little variation in the height of etched ribbons when imaged within a $\pm 2\,\mathrm{V}$ bias window). The height of etched GNRs is similar to the height of the interior terrace of unetched GNRs, indicating that the etching process starts from the edges and moves towards the center.

Higher resolution topographic images (figures 9.2a-e) on different parts of an etched GNR show the honeycomb structure of the interior graphene. By superimposing a hexagonal lattice structure, we are able to identify the chirality of each segment of the GNR edge. Figures 9.2c-e show close-up images of three different types of representative GNR edge segments: a zigzag segment, a chiral edge segment orientated along the (2, 1) vector of the graphene lattice, and an armchair segment, respectively. The 2-nm-long zigzag edge segment (figure 9.2c) appears as a sequence of bright spots visible along the edge, which then decays into the interior graphene. This segment exhibits a small depression near the middle of the outer row of edge atoms, while the second row of edge atoms next to the depression appear to be brighter than adjacent second row atoms. The (2, 1) chiral edge segment (figure 9.2d) shows a periodic modulation in STM intensity along its length. Comparison with a superimposed lattice structure shows that the periodic bright spots are localized along zigzag-like fragments. A break in the periodic pattern is observed in the middle of the chiral edge, possibly due to the presence of a vacancy defect. The armchair edge (figure 9.2e), in contrast, shows no edge enhancement in the STM intensity. Instead, the armchair edge exhibits a pronounced standing-wave feature with periodicity of $\sim 0.4\,\mathrm{nm}$ at the $-0.97\,\mathrm{V}$ bias voltage used in our measurements.

9.2 Thermodynamic Calculations of Edge Terminations

In order to understand the electronic properties of the GNR edges probed in this manner, the bonding arrangement of hydrogen atoms at the GNR edges must be determined. This information then enables calculation of the GNR electronic local density of states which can be compared to the STM data to self-consistently confirm the structural model and electronic behavior. Our strategy for performing this procedure is to first calculate the energetic stability of different edge structures, and then to use the thermodynamically favorable structures to guide our first-principles electronic property calculations which are then compared to experiment.

We determined the thermodynamically most favorable structures by calculating the edge formation energy of different hydrogen-bonded GNR edge structures in contact with a reservoir of hydrogen. The stabilities of various edge terminations were investigated using GNR models of approximately 1.5 nm width and a plane-wave-based computational scheme implemented in the Quantum-ESPRESSO package [55]. In these calculations we used a combination of ultrasoft pseudopotentials [178], and plane-wave kinetic energy cutoffs of 30 Ry and 300 Ry for wavefunctions and charge density, respectively. Edge carbon atoms were allowed to terminate with either one (sp^2 hybridization) or two (sp^3 hybridization) hydrogen atoms, and we restricted our consideration only to structural terminations having the same

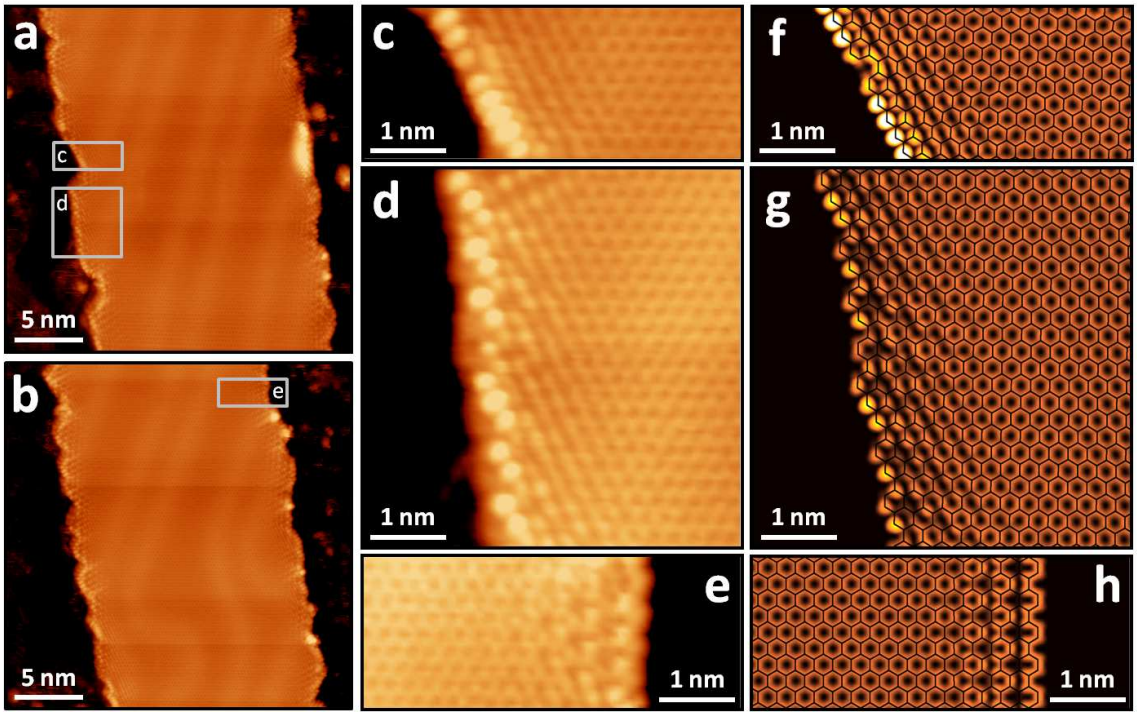

Figure 9.2: Atomically-resolved STM topographs of GNR edges: experiment vs. first-principles simulations. (a, b) Larger scale room temperature STM topographs of two segments of a GNR ($V = 0.97\,\mathrm{V}$, $I = 50\,\mathrm{pA}$). (c, d, e) Zoomed-in atomically-resolved images of edge segments circled in (a) and (b) having different chiralities: a zigzag edge ($V = 0.97\,\mathrm{V}$, $I = 50\,\mathrm{pA}$), a (2, 1) chiral edge ($V = 0.97\,\mathrm{V}$, $I = 50\,\mathrm{pA}$), and an armchair edge ($V = 0.97\,\mathrm{V}$, $I = 50\,\mathrm{pA}$), respectively. (f, g, h) STM images simulated from first principles using the Tersoff-Hamann approximation for the STM tunneling current, the same bias voltage as in the experiments, and the thermodynamically most stable hydrogen edge configuration. These simulations suggest that the plasma treatment results in simple edge termination with one hydrogen atom saturating each dangling bond. The atomic structures of the underlying lattices of carbon atoms are shown as black lines.

periodicity as the unterminated bare edge, since such symmetry is observed experimentally. Different hydrogenated edge structures differ in their local chemical composition, and thus their formation energies per edge unit length depend on the chemical potential of hydrogen, μ_H, according to [156],

$$G(\mu_H) = \frac{1}{2a}\left(E_{GNR} - \frac{N_C}{2}E_{graphene} - \frac{N_H}{2}E_{H_2} - N_H\mu_H\right) \tag{9.1}$$

where a is the edge periodicity, N_C and N_H are the number of carbon and hydrogen atoms per unit cell, and E_{GNR} and $E_{graphene}$ are the total energies of the model GNR and ideal

graphene per unit cell, respectively. The chemical potential, μ_H, here defined using the total energy E_{H_2} of an H_2 molecule as a reference, is a free parameter which depends on particular experimental conditions. For this reason, we analyzed a broad range of chemical potentials, as shown in figure 9.3. Structures having the lowest formation energies, $G(\mu_H)$, at a given μ_H are highlighted with thick lines and the corresponding structures are shown below with the π bonding network emphasized. Note that more stable structures with long-range periodicity can in principle be realized [181], but they are not observed here since global thermodynamic equilibrium is not achieved under the present experimental conditions.

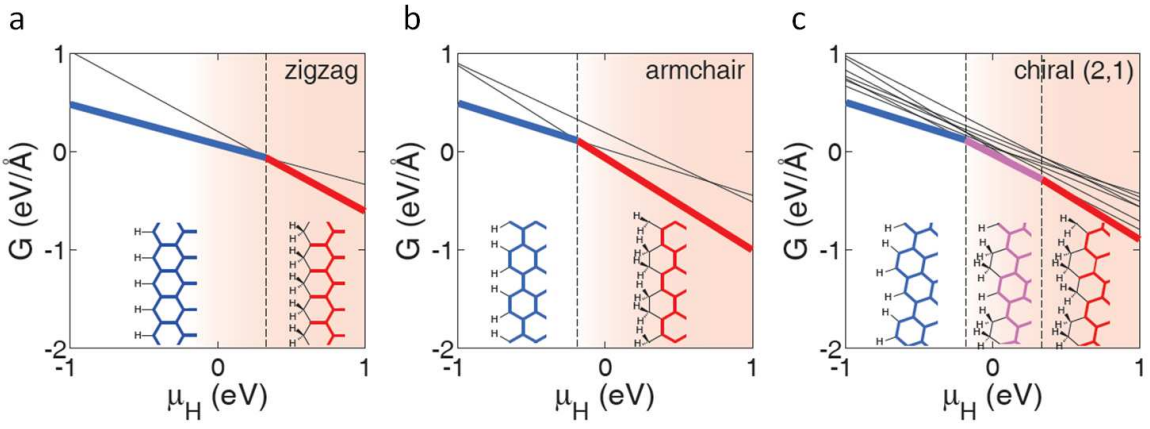

Figure 9.3: Thermodynamic stability of hydrogenated graphene edges calculated from first principles. Edge formation energy per unit length (G) as a function of chemical potential of hydrogen (μ_H) calculated from first principles for various hydrogen termination patterns for (a) a zigzag, (b) an armchair, and (c) a (2,1) chiral edge of a GNR. The structures for stable edge terminations are sketched below. The sp^2 carbon atom bonding networks are highlighted in color (matched to the energy plot) while sp^3 carbon atoms and terminating bonds are shown in black. The shaded areas denote the range of chemical potentials μ_H for which graphane is more stable than graphene.

For the zigzag edge (figure 9.3a), two hydrogen configurations are possible – either a "simple" sp^2-bonded hydrogen zigzag edge for $\mu_H < 0.33\,\text{eV}$ or an sp^3-bonded edge with two hydrogen atoms per carbon edge atom for $\mu_H > 0.33\,\text{eV}$ (the latter results in a Klein edge π bonding network topology [95]). The shaded region in figure 9.3 shows the condition for graphene to transform into graphane [167, 40] with a full basal hydrogenation of stoichiometry CH ($\mu_H > -0.2\,\text{eV}$). Since this is not observed experimentally, meaning $\mu_H < -0.2\,\text{eV}$, we are able to exclude the Klein edge scenario. We thus conclude that the zigzag GNR is terminated with one hydrogen atom per carbon edge atom.

The armchair edge (which has two carbon edge atoms per unit cell) can, in principle, support three possible hydrogen terminations. As shown in figure 9.3b, however, only two of them have regions of stability – either both carbon edge atoms terminated with one hydrogen atom ($\mu_H < -0.19\,\text{eV}$) or both carbon edge atoms terminated with two hydrogen

atoms ($\mu_H > -0.19\,\mathrm{eV}$). These two configurations are equivalent from the point of view of the π electron system topology, and both have an identical electronic structure that is consistent with the experimental observation. However, the condition of observing graphene instead of graphane requires $\mu_H < -0.2\,\mathrm{eV}$, thus indicating that the armchair edge is most likely terminated with one hydrogen atom per carbon atom.

The situation is somewhat more complicated for the case of the (2,1) chiral edge, which has three inequivalent edge atoms per unit cell and thus can realize, in principle, eight distinct possible hydrogen terminations. Only three of these, however, have regions of stability (figure 9.3c): the case where all edge atoms are terminated with one hydrogen atom ($\mu_H < -0.19\,\mathrm{eV}$), the case where two adjacent edge atoms are terminated with two hydrogen atoms and the third edge atom is bonded only to one hydrogen ($-0.19\,\mathrm{eV} < \mu_H < 0.33\,\mathrm{eV}$), and the case where all three edge atoms are each terminated with two hydrogen atoms ($\mu_H > 0.33\,\mathrm{eV}$). The first two structures realize the same π electron network topology. However, because the upper limit of μ_H realized under the present experimental condition is $-0.2\,\mathrm{eV}$, we conclude that the (2,1) chiral edge termination should involve only one hydrogen atom per edge carbon atom.

To further confirm that the calculated thermodynamically favorable edge terminations correspond to what we observe experimentally, we performed first-principles simulations of the STM images for these structures (figures 9.2f-h) and compared them to our experimental data. The models for the first-principles simulations of STM images are approximately 7-nm-wide graphene nanoribbons with hydrogen-terminated edges. These large-scale simulations of STM images were performed using the local spin density approximation of density functional theory as implemented in the SIESTA package [168] and a combination of a double-ζ plus polarization basis set, norm-conserving pseudopotentials [177], and a mesh cutoff of 200 Ry. The atomic positions have been fully relaxed. The STM intensities were calculated using the Tersoff-Hamann approximation [176] assuming a fixed tip sample distance of 5 a.u. and a negative bias of $-0.97\,\mathrm{V}$ in accordance with experimental conditions. The structural models have utilized the energetically most stable termination (i.e. one hydrogen atom per edge carbon atom), and did not involve any covalent bonding reconstructions other than six-membered rings.

The resulting simulated STM images nicely match the experimental data. This can be seen first for the zigzag segment in figure 9.2f, which shows a sequence of bright spots along the edge. A single carbon atom was removed from the center of the zigzag edge in the simulation, and this is seen to explain the depression in the middle of the outer row of atoms and the slight enhancement in the second row of carbon atoms. The simulation of the (2,1) chiral edge (figure 9.2g) shows very pronounced edge states in agreement with the experimental data. It also features the observed intensity modulation along the length of this edge, which results from edge states localized along the zigzag-like fragments. An extra pair of edge carbon atoms was added to the middle of this edge segment which effectively elongates one of the zigzag-like fragments and shortens the neighboring one, thus explaining a break in the periodic pattern observed in the middle of the experimental edge segment. The simulated armchair segment (figure 9.2h) does not show intensity enhancement along

the edge, as seen experimentally for this structure. This is consistent with the fact that this edge orientation does not give rise to localized states. The armchair edge simulation also features a standing-wave pattern, in agreement with previously reported predictions [182, 141] and the experimental data of figure 9.2e.

As a further comparison, we have simulated other possible edge terminations for (2, 1) chiral edge. The (2,1) chiral edge has 3 inequivalent positions of edge carbon atoms (figure 9.4). Thus, there are possible $2^3 = 8$ different configurations in which either 1 or 2 hydrogen atoms terminate each edge carbon atom. The simulated STM images of all 8 configurations are shown in figure 9.4a-h. Only three of these configurations (figures 9.4a, g, h) have

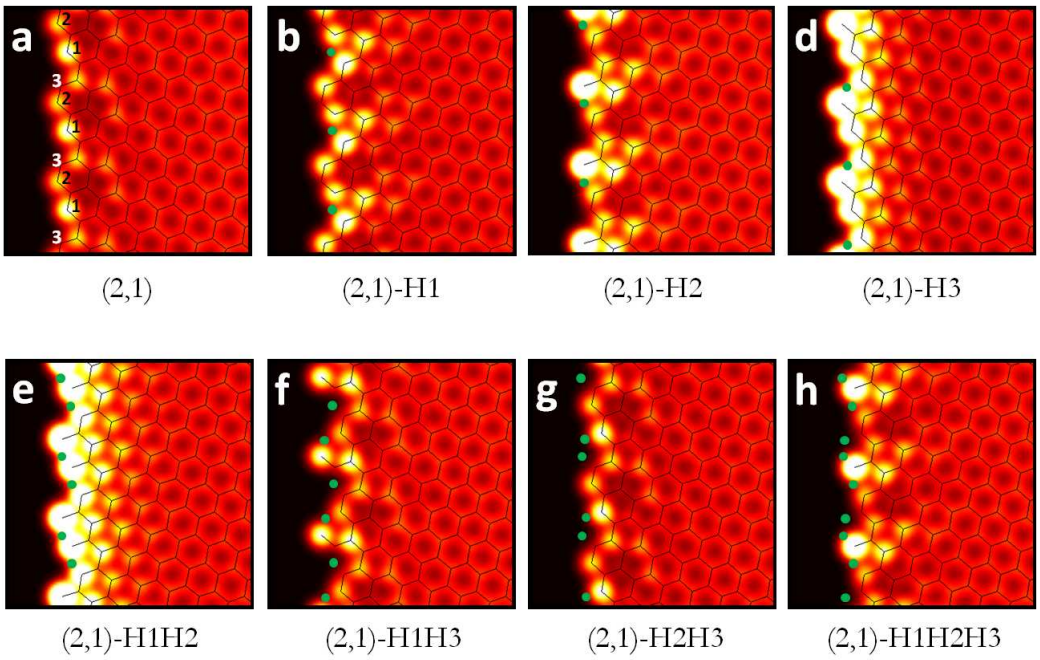

Figure 9.4: Simulated STM images of different hydrogen terminated configurations for a (2, 1) chiral edge. Electronically equivalent configurations shown in panels a and g are the thermodynamically most stable terminations (see figure 9.3c) and match the experiment. The images were simulated using a tight-binding Hamiltonian and the Tersoff-Hamann approximation. The bias voltage is the same as in experiments ($V = -0.97\,\mathrm{V}$). The solid lines correspond to covalent bonds between the neighboring sp^2 carbon atoms (sp^3-hybridized edge atoms are shown as green dots).

regions of stability as shown in figure 9.3c. Only two of them, the normal chiral edge with one hydrogen atom per edge carbon atom (figure 9.4a) and the one with two hydrogen atoms terminating edge carbon atoms in position 2 and 3 (figure 9.4g) qualitatively agree with the experimental STM image (figure 9.2d). These two cases are electronically equivalent since they share the same π-electron system boundary. However, the structure with two hydrogen atoms per carbon atom lies in the regime where graphene is thermodynamically less stable

than graphane, and so we conclude that the observed termination of the (2,1) chiral edge has one hydrogen atom per edge carbon atom.

We also compare the experimental data and simulations for GNR edge electronic structure by examining average line profiles perpendicular to zigzag and armchair edges. We took more than 20 parallel line scans from the experimental data in the shaded regions of figures 9.5a and b, and then averaged them to get the blue curves in figures 9.5e and f. For the simulation images, we first used a mean-filtering image processing method to account for the finite size of the STM tip, and we then took an average of parallel line scans oriented perpendicular to the edges. The theoretical line scans obtained in this way are depicted as red dashed lines in figures 9.5e and f, they are offset vertically for clarity.

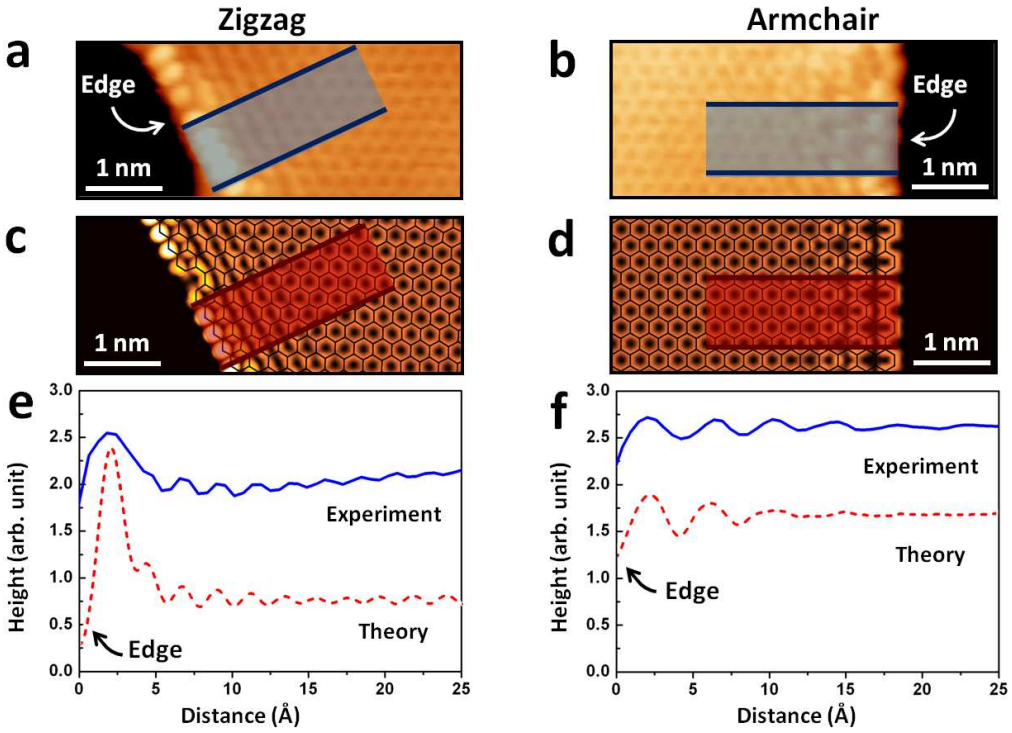

Figure 9.5: Comparison of line profiles derived from experiment and simulation for GNR zigzag and armchair edges. (a, b) Experimental images ($V = -0.97\,\mathrm{V}$, $I = 50\,\mathrm{pA}$) of (a) GNR zigzag and (b) GNR armchair edges, with blue regions showing areas where linescans were averaged. (c) GNR zigzag and (d) GNR armchair edge LDOS simulations with red areas indicating where linescans were averaged. Average linescan profiles for the experiment (blue lines) and the simulations (red lines) are shown for (e) GNR zigzag and (f) GNR armchair edges.

For the zigzag edge, both the experimental and theoretical line scans exhibit an LDOS oscillation with a period of 2.1 Å, which is close to the distance between neighboring zigzag chains. This oscillation can be explained by the fact that the localized edge state decays

exponentially over zigzag chains away from the edge. For the armchair edge, a different modulation period of 3.8 Åis seen. This can be explained by intervalley scattering of electrons [141]. The zigzag edge is seen to have a large buildup in LDOS near the edge (in both the experiment and the simulation) which is not seen for the armchair edge. This is due to the fact that the zigzag edge has an edge state while the armchair edge does not.

9.3 Conclusions

In this chapter, we discussed a scanning tunneling microscopy (STM) study of graphene nanoribbons (GNRs) that are treated by hydrogen plasma etching. We find that hydrogen plasma etches away the original edge groups and develops segments with different chiralities along the edge. We have closely examined three different types of representative GNR edge segments: zigzag segments, (2, 1) chiral edge segments, and armchair segments. Comparison between our experimental data and first-principles theoretical simulation of energetically most favorable structures shows good agreement. For example, we find that the edge carbon atoms of our etched GNRs are terminated by only one hydrogen atom, and that both zigzag and chiral edges show the presence of edge states. The edges of hydrogen-plasma-etched GNRs are seen to be generally free of structural reconstructions and are terminated by hydrogen atoms with no rehybridization of the outermost carbon edge atoms.

Bibliography

[1] A. R. Akhmerov and C. W. J. Beenakker. Boundary conditions for Dirac fermions on a terminated honeycomb lattice. *Phys. Rev. B* 77, p. 085423 (2008).

[2] GJ Ashwell, WD Tyrrell, and AJ Whittam. Molecular rectification: Self-assembled monolayers in which donor-(π-bridge)-acceptor moieties are centrally located and symmetrically coupled to both gold electrodes. *Journal of the American Chemical Society* 126, no. 22, pp. 7102–7110 (2004).

[3] F Atamny, TF Fassler, A Baiker, and R Schlogl. On the imaging mechanism of monatomic steps in graphite. *Applied Physics A: Materials Science & Processing* 71, no. 4, pp. 441–447 (2000).

[4] U Bach, D Lupo, P Comte, JE Moser, F Weissortel, J Salbeck, H Spreitzer, and M Gratzel. Solid-state dye-sensitized mesoporous TiO2 solar cells with high photon-to-electron conversion efficiencies. *Nature* 395, no. 6702, pp. 583–585 (1998).

[5] Vincenzo Balzani, Margherita Venturi, and Alberto Credi. *Molecular Devices and Machines: A Journey into the Nanoworld*. Wiley-VCH Verlag GmbH & Co. (2003).

[6] E. J. Baran and K. H. Lii. Vibrational spectra of the layered compound $[(VO_2)_2(4,4\text{-bipy})_{0.5}(4,4'\text{-Hbipy})(PO_4)]\cdot H_2O$. *Zeitschrift für Naturforschung Section B—A Journal of Chemical Sciences* 58, no. 5, pp. 485–488 (2003).

[7] J. Bardeen. Tunneling from a many-particle point of view. *Physical Review Letters* 6, no. 2, pp. 57–59 (1961).

[8] Salvador Barraza-Lopez, Michael C. Avery, and Kyungwha Park. First-principles study of a single-molecule magnet Mn_{12} monolayer on the Au(111) surface. *Physical Review B (Condensed Matter and Materials Physics)* 76, no. 22, 224413 (2007).

[9] L. Bartels, G. Meyer, and K.-H. Rieder. Basic Steps of Lateral Manipulation of Single Atoms and Diatomic Clusters with a Scanning Tunneling Microscope Tip. *Phys. Rev. Lett.* 79, pp. 697–700 (1997).

[10] L Bartels, G Meyer, and KH Rieder. Controlled vertical manipulation of single CO molecules with the scanning tunneling microscope: A route to chemical contrast. *APPLIED PHYSICS LETTERS* 71, no. 2, pp. 213–215 (1997).

[11] J. V. Barth, H. Brune, G. Ertl, and R. J. Behm. Scanning tunneling microscopy observations on the reconstructed Au(111) surface: Atomic structure, long-range superstructure, rotational domains, and surface defects. *Phys. Rev. B* 42, pp. 9307–9318 (1990).

[12] S. Bedwani, D. Wegner, M. F. Crommie, and A. Rochefort. Strongly Reshaped Organic-Metal Interfaces: Tetracyanoethylene on Cu(100). *Phys. Rev. Lett.* 101, p. 216105 (2008).

[13] G Binnig and H Rohrer. Scanning tunneling microscopy. *Helvetica Physica Acta* 55, no. 6, pp. 726–735 (1982).

[14] G Binnig, H Rohrer, C Gerber, and E Weibel. Tunneling through a controllable vacuum gap. *Applied Physics Letters* 40, no. 2, pp. 178–180 (1982).

[15] G. Binnig, H. Rohrer, Ch. Gerber, and E. Weibel. 7×7 reconstruction on Si(111) resolved in real space. *Phys. Rev. Lett.* 50, pp. 120–123 (1983).

[16] J. M. Blanco, C. González, P. Jelínek, J. Ortega, F. Flores, R. Pérez, M. Rose, M. Salmeron, J. Méndez, J. Wintterlin, and G. Ertl. Origin of contrast in STM images of oxygen on Pd(111) and its dependence on tip structure and tunneling parameters. *Phys. Rev. B* 71, p. 113402 (2005).

[17] X. Blase, Lorin X. Benedict, Eric L. Shirley, and Steven G. Louie. Hybridization effects and metallicity in small radius carbon nanotubes. *Phys. Rev. Lett.* 72, pp. 1878–1881 (1994).

[18] M.-L. Bocquet, H. Lesnard, and N. Lorente. Inelastic Spectroscopy Identification of STM-Induced Benzene Dehydrogenation. *Phys. Rev. Lett.* 96, p. 096101 (2006).

[19] Marie-Laure Bocquet and Nicolas Lorente. Probing the proton location in a water bilayer on Pd (111) by inelastic spectroscopy simulations. *J. Chem. Phys.* 130, no. 12, 124702 (2009).

[20] Lapo Bogani and Wolfgang Wernsdorfer. Molecular spintronics using single-molecule magnets. *Nature Materials* 7, no. 3, pp. 179–186 (2008).

[21] M. Böhringer, W.-D. Schneider, K. Glöckler, E. Umbach, and R. Berndt. Adsorption site determination of PTCDA on Ag(110) by manipulation of adatoms. *Surf. Sci.* 419, pp. L95–L99 (1998).

[22] Victor W. Brar, Sebastian Wickenburg, Melissa Panlasigui, Cheol-Hwan Park, Tim O. Wehling, Yuanbo Zhang, Régis Decker, Ça ğlar Girit, Alexander V. Balatsky, Steven G. Louie, Alex Zettl, and Michael F. Crommie. Observation of Carrier-Density-Dependent Many-Body Effects in Graphene via Tunneling Spectroscopy. *Phys. Rev. Lett.* 104, p. 036805 (2010).

[23] S. T. Brown, J. C. Rienstra-Kiracofe, and H. F. Schaefer. A systematic application of density functional theory to some carbon-containing molecules and their anions. *Journal of Physical Chemistry A* 103, no. 20, pp. 4065–4077 (1999).

[24] Fabien Bruneval, Nathalie Vast, and Lucia Reining. Effect of self-consistency on quasiparticles in solids. *Phys. Rev. B* 74, p. 045102 (2006).

[25] A. H. Castro Neto, F. Guinea, N. M. R. Peres, K. S. Novoselov, and A. K. Geim. The electronic properties of graphene. *Reviews of Modern Physics* 81, no. 1, pp. 109–162 (2009).

[26] GA Chamberlain. Organic solar-cells - a review. *Solar Cells* 8, no. 1, pp. 47–83 (1983).

[27] C. Julian Chen. *Introduction to Scanning Tunneling Microscopy.* Oxford University Press, 2nd edition (2008).

[28] W. Chen, T. Jamneala, V. Madhavan, and M. F. Crommie. Disappearance of the Kondo resonance for atomically fabricated cobalt dimers. *Phys. Rev. B* 60, pp. R8529–R8532 (1999).

[29] Wei Chen. *STM Investigations of Pristine Au(111) at Low Temperature and Surface-Supported Magnetic Clusters.* Ph.D. thesis, Boston University (1999).

[30] Zhihong Chen, Yu-Ming Lin, Michael J. Rooks, and Phaedon Avouris. Graphene nano-ribbon electronics. *Physica E: Low Dimensional Systems & Nanostructures* 40, no. 2, pp. 228–232 (2007). 2nd International Symposium on Nanometer-Scale Quantum Physics, Tokyo Inst Technol, Tokyo, JAPAN, JAN 24-26, 2007.

[31] T. Choi, S. Bedwani, A. Rochefort, C.-Y. Chen, A. J. Epstein, and J. A. Gupta. A single molecule Kondo switch: multistability of tetracyanoethylene on Cu(111). *Nano Lett.* 10, pp. 4175–4180 (2010).

[32] Swapan Chowdhury and Paul Kebarle. Electron affinities of di- and tetracyanoethylene and cyanobenzenes based on measurements of gas-phase electron-transfer equilibria. *Journal of the American Chemical Society* 108, no. 18, pp. 5453–5459 (1986).

[33] KM Coakley, YX Liu, MD McGehee, KL Frindell, and GD Stucky. Infiltrating semiconducting polymers into self-assembled mesoporous titania films for photovoltaic applications. *Advanced Functional Materials* 13, no. 4, pp. 301–306 (2003).

[34] M. F. Crommie, C. P. Lutz, and D. M. Eigler. Spectroscopy of a single adsorbed atom. *Phys. Rev. B* 48, pp. 2851–2854 (1993).

[35] MF Crommie, CP Lutz, and DM Eigler. Confinement of electrons to quantum corrals on a metal-surface. *Science* 262, no. 5131, pp. 218–220 (1993).

[36] MF Crommie, CP Lutz, and DM Eigler. Imaging standing waves in a 2-dimensional electron-gas. *Nature* 363, no. 6429, pp. 524–527 (1993).

[37] XD Cui, M Freitag, R Martel, L Brus, and P Avouris. Controlling energy-level alignments at carbon nanotube/Au contacts. *Nano Letters* 3, no. 6, pp. 783–787 (2003).

[38] DM Eigler and EK Schweizer. Positioning single atoms with a scanning tunneling microscope. *Nature* 344, no. 6266, pp. 524–526 (1990).

[39] M Elbing, R Ochs, M Koentopp, M Fischer, C von Hanisch, F Weigend, F Evers, HB Weber, and M Mayor. A single-molecule diode. *Proceedings of the National Academy of Sciences of the United States of America* 102, no. 25, pp. 8815–8820 (2005).

[40] D. C. Elias, R. R. Nair, T. M. G. Mohiuddin, S. V. Morozov, P. Blake, M. P. Halsall, A. C. Ferrari, D. W. Boukhvalov, M. I. Katsnelson, A. K. Geim, and K. S. Novoselov. Control of Graphene's Properties by Reversible Hydrogenation: Evidence for Graphane. *Science* 323, no. 5914, pp. 610–613 (2009).

[41] W. Erley. Reflection absorption infrared-spectroscopy of tetracyanoethylene adsorbed on Cu(111) – observation of vibronic interaction. *Journal of Physical Chemistry* 91, no. 24, pp. 6092–6094 (1987).

[42] W. Erley and H. Ibach. Spectroscopic evidence for surface anion radical formation of tetracyanoethylene adsorbed on Cu(111) At 100 K – a high-resolution electron-energy loss study. *Journal of Physical Chemistry* 91, no. 11, pp. 2947–2950 (1987).

[43] Motohiko Ezawa. Peculiar width dependence of the electronic properties of carbon nanoribbons. *Phys. Rev. B* 73, p. 045432 (2006).

[44] A.L. Fahrenbruch and R.H. Bube. *Fundamentals of Solar Cells: Photovoltaic Solar Energy Conversion*. Academic Press, New York (1983).

[45] A. M. Fennimore, T. D. Yuzvinsky, W. Q. Han, M. S. Fuhrer, J. Cumings, and A. Zettl. Rotational actuators based on carbon nanotubes. *Nature* 424, no. 6947, pp. 408–410 (2003).

[46] SR Forrest. The limits to organic photovoltaic cell efficiency. *MRS Bulletin* 30, no. 1, pp. 28–32 (2005).

[47] R. Foster. *Organic charge-transfer complexes*. Academic Press: New York (1969).

[48] M. Frank and M. Bäumer. From atoms to crystallites: adsorption on oxide-supported metal particles. *Phys. Chem. Chem. Phys.* 2, pp. 3723–3737 (2000).

[49] K. J. Franke, G. Schulze, and J. I. Pascual. Competition of Superconducting Phenomena and Kondo Screening at the Nanoscale. *Science* 332, pp. 940–944 (2011).

[50] Thomas Frederiksen, Magnus Paulsson, Mads Brandbyge, and Antti-Pekka Jauho. Inelastic transport theory from first principles: Methodology and application to nanoscale devices. *Phys. Rev. B* 75, p. 205413 (2007).

[51] M Fujita, K Wakabayashi, K Nakada, and K Kusakabe. Peculiar localized state at zigzag graphite edge. *Journal of the Physical Society of Japan* 65, no. 7, pp. 1920–1923 (1996).

[52] A. K. Geim. Graphene: Status and Prospects. *Science* 324, no. 5934, pp. 1530–1534 (2009).

[53] A. K. Geim and K. S. Novoselov. The rise of graphene. *Nature Materials* 6, no. 3, pp. 183–191 (2007).

[54] AK Ghosh, DL Morel, T Feng, RF Shaw, and CA Rowe. Photovoltaic and rectification properties of Al/Mg phthalocyanine/Ag Schottky barrier cells . *Journal of Applied Physics* 45, no. 1, pp. 230–236 (1974).

[55] Paolo Giannozzi and *et al.* QUANTUM ESPRESSO: a modular and open-source software project for quantum simulations of materials. *Journal of Physics: Condensed Matter* 21, no. 39 (2009).

[56] S Glenis, G Tourillon, and F Garnier. Influence of the Doping on the Photovoltaic Properties of Thin Films of Poly-3-methylthiophene. *Thin Solid Films* 139, no. 3, pp. 221–231 (1986).

[57] N. Gonzalez-Lakunza, I. Fernández-Torrente, K. J. Franke, N. Lorente, A. Arnau, and J. I. Pascual. Formation of Dispersive Hybrid Bands at an Organic-Metal Interface. *Phys. Rev. Lett.* 100, p. 156805 (2008).

[58] M Granstrom, K Petritsch, AC Arias, A Lux, MR Andersson, and RH Friend. Laminated fabrication of polymeric photovoltaic diodes. *Nature* 395, no. 6699, pp. 257–260 (1998).

[59] Martin A. Green, Keith Emery, Yoshihiro Hishikawa, Wilhelm Warta, and Ewan D. Dunlop. Solar cell efficiency tables (version 39). *Progress in Photovoltaics* 20, no. 1, pp. 12–20 (2012).

[60] BA Gregg. Bilayer molecular solar cells on spin-coated TiO2 substrates. *Chemical Physics Letters* 258, no. 3-4, pp. 376–380 (1996).

[61] BA Gregg. The photoconversion mechanism of excitonic solar cells. *MRS Bulletin* 30, no. 1, pp. 20–22 (2005).

[62] Michael Grobis. *Scanning Tunneling Spectroscopy of Fullerene Nanostructures*. Ph.D. thesis, University of California, Berkeley (2005).

[63] Serap Guenes, Helmut Neugebauer, and Niyazi Serdar Sariciftci. Conjugated Polymer-based Organic Solar Cells. *Chemical Reviews* 107, no. 4, pp. 1324–1338 (2007).

[64] JJM Halls, CA Walsh, NC Greenham, EA Marseglia, RH Friend, SC Moratti, and AB Holmes. Efficient photodiodes from interpenetrating polymer networks. *Nature* 376, no. 6540, pp. 498–500 (1995).

[65] Melinda Y. Han, Barbaros Özyilmaz, Yuanbo Zhang, and Philip Kim. Energy Band-Gap Engineering of Graphene Nanoribbons. *Phys. Rev. Lett.* 98, p. 206805 (2007).

[66] EL Hanson, J Guo, N Koch, J Schwartz, and SL Bernasek. Advanced surface modification of indium tin oxide for improved charge injection in organic devices. *Journal of the American Chemical Society* 127, no. 28, pp. 10058–10062 (2005).

[67] D. Haskel, Z. Islam, J. Lang, C. Kmety, G. Srajer, K. I. Pokhodnya, A. J. Epstein, and Joel S. Miller. Local structural order in the disordered vanadium tetracyanoethylene room-temperature molecule-based magnet. *Physical Review B* 70, no. 5, p. 054422 (2004).

[68] Lars Hedin. New Method for Calculating the One-Particle Green's Function with Application to the Electron-Gas Problem. *Phys. Rev.* 139, pp. A796–A823 (1965).

[69] AJ Heinrich, CP Lutz, JA Gupta, and DM Eigler. Molecule cascades. *Science* 298, no. 5597, pp. 1381–1387 (2002).

[70] CF Hirjibehedin, CP Lutz, and AJ Heinrich. Spin coupling in engineered atomic structures. *Science* 312, no. 5776, pp. 1021–1024 (2006).

[71] Saw-Wai Hla, Ludwig Bartels, Gerhard Meyer, and Karl-Heinz Rieder. Inducing all steps of a chemical reaction with the scanning tunneling microscope tip: towards single molecule engineering. *Phys. Rev. Lett.* 85, pp. 2777–2780 (2000).

[72] Saw-Wai Hla, Kai-Felix Braun, and Karl-Heinz Rieder. Single-atom manipulation mechanisms during a quantum corral construction. *Phys. Rev. B* 67, p. 201402 (2003).

[73] W Ho. Single-molecule chemistry. *Journal of Chemical Physics* 117, no. 24, pp. 11033–11061 (2002).

[74] Oded Hod, Veronica Barone, Juan E. Peralta, and Gustavo E. Scuseria. Enhanced half-metallicity in edge-oxidized zigzag graphene nanoribbons. *Nano Letters* 7, no. 8, pp. 2295–2299 (2007).

[75] W. A. Hofer. Challenges and errors: interpreting high resolution images in scanning tunneling microscopy. *Prog. Surf. Sci.* 71, pp. 147–183 (2003).

[76] Ph. Hofmann, K.-M. Schindler, S. Bao, A. M. Bradshaw, and D. P. Woodruff. Direct identification of atomic and molecular adsorption sites using photoelectron diffraction. *Nature* 368, pp. 131–132 (1994).

[77] N. Holonyak, I. A. Lesk, R. N. Hall, J. J. Tiemann, and H. Ehrenreich. Direct Observation of Phonons During Tunneling in Narrow Junction Diodes. *Phys. Rev. Lett.* 3, pp. 167–168 (1959).

[78] H Hoppe and NS Sariciftci. Organic solar cells: An overview. *Journal of Materials Research* 19, no. 7, pp. 1924–1945 (2004).

[79] H Hoppe, NS Sariciftci, and D Meissner. Optical constants of conjugated polymer /fullerene based bulk-heterojunction organic solar cells. *Molecular Crystals And Liquid Crystals* 385, pp. 233–239 (2002).

[80] WU Huynh, JJ Dittmer, and AP Alivisatos. Hybrid nanorod-polymer solar cells. *Science* 295, no. 5564, pp. 2425–2427 (2002).

[81] Mark S. Hybertsen and Steven G. Louie. Electron correlation in semiconductors and insulators: Band gaps and quasiparticle energies. *Phys. Rev. B* 34, pp. 5390–5413 (1986).

[82] P. Yang (editor) J. R. Long. *Chemistry of Nanostructured Materials*, p. 291. World Scientific, Hong Kong (2003).

[83] F. Jäckel, U. G. E. Perera, V. Iancu, K.-F. Braun, N. Koch, J. P. Rabe, and S.-W. Hla. Investigating Molecular Charge Transfer Complexes with a Low Temperature Scanning Tunneling Microscope. *Phys. Rev. Lett.* 100, p. 126102 (2008).

[84] Koblar Jackson and Mark R. Pederson. Accurate forces in a local-orbital approach to the local-density approximation. *Physical Review B* 42, no. 6, pp. 3276–3281 (1990).

[85] R. C. Jaklevic and J. Lambe. Molecular Vibration Spectra by Electron Tunneling. *Phys. Rev. Lett.* 17, pp. 1139–1140 (1966).

[86] T. Jamneala, V. Madhavan, and M. F. Crommie. Kondo Response of a Single Antiferromagnetic Chromium Trimer. *Phys. Rev. Lett.* 87, p. 256804 (2001).

[87] Tiberiu Jamneala. *Tunneling Measurements of the Electronic Structure of Magnetic Nanostructures on Surfaces*. Ph.D. thesis, University of California, Berkeley (2001).

[88] C. Jayaprakash, H. R. Krishna-murthy, and J. W. Wilkins. Two-Impurity Kondo Problem. *Physical Review Letters* 47, no. 10, pp. 737–740 (1981).

[89] K. Jensen, J. Weldon, H. Garcia, and A. Zettl. Nanotube radio. *Nano Letters* 7, no. 11, pp. 3508–3511 (2007).

[90] Liying Jiao, Xinran Wang, Georgi Diankov, Hailiang Wang, and Hongjie Dai. Facile synthesis of high-quality graphene nanoribbons. *Nature Nanotechnology* 5, no. 5, pp. 321–325 (2010).

[91] S Karg, W Riess, V Dyakonov, and M Schwoerer. Electrical and Optical Characterization of Poly(phenylene-vinylene) Light Emitting Diodes. *Synthetic Metals* 54, no. 1-3, pp. 427–433 (1993).

[92] D Kearns and M Calvin. Photovoltaic Effect and Photoconductivity in Laminated Organic Systems. *Journal of Chemical Physics* 29, no. 4, pp. 950–951 (1958).

[93] C. Kittel. *Introduction to Solid State Physics*. Wiley, New York (2004).

[94] C. Klein, A. Eichler, E. L. D. Hebenstreit, G. Pauer, R. Koller, A. Winkler, M. Schmid, and P. Varga. When Scanning Tunneling Microscopy Gets the Wrong Adsorption Site: H on Rh(100). *Phys. Rev. Lett.* 90, p. 176101 (2003).

[95] DJ Klein and L Bytautas. Graphitic edges and unpaired pi-electron spins. *Journal of Physical Chemistry A* 103, no. 26, pp. 5196–5210 (1999).

[96] Leonard Kleinman and D. M. Bylander. Efficacious form for model pseudopotentials. *Phys. Rev. Lett.* 48, pp. 1425–1428 (1982).

[97] W. Kohn and L. J. Sham. Self-consistent equations including exchange and correlation effects. *Phys. Rev.* 140, pp. A1133–A1138 (1965).

[98] J KONDO. Resistance Minimum in Dilute Magnetic Alloys. *Progress of Theoretical Physics* 32, no. 1, pp. 37–49 (1964).

[99] J. B. Kortright, D. M. Lincoln, R. Shima Edelstein, and A. J. Epstein. Bonding, Backbonding, and Spin-Polarized Molecular Orbitals: Basis for Magnetism and Semiconducting Transport in V[TCNE]$_{x\sim2}$. *Physical Review Letters* 100, no. 25, 257204 (2008).

[100] Dmitry V. Kosynkin, Amanda L. Higginbotham, Alexander Sinitskii, Jay R. Lomeda, Ayrat Dimiev, B. Katherine Price, and James M. Tour. Longitudinal unzipping of carbon nanotubes to form graphene nanoribbons. *Nature* 458, no. 7240, pp. 872–U5 (2009).

[101] A. Kraft, R. Temirov, S. K. M. Henze, S. Soubatch, M. Rohlfing, and F. S. Tautz. Lateral adsorption geometry and site-specific electronic structure of a large organic chemisorbate on a metal surface. *Phys. Rev. B* 74, p. 041402(R) (2006).

[102] G. Kresse and J. Furthmüller. Efficient iterative schemes for *ab initio* total-energy calculations using a plane-wave basis set. *Phys. Rev. B* 54, pp. 11169–11186 (1996).

[103] G. Kresse and D. Joubert. From ultrasoft pseudopotentials to the projector augmented-wave method. *Phys. Rev. B* 59, pp. 1758–1775 (1999).

[104] J. Lagoute, K. Kanisawa, and S. Fölsch. Manipulation and adsorption-site mapping of single pentacene molecules on Cu(111). *Phys. Rev. B* 70, p. 245415 (2004).

[105] SC Lam and RJ Needs. First-principles calculations of the screening of electric-fields at the aluminum (111) and (110) surfaces. *Journal of Physics-Condensed Matter* 5, no. 14, pp. 2101–2108 (1993).

[106] M Law, LE Greene, JC Johnson, R Saykally, and PD Yang. Nanowire dye-sensitized solar cells. *Nature Materials* 4, no. 6, pp. 455–459 (2005).

[107] HJ Lee and W Ho. Single-bond formation and characterization with a scanning tunneling microscope. *Science* 286, no. 5445, pp. 1719–1722 (1999).

[108] N. Levy, S. A. Burke, K. L. Meaker, M. Panlasigui, A. Zettl, F. Guinea, A. H. Castro Neto, and M. F. Crommie. Strain-Induced Pseudo-Magnetic Fields Greater Than 300 Tesla in Graphene Nanobubbles. *Science* 329, no. 5991, pp. 544–547 (2010).

[109] Jiutao Li, Wolf-Dieter Schneider, Richard Berndt, and Bernard Delley. Kondo Scattering Observed at a Single Magnetic Impurity. *Physical Review Letters* 80, no. 13, pp. 2893–2896 (1998).

[110] Xiaolin Li, Xinran Wang, Li Zhang, Sangwon Lee, and Hongjie Dai. Chemically derived, ultrasmooth graphene nanoribbon semiconductors. *Science* 319, no. 5867, pp. 1229–1232 (2008).

[111] Peter Liljeroth, Ingmar Swart, Sami Paavilainen, Jascha Repp, and Gerhard Meyer. Single-Molecule Synthesis and Characterization of Metal-Ligand Complexes by Low-Temperature STM. *Nano Letters* 10, no. 7, pp. 2475–2479 (2010).

[112] N Liu, NA Pradhan, and W Ho. Vibronic states in single molecules: C_{60} and C_{70} on ultrathin Al_2O_3 films. *Journal of Chemical Physics* 120, no. 24, pp. 11371–11375 (2004).

[113] N. Lorente. Mode excitation induced by the scanning tunnelling microscope. *Appl. Phys. A* 78, pp. 799–806 (2004).

[114] N. Lorente and M. Persson. Theory of Single Molecule Vibrational Spectroscopy and Microscopy. *Phys. Rev. Lett.* 85, pp. 2997–3000 (2000).

[115] N. Lorente, M. Persson, L. J. Lauhon, and W. Ho. Symmetry Selection Rules for Vibrationally Inelastic Tunneling. *Phys. Rev. Lett.* 86, pp. 2593–2596 (2001).

[116] Xinghua Lu. *Scanning Tunneling Spectroscopy of Fullerenes, Diamondoids, and Organometallic Molecular Nanostructures*. Ph.D. thesis, University of California, Berkeley (2006).

[117] V. Madhavan, W. Chen, T. Jamneala, M. F. Crommie, and N. S. Wingreen. Tunneling into a Single Magnetic Atom: Spectroscopic Evidence of the Kondo Resonance. *Science* 280, no. 5363, pp. 567–569 (1998).

[118] Vidya Madhavan. *Electronic Properties of Magnetic Nanoclusters: A Scanning Tunneling Microscope Study of Transition Metal Atoms on Au(111)*. Ph.D. thesis, Boston University (2000).

[119] Juan M. Manriquez, Gordon T. Yee, R. Scott Mclean, Arthur J. Epstein, and Joel S. Miller. A Room-Temperature Molecular/Organic-Based Magnet. *Science* 252, no. 5011, pp. 1415–1417 (1991).

[120] J. M. Masnovi and J. K. Kochi. Cycloreversion Induced by Charge-Transfer Excitation of Electron-Donor Acceptor Complexes—Wavelength-Dependent Photochemistry of Dianthracene. *Journal of the American Chemical Society* 107, no. 24, pp. 6781–6788 (1985).

[121] Focko Meier, Lihui Zhou, Jens Wiebe, and Roland Wiesendanger. Revealing Magnetic Interactions from Single-Atom Magnetization Curves. *Science* 320, no. 5872, pp. 82–86 (2008).

[122] RM Metzger. Unimolecular electrical rectifiers. *Chemical Reviews* 103, no. 9, pp. 3803–3834 (2003).

[123] G. Meyer, S. Zöphel, and K.-H. Rieder. Scanning Tunneling Microscopy Manipulation of Native Substrate Atoms: A New Way to Obtain Registry Information on Foreign Adsorbates. *Phys. Rev. Lett.* 77, p. 2113 (1996).

[124] K. H. Michaelian, K. E. Rieckhoff, and E. M. Voigt. Valence Force-Field Analysis of Tetracyanoethylene. *Journal of Molecular Spectroscopy* 95, no. 1, pp. 1–8 (1982).

[125] K. H. Michaelian, K. E. Rieckhoff, and E. M. Voigt. Valence force field analysis of tetracyanoethylene. *J. Mol. Spectrosc.* 95, p. 1 (1982).

[126] Fabian Mohn, Jascha Repp, Leo Gross, Gerhard Meyer, Matthew S. Dyer, and Mats Persson. Reversible Bond Formation in a Gold-Atom-Organic-Molecule Complex as a Molecular Switch. *Phys. Rev. Lett.* 105, p. 266102 (2010).

[127] G. E. Moore. Cramming more components onto integrated circuits (Reprinted from Electronics, pg 114-117, April 19, 1965). *Proceedings of the IEEE* 86, no. 1, pp. 82–85 (1998).

[128] R. G. Musket, W. McLean, C. A. Colmenares, D. M. Makowiecki, and W. J. Siekhaus. Preparation of Atomically Clean Surfaces of Selected Elements: A Review. *Applications of Surface Science* 10, pp. 143–207 (1982).

[129] Kyoko Nakada, Mitsutaka Fujita, Gene Dresselhaus, and Mildred S. Dresselhaus. Edge state in graphene ribbons: Nanometer size effect and edge shape dependence. *Phys. Rev. B* 54, pp. 17954–17961 (1996).

[130] J. B. Neaton, Mark S. Hybertsen, and Steven G. Louie. Renormalization of Molecular Electronic Levels at Metal-Molecule Interfaces. *Phys. Rev. Lett.* 97, p. 216405 (2006).

[131] J Nelson. Organic photovoltaic films. *Current Opinion in Solid State & Materials Science* 6, no. 1, pp. 87–95 (2002).

[132] A Nitzan and MA Ratner. Electron transport in molecular wire junctions. *Science* 300, no. 5624, pp. 1384–1389 (2003).

[133] KS Novoselov, AK Geim, SV Morozov, D Jiang, MI Katsnelson, IV Grigorieva, SV Dubonos, and AA Firsov. Two-dimensional gas of massless Dirac fermions in graphene. *Nature* 438, no. 7065, pp. 197–200 (2005).

[134] KS Novoselov, AK Geim, SV Morozov, D Jiang, Y Zhang, SV Dubonos, IV Grigorieva, and AA Firsov. Electric field effect in atomically thin carbon films. *Science* 306, no. 5696, pp. 666–669 (2004).

[135] Norio Okabayashi, Magnus Paulsson, Hiromu Ueba, Youhei Konda, and Tadahiro Komeda. Inelastic Tunneling Spectroscopy of Alkanethiol Molecules: High-Resolution Spectroscopy and Theoretical Simulations. *Phys. Rev. Lett.* 104, p. 077801 (2010).

[136] Pablo Ordejón, Emilio Artacho, and José M. Soler. Self-consistent order-N density-functional calculations for very large systems. *Phys. Rev. B* 53, pp. R10441–R10444 (1996).

[137] B Oregan and M Gratzel. A low-cost, high-efficiency solar-cell based on dye-sensitized colloidal TiO2 films. *Nature* 353, no. 6346, pp. 737–740 (1991).

[138] Paul A. Packan. DEVICE PHYSICS: Pushing the Limits. *Science* 285, no. 5436, pp. 2079–2081 (1999).

[139] F. M. Pan, J. C. Hemminger, and S. Ushioda. Adsorption of Tetracyanoethylene on a Nickel(111) Surface Studied by Auger-Electron Spectroscopy, Thermal-Desorption Spectroscopy, and Raman-Spectroscopy. *Journal of Physical Chemistry* 89, no. 5, pp. 862–867 (1985).

[140] Minghu Pan, E. Costa Girao, Xiaoting Jia, Sreekar Bhaviripudi, Qing Li, Jing Kong, V. Meunier, and Mildred S. Dresselhaus. Topographic and Spectroscopic Characterization of Electronic Edge States in CVD Grown Graphene Nanoribbons. *Nano Letters* 12, no. 4, pp. 1928–1933 (2012).

[141] Changwon Park, Heejun Yang, Andrew J. Mayne, Gerald Dujardin, Sunae Seo, Young Kuk, Jisoon Ihm, and Gunn Kim. Formation of unconventional standing waves at graphene edges by valley mixing and pseudospin rotation. *Proceedings of the National Academy of Science of the United States of America* 108, no. 46, pp. 18622–18625 (2011).

[142] H Park, J Park, AKL Lim, EH Anderson, AP Alivisatos, and PL McEuen. Nanomechanical oscillations in a single-C-60 transistor. *Nature* 407, no. 6800, pp. 57–60 (2000).

[143] J Park, AN Pasupathy, JI Goldsmith, C Chang, Y Yaish, JR Petta, M Rinkoski, JP Sethna, HD Abruna, PL McEuen, and DC Ralph. Coulomb blockade and the Kondo effect in single-atom transistors. *Nature* 417, no. 6890, pp. 722–725 (2002).

[144] A. N. Pasupathy, J. Park, C. Chang, A. V. Soldatov, S. Lebedkin, R. C. Bialczak, J. E. Grose, L. A. K. Donev, J. P. Sethna, D. C. Ralph, and P. L. McEuen. Vibration-assisted electron tunneling in C140 transistors. *Nano Letters* 5, no. 2, pp. 203–207 (2005).

[145] M. R. Pederson, D. V. Porezag, J. Kortus, and D. C. Patton. Strategies for massively parallel local-orbital-based electronic structure methods. *Physica Status Solidi B—Basic Research* 217, no. 1, pp. 197–218 (2000).

[146] Mark R. Pederson and Koblar A. Jackson. Variational mesh for quantum-mechanical simulations. *Physical Review B* 41, no. 11, pp. 7453–7461 (1990).

[147] Mark R. Pederson and Koblar A. Jackson. Pseudoenergies for simulations on metallic systems. *Physical Review B* 43, no. 9, pp. 7312–7315 (1991).

[148] J. P. Perdew and Alex Zunger. Self-interaction correction to density-functional approximations for many-electron systems. *Phys. Rev. B* 23, pp. 5048–5079 (1981).

[149] John P. Perdew, Kieron Burke, and Matthias Ernzerhof. Generalized Gradient Approximation Made Simple. *Physical Review Letters* 77, no. 18, pp. 3865–3868 (1996).

[150] John P. Perdew, Kieron Burke, and Matthias Ernzerhof. Generalized Gradient Approximation Made Simple. *Phys. Rev. Lett.* 77, pp. 3865–3868 (1996).

[151] LAA Pettersson, LS Roman, and O Inganas. Modeling photocurrent action spectra of photovoltaic devices based on organic thin films. *Journal of Applied Physics* 86, no. 1, pp. 487–496 (1999).

[152] P Peumans, V Bulovic, and SR Forrest. Efficient, high-bandwidth organic multilayer photodetectors. *Applied Physics Letters* 76, no. 26, pp. 3855–3857 (2000).

[153] P Peumans, S Uchida, and SR Forrest. Efficient bulk heterojunction photovoltaic cells using small molecular-weight organic thin films. *Nature* 425, p. 158 (2003).

[154] P Peumans, A Yakimov, and SR Forrest. Small molecular weight organic thin-film photodetectors and solar cells. *Journal of Applied Physics* 93, no. 7, pp. 3693–3723 (2003).

[155] K. I. Pokhodnya, A. J. Epstein, and J. S. Miller. Thin-film V[TCNE]$_x$ magnets. *Advanced Materials* 12, no. 6, pp. 410–413 (2000).

[156] Guo-Xin Qian, Richard M. Martin, and D. J. Chadi. First-principles study of the atomic reconstructions and energies of Ga- and As-stabilized GaAs(100) surfaces. *Phys. Rev. B* 38, pp. 7649–7663 (1988).

[157] X. H. Qiu, G. V. Nazin, and W. Ho. Vibronic States in Single Molecule Electron Transport. *Phys. Rev. Lett.* 92, p. 206102 (2004).

[158] S. Reich, J. Maultzsch, C. Thomsen, and P. Ordejón. Tight-binding description of graphene. *Phys. Rev. B* 66, p. 035412 (2002).

[159] J Repp, G Meyer, S Paavilainen, FE Olsson, and M Persson. Imaging bond formation between a gold atom and pentacene on an insulating surface. *Science* 312, no. 5777, pp. 1196–1199 (2006).

[160] Jascha Repp, Gerhard Meyer, Sladjana M. Stojković, André Gourdon, and Christian Joachim. Molecules on Insulating Films: Scanning-Tunneling Microscopy Imaging of Individual Molecular Orbitals. *Phys. Rev. Lett.* 94, p. 026803 (2005).

[161] M. G. Reuter, T. Seideman, and M. A. Ratner. Guidelines for choosing molecular alligator clip binding motifs in electron transport devices. *J. Chem. Phys.* 134, p. 154708 (2011).

[162] BL Rogers, JG Shapter, WM Skinner, and K Gascoigne. A method for production of cheap, reliable Pt-Ir tips. *Review of Scientific Instruments* 71, no. 4, pp. 1702–1705 (2000).

[163] J Rostalski and D Meissner. Photocurrent Spectroscopy for the Investigation of Charge Carrier Generation and Transport Mechanisms in Organic p/n-junction Solar Cells. *Solar Energy Materials and Solar Cells* 63, no. 1, pp. 37–47 (2000). ECOS 98 Seminar, NANCY, FRANCE, JUL, 1998.

[164] NS Sariciftci, F Wudl, AJ Heeger, M Maggini, G Scorrano, M Prato, J Bourassa, and PC Ford. Photoinduced electron transfer and long lived charge separation in a donor-bridge-acceptor supramolecular 'diad' consisting of ruthenium(II) tris(bipyridine) functionalized C_60. *Chemical Physics Letters* 247, no. 4-6, pp. 510–514 (1995).

[165] D. M. Seo, V. Meenakshi, W. Teizer, H. Zhao, and K. R. Dunbar. Enhanced magnetic anisotropy of Mn_{12}-acetate. *Journal of Magnetism and Magnetic Materials* 301, no. 1, pp. 31–36 (2006).

[166] R. Smoluchowski. Anisotropy of the Electronic Work Function of Metals. *Phys. Rev.* 60, pp. 661–674 (1941).

[167] Jorge O. Sofo, Ajay S. Chaudhari, and Greg D. Barber. Graphane: A two-dimensional hydrocarbon. *Phys. Rev. B* 75, p. 153401 (2007).

[168] JM Soler, E Artacho, JD Gale, A Garcia, J Junquera, P Ordejon, and D Sanchez-Portal. The SIESTA method for ab initio order-N materials simulation. *Journal of Physics-Condensed Matter* 14, no. 11, pp. 2745–2779 (2002).

[169] Young-Woo Son, Marvin L. Cohen, and Steven G. Louie. Energy gaps in graphene nanoribbons. *Physical Review Letters* 97, no. 21 (2006).

[170] Young-Woo Son, Marvin L. Cohen, and Steven G. Louie. Half-metallic graphene nanoribbons. *Nature* 444, no. 7117, pp. 347–349 (2006).

[171] BC Stipe, MA Rezaei, and W Ho. Single-molecule vibrational spectroscopy and microscopy. *Science* 280, no. 5370, pp. 1732–1735 (1998).

[172] CW Tang. 2-Layer organic photovoltaic cell. *Applied Physics Letters* 48, no. 2, pp. 183–185 (1986).

[173] Chenggang Tao, Liying Jiao, Oleg V. Yazyev, Yen-Chia Chen, Juanjuan Feng, Xiaowei Zhang, Rodrigo B. Capaz, James M. Tour, Alex Zettl, Steven G. Louie, Hongjie Dai, and Michael F. Crommie. Spatially resolving edge states of chiral graphene nanoribbons. *Nature Physics* 7, no. 8, pp. 616–620 (2011).

[174] F. S. Tautz. Structure and bonding of large aromatic molecules on noble metal surfaces: The example of PTCDA. *Prog. Surf. Sci.* 82, pp. 479–520 (2007).

[175] C. Tengstedt, M. P. de Jong, A. Kanciurzewska, E. Carlegrim, and M. Fahlman. X-Ray Magnetic Circular Dichroism and Resonant Photomission of $V(TCNE)_x$ Hybrid Magnets. *Physical Review Letters* 96, no. 5, 057209 (2006).

[176] J. Tersoff and D. R. Hamann. Theory of the scanning tunneling microscope. *Phys. Rev. B* 31, pp. 805–813 (1985).

[177] N. Troullier and José Luriaas Martins. Efficient pseudopotentials for plane-wave calculations. *Phys. Rev. B* 43, pp. 1993–2006 (1991).

[178] David Vanderbilt. Soft self-consistent pseudopotentials in a generalized eigenvalue formalism. *Phys. Rev. B* 41, pp. 7892–7895 (1990).

[179] P. Wahl, P. Simon, L. Diekhöner, V. S. Stepanyuk, P. Bruno, M. A. Schneider, and K. Kern. Exchange Interaction between Single Magnetic Adatoms. *Phys. Rev. Lett.* 98, p. 056601 (2007).

[180] Yayu Wang, Ryan Yamachika, Andre Wachowiak, Michael Grobis, and Michael F. Crommie. Tuning fulleride electronic structure and molecular ordering via variable layer index. *Nature Materials* 7, no. 3, pp. 194–197 (2008).

[181] Tobias Wassmann, Ari P. Seitsonen, A. Marco Saitta, Michele Lazzeri, and Francesco Mauri. Structure, Stability, Edge States, and Aromaticity of Graphene Ribbons. *Phys. Rev. Lett.* 101, p. 096402 (2008).

[182] Tobias Wassmann, Ari P. Seitsonen, A. Marco Saitta, Michele Lazzeri, and Francesco Mauri. Clar's Theory, pi-Electron Distribution, and Geometry of Graphene Nanoribbons. *Journal of the American Chemical Society* 132, no. 10, pp. 3440–3451 (2010).

[183] D. Wegner, R. Yamachika, Y. Wang, V. W. Brar, B. M. Bartlett, J. R. Long, and M. F. Crommie. Single-Molecule Charge Transfer and Bonding at an Organic/Inorganic Interface: Tetracyanoethylene on Noble Metals. *Nano Lett.* 8, pp. 131–135 (2008).

[184] Daniel Wegner, Ryan Yamachika, Xiaowei Zhang, Yayu Wang, Tunna Baruah, Mark R. Pederson, Bart M. Bartlett, Jeffrey R. Long, and Michael F. Crommie. Tuning molecule-mediated spin coupling in bottom-up-fabricated vanadium-tetracyanoethylene nanostructures. *Phys. Rev. Lett.* 103, p. 087205 (2009).

[185] BR Weinberger, M Akhtar, and SC Gau. Polyacetylene Photovoltaic Devices. *Synthetic Metals* 4, no. 3, pp. 187–197 (1982).

[186] M. Wimmer, A. R. Akhmerov, and F. Guinea. Robustness of edge states in graphene quantum dots. *Phys. Rev. B* 82, p. 045409 (2010).

[187] Ch. Wöll, S. Chiang, R. J. Wilson, and P. H. Lippel. Determination of atom positions at stacking-fault dislocations on Au(111) by scanning tunneling microscopy. *Phys. Rev. B* 39, pp. 7988–7991 (1989).

[188] S. W. Wu, G. V. Nazin, X. Chen, X. H. Qiu, and W. Ho. Control of Relative Tunneling Rates in Single Molecule Bipolar Electron Transport. *Phys. Rev. Lett.* 93, p. 236802 (2004).

[189] F Wudl. The Chemical Properties of Buckminsterfullerene (C_{60}) and the Birth and Infancy of Fulleroids. *Accounts of Chemical Research* 25, no. 3, pp. 157–161 (1992).

[190] Liming Xie, Liying Jiao, and Hongjie Dai. Selective Etching of Graphene Edges by Hydrogen Plasma. *Journal of the American Chemical Society* 132, no. 42, pp. 14751–14753 (2010).

[191] R Yamachika, M Grobis, A Wachowiak, and MF Crommie. Controlled atomic doping of a single C_{60} molecule. *Science* 304, no. 5668, pp. 281–284 (2004).

[192] Ryan Yamachika. *Probing Atomic-Scale Properties of Organic and Organometallic Molecules by Scanning Tunneling Spectroscopy*. Ph.D. thesis, University of California, Berkeley (2009).

[193] Oleg V. Yazyev. Magnetism in Disordered Graphene and Irradiated Graphite. *Phys. Rev. Lett.* 101, p. 037203 (2008).

[194] Oleg V. Yazyev, Rodrigo B. Capaz, and Steven G. Louie. Theory of magnetic edge states in chiral graphene nanoribbons. *Physical Review B* 84, no. 11 (2011).

[195] Oleg V. Yazyev and M. I. Katsnelson. Magnetic Correlations at Graphene Edges: Basis for Novel Spintronics Devices. *Phys. Rev. Lett.* 100, p. 047209 (2008).

[196] Andrea F. Young and Philip Kim. Quantum interference and Klein tunnelling in graphene heterojunctions. *Nature Physics* 5, no. 3, pp. 222–226 (2009).

[197] G Yu, J Gao, JC Hummelen, F Wudl, and AJ Heeger. Polymer photovoltaic cells - enhanced efficiencies via a network of internal donor-acceptor heterojunctions. *Science* 270, no. 5243, pp. 1789–1791 (1995).

[198] G Yu, J Wang, J McElvain, and AJ Heeger. Large-area, Full-color Image Sensors Made with Semiconducting Polymers. *Advanced Materials* 10, no. 17, pp. 1431–1434 (1998).

[199] YB Zhang, YW Tan, HL Stormer, and P Kim. Experimental observation of the quantum Hall effect and Berry's phase in graphene. *Nature* 438, no. 7065, pp. 201–204 (2005).

[200] Yuanbo Zhang, Victor W. Brar, Feng Wang, Caglar Girit, Yossi Yayon, Melissa Panlasigui, Alex Zettl, and Michael F. Crommie. Giant phonon-induced conductance in scanning tunnelling spectroscopy of gate-tunable graphene. *Nature Physics* 4, no. 8, pp. 627–630 (2008).